Development of novel Ti-Nb based alloys for biomedical applications

A thesis

submitted in fulfilment

of the requirements for the degree

of

Masters of Engineering in Materials and Processing

at

The University of Waikato

by

Balakrishnan Manogar

THE UNIVERSITY OF
WAIKATO
Te Whare Wānanga o Waikato

2021

Abstract

Since the advent of industrialisation, the interaction between humans and machines have become imminent. In doing so, unfortunate accidents are bound to occur resulting in severe injury or loss. On the other hand, with the advancement of modern medicine many pathological diseases have been eradicated. This has caused the overall life expectancy to increase. As a result, population of the elderly is increasing day by day. Subsequently, due to old age, accidents and poor lifestyle, joints and bone tend to experience premature fatigue. In order to overcome this issue, patients prefer to use implant materials to restore the functionality of the injured part of the body. A few common examples where implant materials are employed are in Total knee and hip replacement surgery and spinal fixation. Since there is a structural (load bearing) component to these implants, among various classes of materials such as ceramics and plastics, metallic biomaterials are deemed to be an appropriate fit. Among the metallic materials, stainless steel (SS 316L), Co-Cr alloys and Ti alloys are the primary choice. SS 316L and Co-Cr alloys have been used as structural implant materials for a couple of decades. However, it is important that the material does not induce any immune response or in any way affect the homeostasis of the patient. Taking this into consideration, Ti has been confirmed to be the most favourable choice for structural implant materials as it is biocompatible and has high specific strength i.e. it possesses high strength to weight ratio. This becomes very critical especially in terms of the comfort of the patient.

Ti-Nb based alloys are considered to be effective in employing as an implant material. Thus, two systems of Ti-Nb based ternary alloys were developed by adding manganese (Mn) and iron (Fe). Among various Ti alloys, Ti-Nb alloys have been scarcely explored and elements such as Mn and Fe, becomes especially significant in terms of availability, ease of processing and the biocompatible nature. Powder metallurgy is chosen as the processing route owing to its capability to incorporate a wide range of alloying elements, the near net shape products prevents material wastage and the possibility to control the porosity. Using Mn and Fe becomes critical while processing via powder metallurgy as the primary means of densification is diffusion and both Mn and Fe have high diffusivity with Ti.

Since both Ti-Nb-Mn and Ti-Nb-Fe systems have not been explored to a larger extent, 8 compositions from Ti-Nb-Mn and 12 compositions from Ti-Nb-Fe were designed. So, 8 Ti-Nb-Mn alloys and 12 Ti-Nb-Fe alloys along with C.P. Ti as reference were warm compacted at 250^{o}C, vacuum sintered at 1300^{o}C and characterised for various physical and mechanical properties.

The relative green density were found to be above 85% and relative sintered density ≥ 95%. Hence, the maximum porosity was about 5% and the least was around 2%. Warm compaction of the alloys helped to achieve a higher green density when compared to conventional cold pressing of elemental powders.

Based on the microstructural analysis by optical and electron microscopy most of the alloys were characterised by Widmänstatten microstructures with varying levels of refinement in the α+β lamellae and the interlamellar spacing due to the effect of adding β stabilisers. Since all the alloys have achieved a relative density above 95% most of the alloys consists of closed pores. The size and distribution however varied depending on the density values.

Mechanical properties were measured by conducting a uniaxial tensile test and Rockwell hardness test. It was found that with the addition of alloying elements leads to solid solution strengthening and as a result the strength increases with the addition of Nb, Fe and Mn. The hardness also follows a similar trend with most of the alloys except a few that were influenced by porosity. Among Ti-Nb-Mn alloys, Ti-6Nb-8Mn exhibited the highest UTS of 1090 MPa and Ti-5Nb-5Mn exhibited the highest elongation to failure. For the Ti-Nb-Fe system, Ti-9Nb-6Fe possesses the highest UTS and Ti-2Nb-3Fe showed highest elongation to failure. Among both the system, Ti-Nb-Mn alloys possessed high strength and relatively very low ductility whereas it Ti-Nb-Fe alloys had a good combination of strength and ductility. In order to improve the performance of the alloys to be used as implant materials, the near β and metastable β alloys can be subjected to thermo-mechanical processing or heat treatment.

Acknowledgements

Gratitude is a quality similar to electricity; It must be produced and discharged and used up in order to exist at all.

- William Faulkner

University of Waikato has been home away from home. The campus and the people here are really welcoming and accommodating. I am grateful to have spent the last couple of months in this solace.

Dr. Leandro Bolzoni has been very supportive. He always inspires his students with this passion to research. I feel grateful and blessed to have worked under his supervision. Apart from academics, his guidance onto other skill developments such as public speaking is really appreciated. Huge thanks to Johnathan Van Harselaar (Jonny) and Duncan Barnard, the technical officers who were always available just a text or call away. Without them my project would have got much delayed. Thank you very much guys for the helping hand you lend with the training and getting our characterisation done. Next up, a big thank you to Helen Turner who was patient in teaching me how to use the electron microscope. Cheryl Ward is a magician and I would like to humbly thank her for spending hours together to sort out my formatting issues. If this thesis looks appealing, she should take the major credit for it.

Lastly, thank you to my family back in India, who have always supported me and been with me during good and bad times.

Table of Contents

List of Figures

List of Tables

Chapter One

Introduction

1.1 Introduction to biomaterials

Human bone is a fibrous connective tissue providing anchorage to the muscles and protecting vital organs [1; 2]. In order to serve these functions, the structure of bones has evolved in such a way that it has a hard-outer region called the 'cortical bone' (4-30GPa) and a porous inner region called the 'trabecular bone' (0.2 – 2 GPa). Such a construct helps the bone to be stiff and flexible at the same time so as to avoid bending and absorb energy correspondingly [3]

By virtue of the development of modern medicine and improved life expectancy, the aged population has been increasing and various muscoskeletal disorders such as osteoporosis, osteoarthritis, and general frailty problems are noticed among the general population due to fatigue and poor life style [1]. Disturbance to mobility is considered to be the third most alarming issue after cardio-vascular diseases and cancer. Thus, a situation such as this has raised the need to invent advanced implant materials to relieve the injured patients from their pain and aid normal functioning of skeletal muscles. Balck (as cited in Katti) [4] defined biomaterials as materials of natural or man-made origin that are used to directly supplement or replace the functions of living tissues. Biomaterials are generally used in orthopaedics, dental care, drug delivery and cardiovascular devices as shown in Figure 1.1.

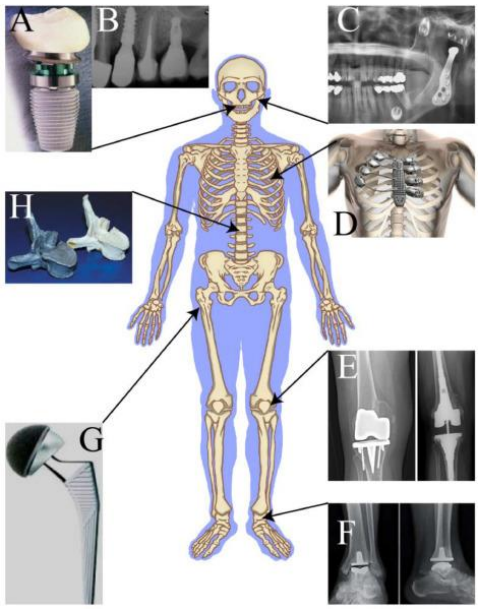

Figure 1.1 Illustration of various implant biomaterials for different applications i.e., dental (A, B, C), rib replacement (D), ankle and knee arthroplasty (E,F), hip replacement (G) and spine fixation (H) [5].

Depending on the type of the response the body exhibits while interacting with a biomaterial, they are classified are toxic, bio-inert, bio-active, and bio-degradable [1]. Williams [6] defines biocompatibility as the ability of a material to perform its desired function with respect to a medical therapy, without eliciting any undesirable local or systemic effects in the recipient or beneficiary of that therapy, but generating the most appropriate beneficial cellular or tissue response to that specific situation, and optimising the clinically relevant performance of that therapy. In other words, it states that the material being introduced into the body should bind well with the system and not intend to elicit any immune response.

The classes of materials employed as biomaterials are metals and their alloys, ceramics and polymers. Polymers are too weak for load distribution (structural prostheses) and ceramics on the contrary have poor fracture toughness and are brittle. As far as hip joints are concerned, the load borne is 3 times the body weight. Load carried during strenuous activities like jumping is 10 times the body weight and the cyclic loads it carries is 10^6 throughout our lifetime [4]. Mechanical-biocompatibility is the term used to define the combined mechanical and biological property requirements considered while choosing a biomaterial [7]. It is critical to have materials that possess excellent mechanical properties and are biocompatible to the human body. Otherwise, implant materials often fail prematurely due to various reasons such as loosening via corrosion and/or stress shielding (as shown in Figure 1.2) which may lead to revision surgery that maybe expensive and painful. Thus, in order to produce a long-lasting implant, it is vital to consider the bio functionalities of the biomaterial prior to employing them.

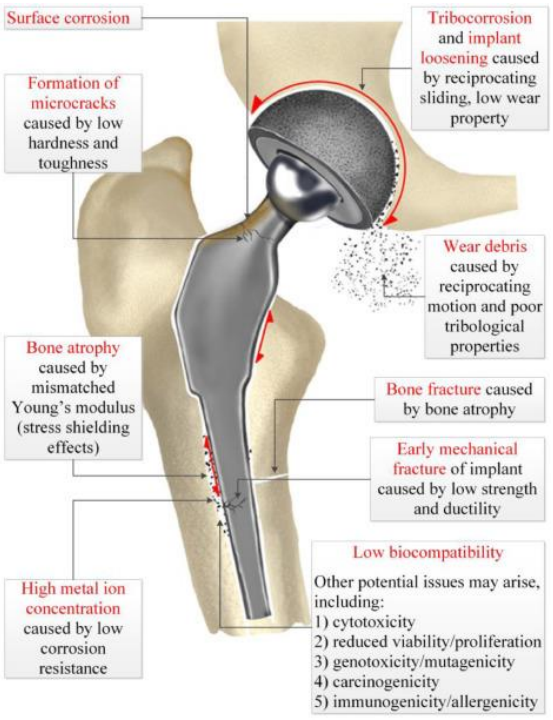

Figure 1.2 Possible mechanisms of failure of a hip implant [5].

As discussed above, metallic biomaterials are sturdier and are more viable in helping with the reconstruction of the damaged/failed hard tissue. It is to be noted that around 70-80% of the implants used for treatment of orthopaedic trauma are metallic biomaterials [8]. Despite impressive mechanical properties such as high UTS and relatively high fatigue strength metals possess, the concerning traits such as stiffness and biocompatibility (which is often measured qualitatively) give rise to atypical phenomenon such as the stress shielding effect. However, such a drawback can be overcome by careful consideration of alloying elements.

1.2 Metallic biomaterials

Among the available classes of materials, metallic biomaterials stand a good chance in being employed as structural implants for the remodelling of damaged skeletal tissues. Although there are few biocompatible metals, their contribution as independent materials is either insufficient or becomes unaffordable. Magnesium (Mg), for example, is biocompatible but due to the lack of the mechanical bio functionalities its usage is restricted for long term applications. However, Mg based alloys are used for short term bio-degradable implants. Similarly, Ni and its alloys with their super-plasticity properties have been used to make stents but are recently restricted on account of rising suspicions about its toxicity [9]. Precious metals such as Gold (Au), Silver (Ag), Platinum (Pt) are extensively used as dental implants but are constrained because of their huge cost. Tantalum (Ta) and Niobium (Nb) are excellent bioactive materials, whose contribution are far more significant as alloying elements than as independent biomaterials [5]. Table 1.1 shows the list of strength and Young's modulus of various metallic biomaterials.

Table 1.1 Comparison of mechanical properties of Bone with that of other metallic biomaterials [9].

Metallic Biomaterials	**UTS (MPa)**	**Young's Modulus (GPa)**
Co-Cr-Mo alloys	900-1540	240
316L stainless steel	540-1000	200
Ti alloys	900	105-125
Mg alloys	100-250	40-45
Cortical bone	130-150	10-30

The front runners among metallic biomaterials are stainless steel (SS 316L), cobalt-chromium alloys (Cr-Co) and Ti alloys (Ti). Till today, the aforementioned materials have been commercially employed as structural biomaterials for dental and orthopaedic applications. The successful use of SS 316L into total hip arthroplasty (THA) is credited to John Charnley's design that emerged in 1970s [10]. The initial success of the SS 316L in THA was observed only among young patients. Issues concerning aseptic loosening began to arise by 1990s and the nature of failure was identified to be corrosion induced fatigue [11]. After the application of SS for about 20 years it was validated not to be used as long-term implants. However due to the low cost, it is still widely preferred for various internal fracture fixation, bone screws/plates and intramedullary nails and rods. In addition to the issues regarding corrosion, the release of Ni and Cr into the blood stream is carcinogenic.

Cr-Co-Mo alloy aka Vitallium was initially used for dental application and later used in orthopaedics in 1940s [12]. It possesses excellent mechanical properties when compared to the SS 316L, mainly because of the presence of cobalt (Co). The huge cost of Cr-Co-Mo super alloy is a limitation in putting it to commercial use. However, 20% of the market still prefers the alloy because of its durability. With a downside to the very high mechanical properties, the high young's modulus (~240GPa) causes extensive stress shielding resulting in bone resorption.

Most of the commercial metallic THA implants are 5-6 times stiffer than bone [9]. The scale of stress shielding is directly dependent on the difference in the Young's modulus of that of the bone and the implant material. Stress shielding or aseptic loosening of the implant is a condition wherein the implant ends up carrying more load compared to that of the bone causing non-homogeneous load transfer. Since the remodelling of the bone is accelerated primarily by being subjected to loads, reduced distribution of load to the natural bone results in bone atrophy. Hence, lower the young's modulus the lesser the effect of stress shielding leading to the longevity of the implant [4]. Figure 1.2 represents the various mechanisms of failure.

Commercially pure titanium (C.P. Ti) possesses excellent corrosion resistance due to its affinity towards oxygen and has the lowest Young's modulus when compared with other metallic biomaterials. C.P. Ti is hence used for dental applications for its exceptional corrosion resistance [1]. The structure of Ti alloys is influenced by its alloying elements. Therefore, introducing a biphasic microstructure enhances its mechanical properties. Later, it was discovered that the β Ti alloys had higher fatigue strength and the lowest young's modulus (as low as 55 GPa) than both the α and α+β alloys. Niinomi et al. [7] observed that when a β Ti alloy based intramedullary rods was implanted in a rabbit, lower bone atrophy compared to SS 316L and best bone remodelling was observed.

Almost 42% of THR and 32% knee arthroplasty is due to the issues concerning aseptic loosening [13]. Employing Ti based alloys on such application will result in a pronounced improvement in the comfort of the patient and longevity of the implant.

1.3 Introduction to titanium

Ti is a greyish white metal with an atomic number 22. It is the fourth most abundant structural metal (after Al, Fe and Mg) accounting to 0.6% of earth's crust. The major sources of ore are Ilmenite ($FeTiO_3$) and Rutile (TiO_2) although suspicion of an oxide of an unknown element ($FeTiO_3$) was pointed out by Gregor in 1791. Not until the 20th century, the commercial large-scale extraction of Ti from $TiCl_4$ with the reduction of Mg in an inert atmosphere was discovered by Kroll. The texture of the resulting Ti was spongy and porous leading to be addressed as 'sponge Ti'.

The interest on the properties of Ti grew after the Second World War. By 1951, both the US and UK set out to develop various Ti based alloys for high strength and high temperature applications respectively. As an example, to the immense growth of Ti research, roughly 10% of the Boeing 777 airframe weight is Ti because most of the landing gears are made out of the high strength β alloy (Ti-10V-2Fe-3Al). It is worth mentioning that the most established applications of Ti and its alloys are the aerospace and biomedical sectors.

1.4 Metallurgy of titanium

Ti is a non-toxic, non-magnetic, biocompatible light metal. It's density at room temperature is 4.5 g/cm^3 which is about 60% of the density of stainless steel [14]. The strong affinity with oxygen provides excellent corrosion resistance for Ti. With an atomic number 22, Ti is transparent to X-rays for a voltage range of 60-125kV as the attenuation of X rays is proportional to the fourth power of the atomic number. Pure Ti exists in the form of a hexagonal closed packed (a= 2.95 Å; c= 4.68Å) structure called the α-Ti. However, at higher temperatures it undergoes an allotropic transformation to form a body centred cube (a= 3.32 Å) as can be seen from **Figure** 1.3. The temperature at which the transformation takes place is called the β transus temperature and its value is 882 ± 2^oC. The closed packed structure causes a distinct anisotropy which influences the mechanical behaviour of the material. Because of this, the value of Young's modulus various between 145GPa - 100GPa depending on the direction of the application of the load. The reason for the anisotropy is due to the packing

density of the atoms in the hcp and the BCC crystal structures. Due to a decreased c/a ratio of the Ti hcp (1.587) as compared to the ideal hcp structure (1.633) the density of atoms in the prism plane is greater than that of the basal plane thereby favouring slip on the former.

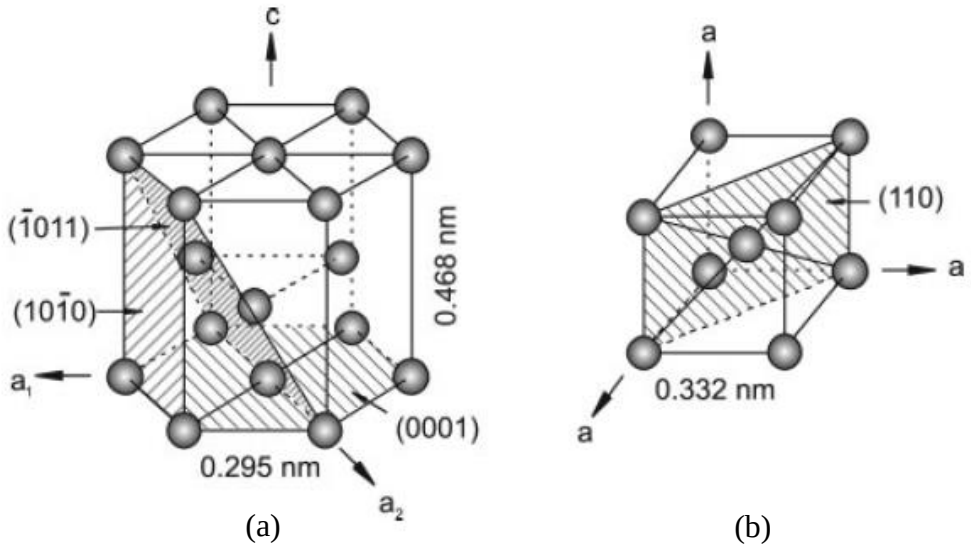

Figure 1.3 Allotropic structures of Ti: a) α-hcp and b) β-bcc [15]

The allotropic nature of Ti opens up a broad avenue for wide range of applications. The addition of different alloying elements has a corresponding influence on the β transus temperature. Based on its effect of the transus temperature they are classified as alpha stabilisers, β stabilisers and neutral elements. As seen in Figure 1.4, α-stabilisers usually expand the area of α phase field by increasing the β transus temperature. Interstitial elements (viz., C, N, O) along with Aluminium (Al) are regarded as α stabilisers. The β stabilisers help stabilise the β phase by lowering the β transus temperature. The β stabilisers are further classified into β isomorphous and β eutectoid. Mo, Nb, V, Ta are the β isomorphous elements and have good solubility with Ti. β eutectoid elements tend to form intermetallic compounds as they have poor solubility with Ti. Fe, Mn, Co, Cu, Ni, Si are common examples of β eutectoid elements. Zr and Sn are usually considered neutral elements and do not alter the transus temperature and contributes to increased strength .

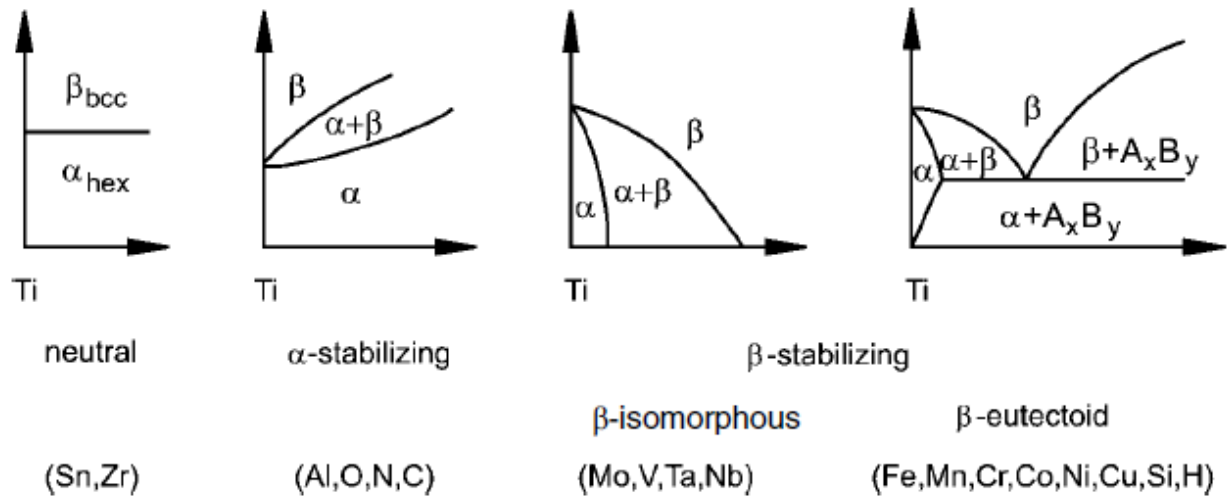

Figure 1.4 α, β and neutral stabilisers of Ti [15].

The strength of each alloying element in stabilising the β phase is quantified using a parameter called the Molybdenum Equivalent (MoE). This quantity is a combined measure of the effects of β phase stabilising elements, α phase stabilising elements, and neutral elements contained in a Ti alloy on the β phase stability. It uses [Mo] as an arbitrarily chosen baseline and normalizes other elements to an equivalent molybdenum value. It is represented in the equation (1-1) [16].

$$MoE = 1.0\,(Mo) + 0.67\,(V) + 0.44\,(W) + 0.28\,(Nb) + 0.22\,(Ta) + 2.9\,(Fe) + 1.6\,(Cr) + 1.25\,(Ni) + 1.54\,(Mn) + 1.60\,(Co) - 1.0\,(Al) \quad (1\text{-}1)$$

Wang et al [17] also proposes another MoE equation based on their experimental work and is stated in equation (1-2):

$$MoE = 1.0\,(Mo) + 1.25\,(V) + 0.59\,(W) + 0.28\,(Nb) + 0.22\,(Ta) + 1.93\,(Fe) + 1.84\,(Cr) + 1.5\,Cu + 2.46\,(Ni) + 2.26\,(Mn) + 2.67(Co) + 0.3\,Sn + 0.47\,Zr + 3.01\,Si - 1.47(Al) \quad (1\text{-}2)$$

1.5 Powder metallurgy of titanium

Powder metallurgy, commonly abbreviated as PM is a technique used in the production, processing and consolidation of fine metal powders into a solid compact [2]. The primary advantage of employing this technique is efficient usage of material thereby leading to cost effectiveness. Some of the key characteristics include repeatability, freedom with the design of

the alloy system (in terms of porosity and phases) based on the intended application. PM technique is a near-net shape technique similar to casting. Although, contrary to casting technology, PM is not limited by higher/lower melting point metals paving way for the inclusion of a wide range of materials with a higher material utility [2; 18]. Ti PM alloys was established in 1980s with two major approaches viz., Blended Elemental and Pre-alloyed method.

Blended elemental method is simple cold/warm press and sintering of powders to produce a dense solid. The elemental powders are then mixed well in order to have a proper blend of powders of different density. The mixed powders are then compacted either at room temperature or slightly higher temperatures (upto 250 ^{o}C). The pressed powders are called green compacts or green bodies and the corresponding density is called green density. This density is due to the mechanical interlocking of the powder particles due to the uni-axial load applied. The green bodies are subjected to sintering. The sintering temperature is usually 0.6-0.7T_m (T_m – melting point). Densification of the particles occurs during sintering. The sintered compacts can be subjected to thermomechanical processing.

1.5.1 HDH powders

Ti Metals Corporation patented the HDH (Hydrogenation-Dehydrogenation) process for powder production of Ti powders began around 1957 at [19]. HDH is a method to produce Ti powders from the sponges of Kroll (Mg) and Hunter's (Na) process, a two-step reversible process begins with the addition of hydrogen used as a temporary alloying element causing embrittlement. This allows the feedstock to be easily crushed, milled, and screened to a desired size target. After dehydriding, the mechanical properties of a ductile Ti powder are regained. It is known to be highly versatile and flexible with the ingot sources. The feedstock used is required to have a clean surfaces void of heavy surface oxidation or nitriding coating as they act as barrier for hydrogenation and a thickness less than 5cm is required. Thicker sources might need a second hydride operation. Ingots obtained via arc melting/electron beam melting can also be used. This may result in angular, blocky and denser powders.

Dehydriding may sometimes lead to sintering and the agglomerates formed during the dehydriding cycle are to be crushed/milled and screened to achieve the original particle size distribution. The whole process needs to be carried out as two lengthy vacuum processes and time spent at temperatures that encourage sintering should be minimized [20]. It is vital to

maintain an inert atmosphere in order to produce high quality powders with minimal interstitial elements.

1.5.2 Blended elemental method

The BE method involves the blending of elemental powders of desired compositions and then cold pressed into a shape, followed by sintering the compact to a higher density. The sintered shape may subsequently be subjected to hot isostatic pressing (HIP) to reach full density. HIP convolutes the residual porosity in the sintered shape by a combination of high temperature and iso-static gas pressure (Ar) resulting in a fully dense Ti alloy component with properties that are comparable to wrought material. In addition to the elemental powders, master alloy (MA) powders can also be used (albeit the pressing of MA powders is relatively challenging and expensive). Press and sinter approach is technically the simplest and the most attractive approach for near net shape or preform fabrication. This method provides the flexibility to select the powders from a wide range of specifications based on compatibility or affordability to be blended in to attain the targeted properties. It is known that the use of Ti based MMCs can effectively help improve fuel efficiency consequently reducing the carbon foot print. One of the major barriers to the adoption of Ti for automobile engine components has been its high cost and by employing PM processing, Ti components can be produced at lower cost compared to the conventional methods. The flexibility of PM manufacturing technology to produce a variety of near-net-shape components in sizes from a few grams to hundreds of kilograms has spurred the interest of industry [2].

Approaches such as tri-axial pressing [21], equal channel angle pressing and warm compaction [22; 23]are undertaken to improve the relative density of the green body and prevent high shrinkage several. Warm compaction can be defined as powder compaction performed at temperature above the RT but well below the recrystallization temperature [24]. It is a cost-effective method to produce ferrous and non-ferrous powder metallurgy alloys. The cost of warm compaction process is 25% higher than cold compaction and 40% [25] lesser than forging. The common range of temperature preferred for warm compaction is 130-150^{o}C [2]. Warm compaction aids improve green density better than cold compaction as the yield strength of the metals decreases at higher temperatures thereby favouring plastic deformation. Table 1.2 shows the effect of compaction pressure and temperature on the relative densities. In addition, the green strength of a sample has a linear dependence over the green density and higher green

density ensures better densification leading to reduced porosity preventing distortion in the dimension of the compact after sintering [26].

Table 1.2 Mechanical properties of various Ti alloys produced via warm compaction [27; 28]

Powder	Compaction temperature (°C)	Compaction pressure (MPa)	Relative density (%)
HDH Ti	150	392–1568	82.5–97.5
ME Ti-6Al-4V	150	783–1568	91.1–97.8
HDH Ti	200	200–1000	73.5–96.9
ME Ti-10V- 2Fe-3Al	200	400–800	80.3–89.5
PA Ti-10V- 2Fe-3Al	200	1000	79.8

1.5.3 Pressure-less sintering

The green compact that has been compacted is still expected to have residual pores. For dynamic applications, pore-free solids or small max pore size is required. In the aim to produce pore-free solids, the compacts are subjected to a densification process and is considered to be central to the BE method [29].Various processing routes to densification are hot pressing (HP), hot isostatic pressing (HIP) and (spark plasma sintering (SPS). Among these processes, sintering in a controlled gas atmosphere under vacuum is referred to as pressure-less sintering. The process is carried out in a low oxygen/nitrogen environment in the presence of high purity argon in order to prevent interstitial contamination that might lead to reduced tensile ductility [30]. It is notably vital to prevent the contamination of Ti alloys containing Nb and Mo as it is prone to form TiC on the grain boundaries causing embrittlement. The primary aim of the sintering process is to produce a compact that is nearly pore-free (with a minimum pore size of 10 um). The effective temperature for the sintering of C.P. Ti has been reported to be in the range of 1200 – 1350^{o}C [29]. Fine Ti powders can be sintered at lower temperatures as the size of the powders influences the sintering rate [31]. Having alloying elements with poor diffusivity can be challenging to the sintering process. Fe and O are reportedly fast diffusers whereas Al is a slow diffuser as can be seen from Figure 1.5 [32-34]. Apart from complete densification, solute homogenization is also considered important as it affects the mechanical properties. In the presence of both fast and slow diffusing alloying elements, the sintering rate of the alloy might sometimes be the same as commercially pure Ti.

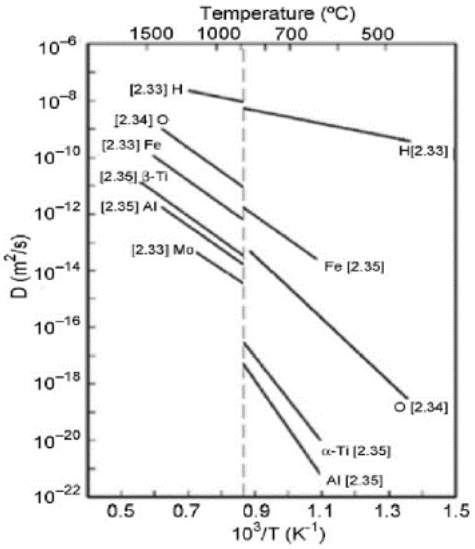

Figure 1.5 Diffusivities of different metals in Ti [14].

1.5.4 Microstructures of PM Ti alloys

Microstructure analysis in general involves chemical/compositional analysis, phase identification and morphological analysis. Size of the α/β grains, the width of the grain boundary is some of the parameters that are often observed. The microstructure of PM Ti alloys closely resembles an equilibrium state due to the lower cooling rate (10°C/min). Fig.1.7 provides a graphical representation of the nature of the phases formed at different conditions. In some cases, due to such low cooling rates, an alloy might respond in a way that is similar to annealing or aging resulting in intermediate phases aka omega phase (ω) specifically in β rich alloys. The common phases observed are alpha (α), beta (β), (α'') secondary alpha, primary alpha (α') and omega phase (ω) (isothermal or athermal). Of which the martensitic phases and the omega phase are considered to be metastable.

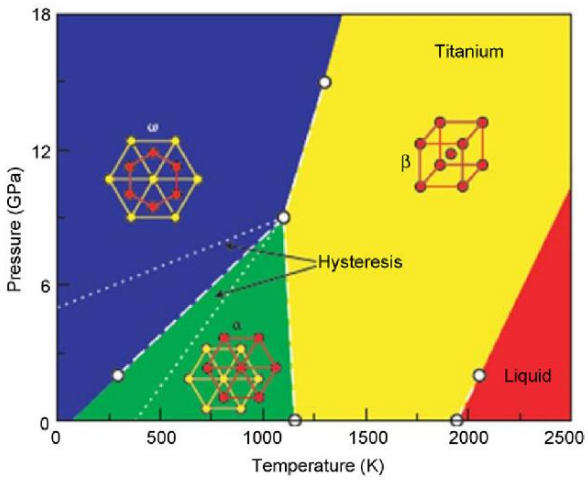

Figure 1.6 Formation of different phases (based on temperature and pressure conditions) [35].

Alpha phase (α) corresponds to the hexagonal closed packed structure with lattice parameters a= 2.8 Å; c= 4.7Å. The lattice parameters can be altered by the presence of interstitials (C, O, N) or substitutional alloying elements such as Al resulting in strain localisation causing solid solution strengthening. The morphology of the α phase is usually lamellar, equiaxed or acicular depending on the alloy chemistry and processing route. A phase can also be formed by the decomposition of the omega phase while aging.

Beta Phase (β) corresponds to the body centered cube. The size of the BCC unit cell is 3.3 Å. B stabilisers can be divided into two groups namely the isomorphous and the eutectoid groups. The eutectoid alloying elements have a poor solubility with Ti hence tend to precipitate in the matrix resulting in intermediate phases whereas the isomorphous group has good solubility to form solid solution.

Martensitic phases are a result of very high cooling rates up to 10^4K/s mostly observed among the alloys produced using additive manufacturing [36]. Among the phases, α' tends to form when there is low concentration of β stabilisers and α'' forms when there is a higher concentration of the β stabilisers. α' shows acicular/lamellar morphology and can be very similar to the α phase in terms of the lattice parameters [37] whereas the latter is an orthorhombic phase exhibiting mostly acicular morphology. The martensitic phases decompose into β which gets further decomposed into α or α+β phases.

Omega Phase (ω) is one of the metastable phases and have a hexagonal close packed structure the lattice parameters being a= 4.60 Å; c= 2.82Å. The metastable phase can be differentiated into two groups: athermal ω and Isothermal ω. While the isothermal ω is formed due to aging at lower temperatures, the athermal ω is independent of the heat treatment processes and is mostly dependent on the alloy design. The transformation between athermal and β can be reversed. The ω phase is usually present as fine 10nm particles and can be identified only using a TEM. It is known that addition of oxygen suppresses the formation of omega phase.

Chapter Two

Literature review

This section consists of a summary of the previous research conducted on the Ti-Nb based alloys produced for biomedical applications. The main purpose of this section is to understand the extent to which the Ti-Nb-Mn and Ti-Nb-Fe systems have been investigated and to identify various gaps in the research. Further, since the quantity of work conducted in the specific the ternary Ti-Nb-Mn and Ti-Nb-Fe systems is very limited, the binary systems of each individual alloying element along with Ti is reviewed. All the compositions reviewed in the following section are in terms of the wt %.

2.1 Binary alloys

2.1.1 Ti-Nb alloys

Ti is one of most favoured metallic materials for biomedical applications due to its high specific strength and biocompatibility [38]. Ti-Nb alloys generally are chemically inert, and possesses improved properties. One of the issues with using other metallic materials such SS 316L and Co-Cr alloys is the magnetic susceptibility. Co-Cr alloys show magnetic susceptibility approximately 7.5 times than that of Ti. Materials with high magnetic susceptibility causes disturbances during magnetic resonance imaging and is a discomfort to the patient [39]. Nb has been proven to be non-toxic when in direct contact with cells and aids relatively good cell growth and mitochondrial activity in studies conducted by Eisenbarth et al. [40]. Nb has also been found to enhance corrosion resistance as its oxides are highly stable in bodily fluids [41].

Zhao et al. [42] produced Ti-Nb alloys using MIM and the SEM images of the elemental powders are shown in Figure 2.1. Ti-(10,16,22) Nb alloys along with pure Ti were injection moulded followed by sintering at 1500^{o}C and held isothermally for 4h. The cooling rate was set to 10 ^{o}C/min. The as-sintered samples were then post processed by HIP at 915^{o}C at 100 MPa with a holding time of 2h.

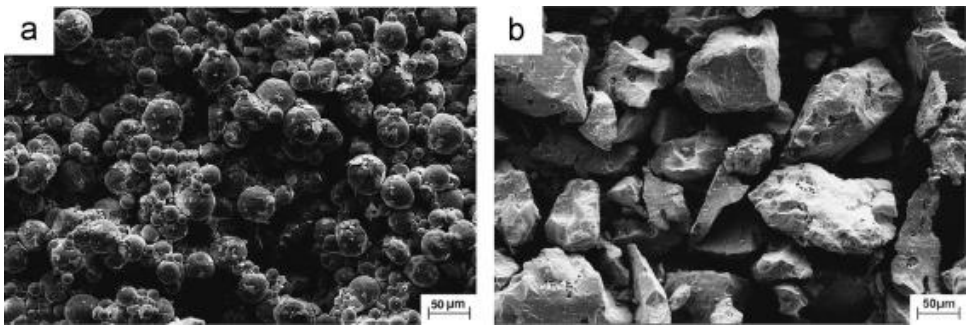

Figure 2.1 SEM micrograph of: a) Ti (<45µm) and b) Nb powders (<110 µm) for powder injection moulding [42].

X-Ray diffraction spectra as seen in Figure 2.2 indicates that the β peaks seem to become dominant with increase in Nb content while no intermediate phases were observed. The XRD spectra of Ti-16Nb produced by Yilmaz et al.[43] indicates that the alloy has a mixture of α and β peaks.

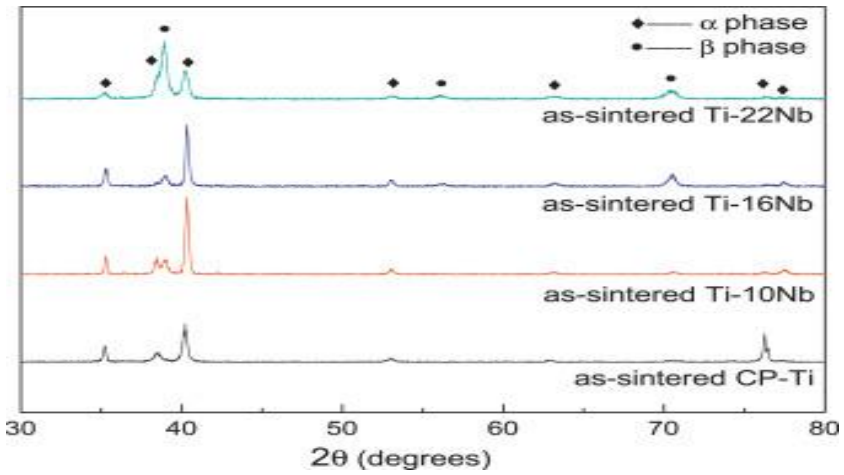

Figure 2.2 XRD spectra of Ti-(10,16,22) Nb [43].

German [2] claims that during sintering, finer particles contribute to faster diffusion (both surface and grain boundary) during sintering as larger particles leads to longer diffusion paths in relation to finer powder particles. Consequently, Yilmaz et al. [43] produced Ti-(16,28,40) Nb alloys through PIM with smaller Nb particles (30.5 µm) (Figure 2.3).

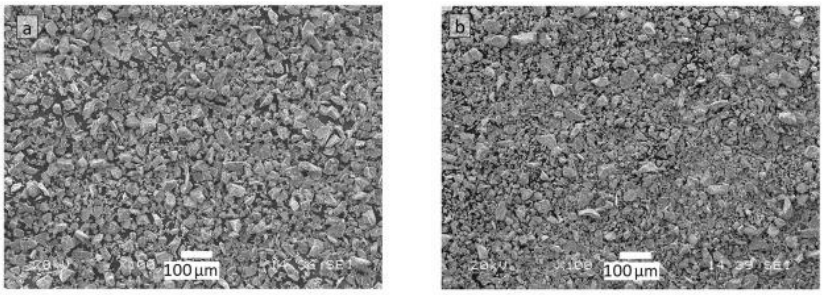

Figure 2.3 SEM micrograph of elemental: a) Ti powders (32.5 µm) and b) Nb powders (30.5 µm) used by Yilmaz et al. [43].

The optical micrographs (as seen in Figure 2.4) of Ti-Nb alloys reveals that C.P. Ti has the lowest porosity. The pores are seen to be rounded and unconnected whereas the other as-sintered samples seem to possess pores of range 10 - 40 µm. The increased porosity can be attributed to the large average particle size of the Nb particles as seen in Figure 2.3. Figure 2.4 also shows the presence of long acicular precipitates in the as-sintered samples. The composition of the precipitates was observed to be TiC_x particles.

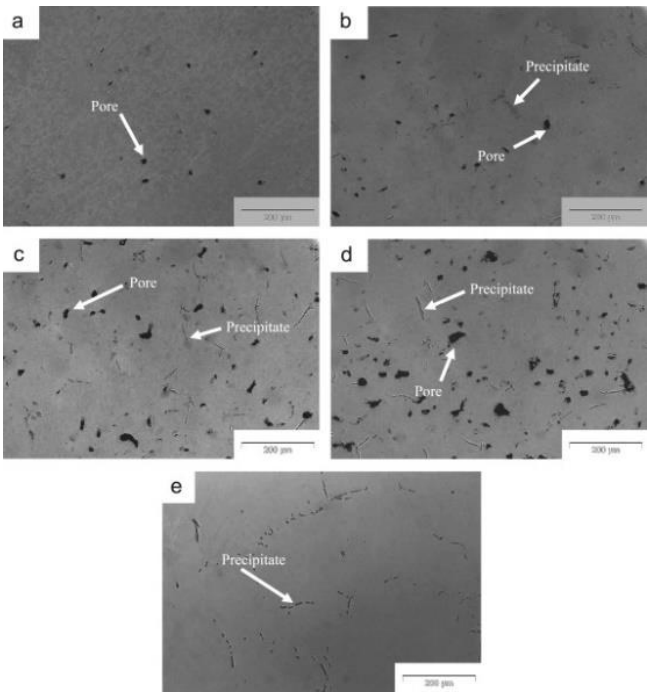

Figure 2.4 Optical micrograph of: a)as sintered C.P. Ti b) Ti-10Nb c) Ti-16Nb d) Ti-22Nb e) Ti-22Nb (as HIP-ed) [43].

The SEM micrographs of the as-sintered samples as observed from Figure 2.5 exhibit a conventional α+β Widmanstätten microstructure. With increased addition of Nb, refinement of the α grains was evident. Similar microstructure is exhibited by Ti-16Nb produced by powder injection moulding followed by vacuum sintering [43]. The TiC precipitates from Figure 2.4 were measured to be 5-10 µm in length and mostly observed along the grain boundaries. It is notable that the TiC is an FCC with a lattice parameter, a= 4.3 Å

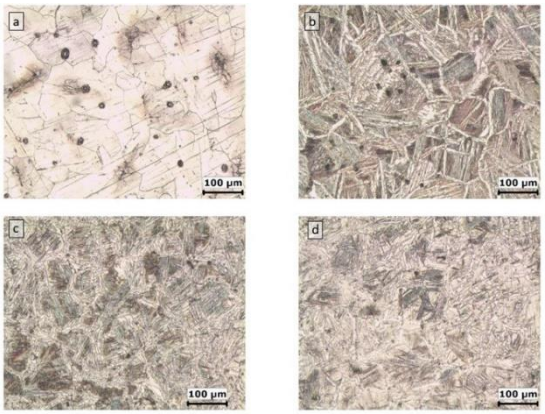

Figure 2.5 Optical micrograph of: a) CP Ti b) Ti-16Nb c) Ti-28Nb d) Ti-40Nb produced by Yilmaz et al. [43].

Table 2.1 summarises the mechanical properties of as sintered and HIP-ed C.P. Ti and Ti-xNb alloys. It can be noticed that strength increases with Nb content whereas the Young's modulus and elongation tend to decrease with the same. However, it is worth mentioning that the % elongation of the as sintered and HIP-ed samples, despite being similar presents a relatively higher increase in strength among the same samples. Such an increase is contradictory to that of Hon et al. [44] who claim that with an increase in Nb content from 12 wt % to 22 wt%, the strength increases from 700 to 750 MPa.

Table 2.1 Mechanical properties of Ti-Nb alloys produced by [42]

Composition	YS [MPa]	UTS [MPa]	Elongation [%]	Young's modulus [GPa]
as-sintered CP-Ti	435 ± 10	531 ± 14	17.2 ± 3.0	112 ± 2.0
as-sintered Ti–10Nb	552 ± 19	638 ± 12	10.5 ± 1.9	85.2 ± 9.0
as-sintered Ti–16Nb	589 ± 20	687 ± 20	3.58 ± 0.61	78.4 ± 5.6
as-sintered Ti–22Nb	649 ± 31	754 ± 7.0	1.43 ± 0.51	70.9 ± 7.2
as-HIPed C.P.-Ti	525 ± 1.5	586 ± 1.0	24.2 ± 2.2	116 ± 2.3
as-HIPed Ti–10Nb	612 ± 3.6	708 ± 4.5	9.63 ± 1.1	90.1 ± 6.1
as-HIPed Ti–16Nb	661 ± 14	739 ± 27	4.96 ± 0.31	82.2 ± 5.0
as-HIPed Ti–22Nb	687 ± 34	838 ± 14	1.30 ± 0.41	75.6 ± 7.6

In order to better understand the discrepancy, the fractographs of the samples were analysed. On observing the fractographs from Figure 2.6a, it is inferred that all samples have bimodal dimple microstructures that is reflective on the fracture surface. While some of the samples consist of coarse dimples similar to the size of the pores, it is clear that the dimples correspond to the porosity and the EDS data from the fractographs shows us the presence of TiC precipitates. A similar coarse dimple region can be seen in C.P. Ti in Fig. 2.6b. However, Ti-40Nb produced by PIM followed by sintering is characterised by finer dimples which is indicative of ductile fracture [43]. Also, the TiC precipitates located along the grain boundaries impede the movement of dislocations thereby causing poor ductility [42]. It is true in claiming that the effect of precipitates surpasses the effect of pores in terms of ductility. However, the reason for the drop of the Young's modulus can be partly attributed to the stabilization of β phase (with the addition of Nb) and partly due to the presence of porosity. The presence of carbide precipitates is also speculated to be the reason for the sudden rise in the Young's modulus of Ti-40Nb produced by Yilmaz et al. [43]. From Table 2.1 it is seen that with the addition of Nb, the values of Young's modulus measured through both nano-indentation and ultrasonic measurement does decline [43].

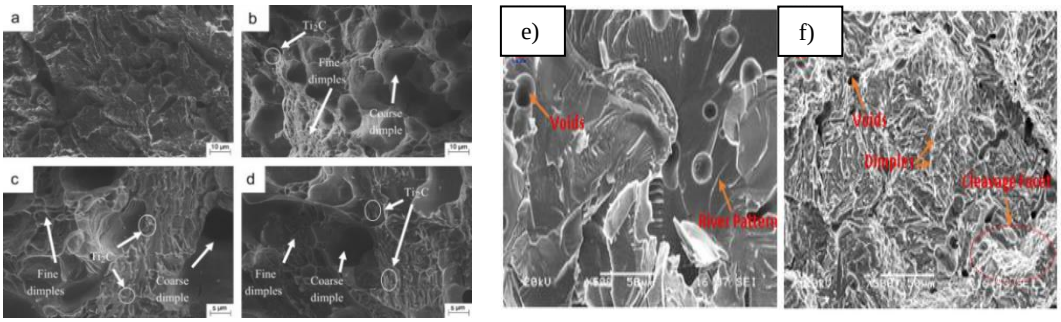

Figure 2.6 Fractography of: a) C.P. Ti, b) Ti-10Nb, c) Ti-16Nb, d) Ti-22Nb, [42] e) C.P. Ti and f) Ti-40Nb [43].

Ti-Nb alloys were produced by conventional powder metallurgy route where HDH Ti powders and Nb powders of size approximately 45 µm (Figure 2.7) were cold pressed at 600 MPa and vacuum sintered at 1350^{o}C with an isothermal holding time of 2h and a constant heating rate of 4^{o}C/min.

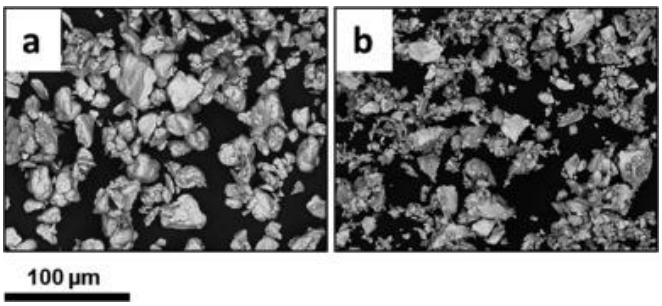

Figure 2.7 SEM micrograph of elemental: a) Ti and, b) Nb powders [45].

The X-ray diffraction peaks of the Ti-(33,40,56,66) Nb is displayed in Figure 2.8. It is evident that most of the peaks belong to the β phase except a few unidentified peaks with low resolution that are presumed to be α'' according to Chen et al. [45]

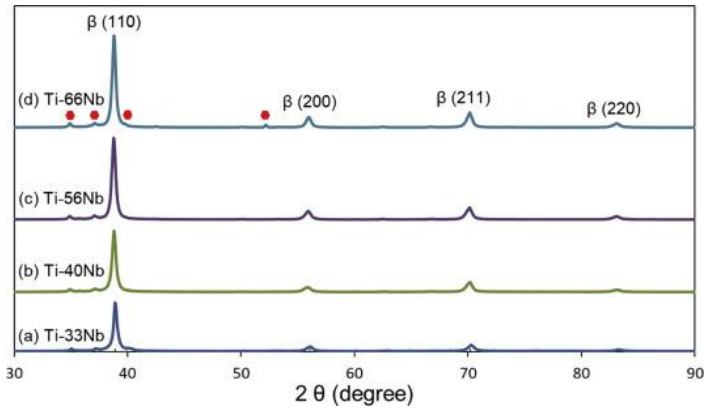

Figure 2.8 XRD spectra of Ti-33Nb, Ti-40Nb, Ti-56Nb and Ti-66Nb via conventional powder metallurgy route [45].

Figure 2.9 displays the SEM micrograph of Ti-(33,40,56,66) Nb alloys produced via BE method. The alloys are mainly characterised by acicular α phase distributed in the β phase. The dark regions in the micrograph corresponds to the pores and the regions with lighter contrast correspond to the β phase due to the presence of heavy atomic element Nb whereas the regions with a darker contrast represents the α phase. It is observed that the Ti-33Nb and Ti-40Nb has acicular α distributed along the grain boundary. However, a relatively denser α is found in Ti-40Nb produced by [43] as can be seen from Figure 2.9b. With the Ti-(56, 66) Nb the prevalence of the brighter contrast region is due to the presence of undissolved Nb powders during sintering. The reported self-diffusion coefficient for Ti at 1350^{o}C is around 5 X 10^{-8} cm^2/s [46]

while for Nb it is in the order of 10^{-14} cm^2/s [47]. Hence, it is evident that the density increases with the increment in Nb content and the reported porosity is slightly higher than that of other researches due to relatively larger average particle size of Nb, lower sintering time and lack of hydriding treatment of Nb. As hydriding the Nb powders prior to sintering has proven to increase diffusivity[48]; [49].

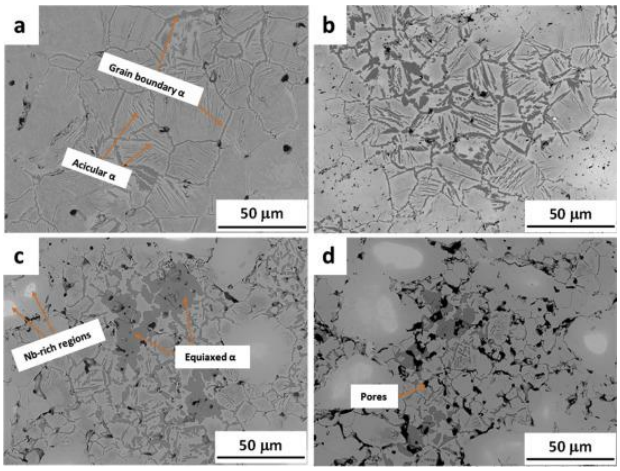

Figure 2.9 SEM micrograph of: a) Ti-33Nb b) Ti-40Nb c) Ti-56Nb and d) Ti-66Nb, respectively [45].

Figure 2.10 represents the mechanical properties of the Ti-Nb alloys and can be seen that the strength and Young's modulus decrease with increase in Nb content. This can be explained on the basis of SEM micrographs were the fine acicular α transform into an equiaxed α due to strengthening of the β phase. Inhomogeneous distribution of phases and undissolved Nb powders in Ti-(56, 66) Nb causes deterioration of mechanical properties as is evident from Figure 2.10

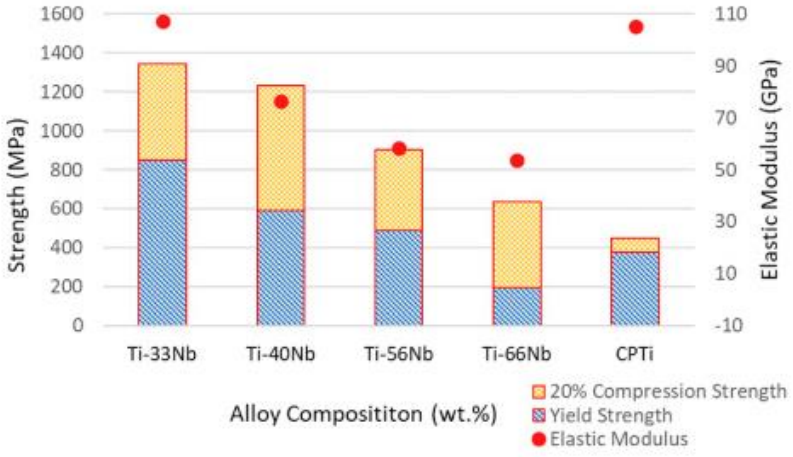

Figure 2.10 Mechanical properties of Ti- xNb alloys produced by Chen et al.[45]

The biocompatibility of the Ti- xNb alloys was investigated by seeding hMSCs (human mesenchymal stem cell) on the alloys for a period of 24h and compared with that of pure Ti. Figure 2.11 shows the MTT assay results and is evident that the amount of Nb influences the cell viability while Figure 2.12 display the fluorescent micrographs of the cell attachment network among the different Ti-Nb alloys. Ti-40Nb and Ti-56Nb exhibit the highest cell viability. With regards to the cell material interaction i.e. the attachment of the hMSCs via the actin filaments and the skeletal architecture, Ti-33Nb and Ti-40Nb exhibit well spread actin microfilament networks while Ti-56,66Nb show limited actin network (similar to that of C.P. Ti). Hence it is concluded that Nb content ranging from 40 to 56 wt% display pronounced cell adhesion and proliferation along with appreciable mechanical properties and can be used as a potential implant material.

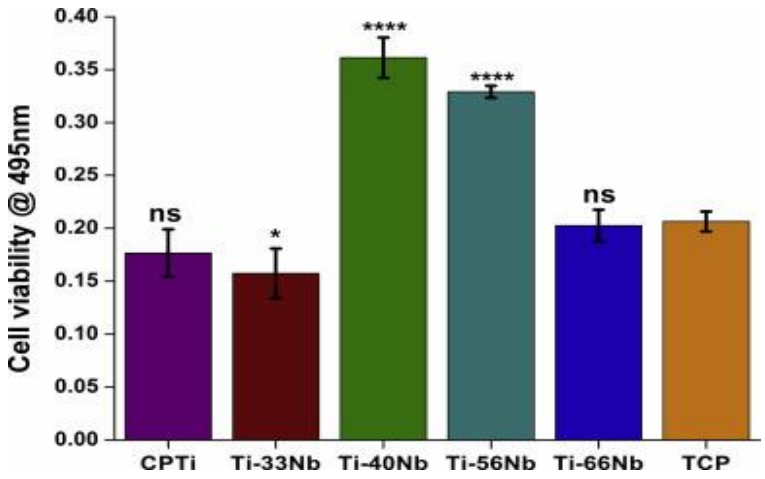

Figure 2.11 hMSC cell viability after 24h culture on C.P. Ti and Ti-xNb alloys produced by Chen et al. [45].

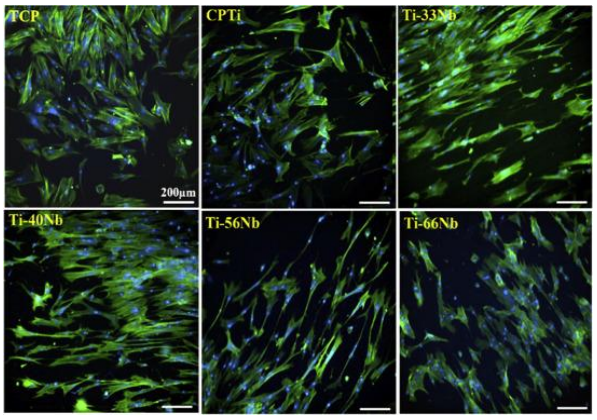

Figure 2.12 Fluorescent micrograph of the cell attachment behaviour of C.P. Ti and other Ti-Nb alloys produced by Chen et al. [45].

Although there have been many studies about the Ti-Nb binary system, it can be concluded that most of the binary alloys have high wt% of Nb and there are only a handful of research conducted on powder metallurgy. Therefore, the compositions for the current project are designed in order to further understand the effect of adding lower quantities of Nb (< 10wt%) and processing the alloys via powder metallurgy especially in a ternary system.

2.1.2 Ti-Mn alloys

Manganese (Mn) is a β stabiliser used to produce high strength Ti-Mn. Due to the abundant availability of the element, it becomes a cost-effective choice [50; 51]. Mn has been reported to improve bone resorption and osteogenesis [52]. Mn is also part of various essential mechanisms that regulates bodily functions [53] and is less toxic than Vanadium (V) [54].

Ti-(0,5,10,15,20) Mn alloys were produced by arc melting followed by solution treatment at a temperature 150^{o}C lower than that of the solidus temperature. The alloys were then allowed to cool down in the furnace at a rate of 10^{o}C/min approximately, until it reaches 600^{o}C after which they were air-cooled until room temperature. The XRD spectra as seen from Figure 2.13 indicates that C.P. Ti consists of a dominant α phase with lattice constants, a= 2.959 Å and c=4.703 Å (c/a=1.589). With 5% addition of Mn, the spectra displayed the presence of trace amounts of α-TiMn and β phase along with dominant α phase [55]. According to Alshammari et al. [56], Ti-5Mn showed no presence of α-TiMn both with the as-sintered and β forged samples. However, Santos et al. [57] reported that Ti-6Mn consists of ω (002), ω (112), α or α' (100) (101) as can be seen from the Figure 2.13. For Ti-8Mn and Ti-9Mn produced by MIM followed by solution treatment, only β peaks can be observed [51]. For Mn content ranging from 10wt %, prominent β peaks were observed as the α phase gradually diminished. A similar behaviour has been observed in Ti-10Mn produced by vacuum sintering where the β phase remains as the dominant phase after adding 10wt% Mn. Ti-5Mn has a c/a factor = 1.759 Å which is different from the usual c/a factor of that of a hcp indicating the presence of a distorted martensitic hexagonal closed pack structure. Kim et al. [55] reported that due to the atomic radii of Mn being

lower than that of Ti, the diffraction angle on β (110) plane shifts from 39º5 for (Ti-10Mn) to 39º9 for (Ti-20Mn) similar to [57] were Ti- (8,9,12,13,15,17) Mn (wt%) also exhibit a shift in the diffraction angle.

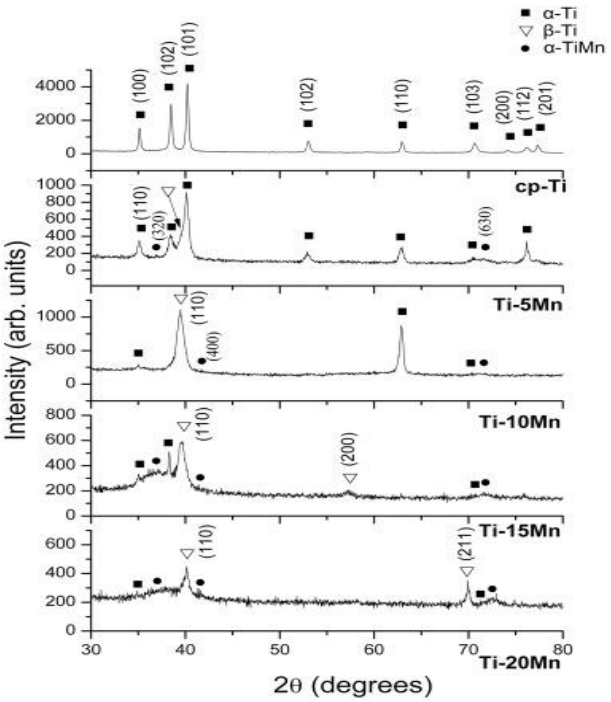

Figure 2.13 XRD spectra of Ti- (5, 10, 15, 20) Mn samples [55].

Ti-1Mn produced by vacuum sintering was characterised by lamellar microstructure as can be seen in fig. 2.13. With increase in Mn content, the lamellar tend to become finer with reduced inter-lamellar spacing and increased size of the grain size [56]. Ti-5Mn produced by was characterised by Widmanstätten microstructure which is typical of an α+β alloy (Figure 2.14, Figure 2.15, Figure 2.16). It is notable that Ti-5Mn after β forging consisted of elongated β grains and the texture can be attributed to the hot working. On the contrary, 6wt% Mn produced fully stable β grains with grain size 190 ± 20 μm (Figure 2.15). However, according to [51], the average grain diameter of the Ti-Mn alloys was similar of the range 69.8 ± 6.1 μm.

Sintered Ti-10Mn alloy is characterised by equiaxed microstructure with acicular α along the grain whereas Ti alloy with 10% addition of Mn produced by arc-melting slowly transforms to a non-lamellar structure due to bainite reaction [58]. For Ti-15Mn and Ti-20Mn, the microstructure is dominated by the β phase with some acicular α phase. The Ti-

18Mn alloy seem to possess grain size of about 418 ± 7 µm. Ti-(6,9,13) Mn have been reported to have almost similar grain sizes [57].

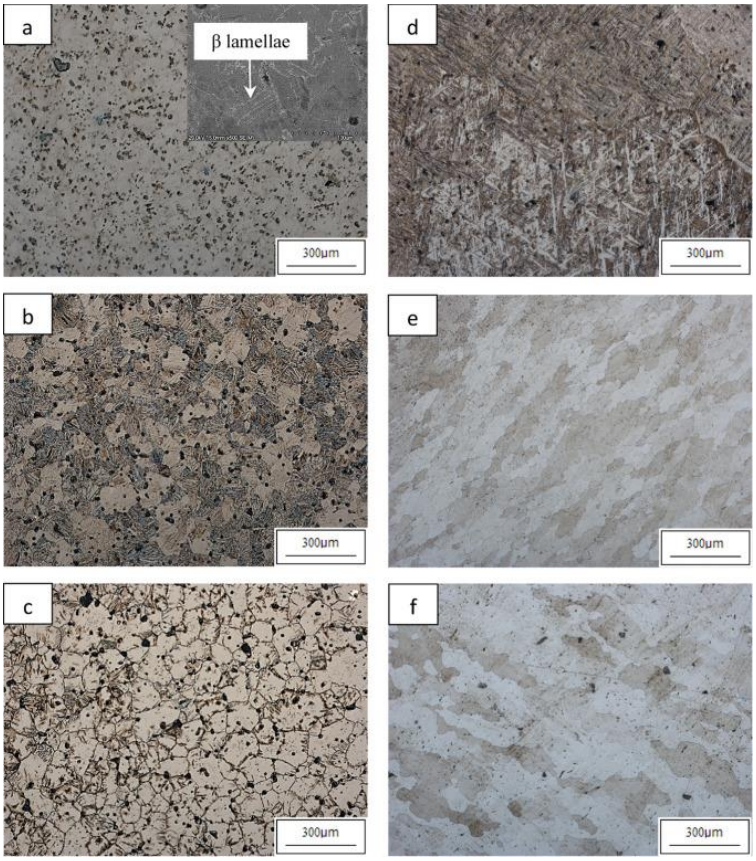

Figure 2.14 Optical micrographs of Ti-(1,5,10)Mn: (a-c) as sintered (d-f) β forged, respectively [56].

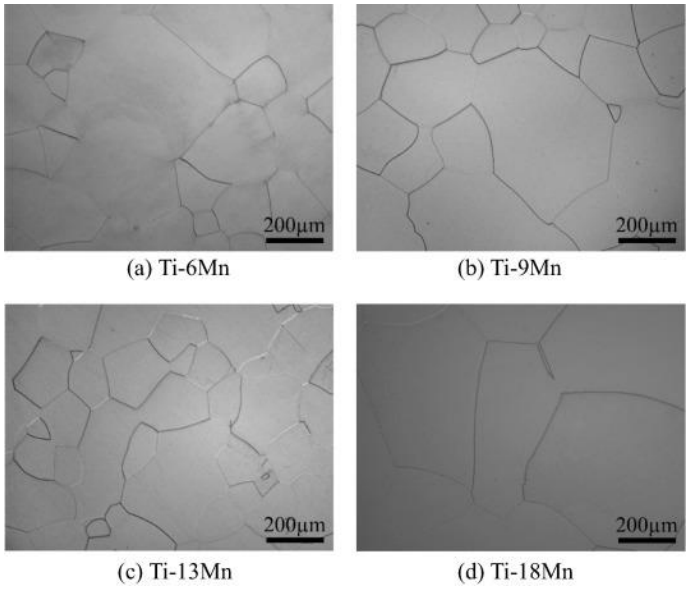

Figure 2.15 Optical micrograph of Ti-(6-18) Mn produced by Santos et al., via CCLM [57].

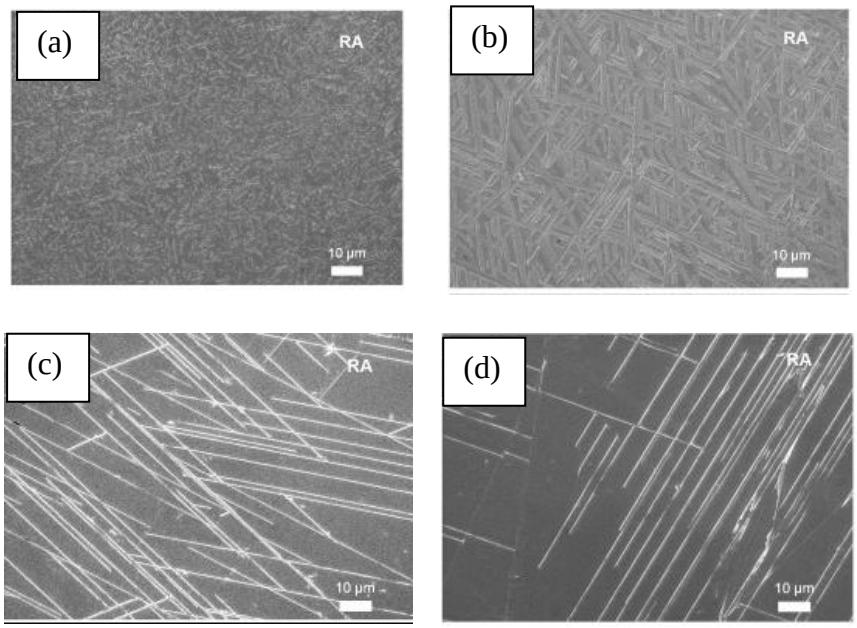

Figure 2.16 Optical micrograph of: a) Ti-5Mn, b) Ti-10Mn, c) Ti-15Mn and d) Ti-20Mn by Kim et al [55].

Ti-5Mn has been reported to have the highest hardness values (457 HV) among the Ti-(5,10,15,20) Mn alloys. The reason has been attributed to solid solution strengthening effect of Mn and the presence of athermal ω phase [55]. Similarly, Ti-6Mn seems to have a hardness of 469 HV. However, for Ti-9Mn addition, the Vicker's hardness value is reported as 338 HV. Ti-(10,15,20) seem to have similar hardness values ranging from 384 -398 HV. The β forged Ti-10Mn alloy has a hardness of around 415 HV [59]. The Ti-(8,9,12,13,15,17) Mn alloys produced by MIM [51] seem to possess a similar Vicker's hardness ranging between 291 HV to 317 HV. The Ti-13Mn alloy produced by CCLM followed by hot working and solution treatment shows a hardness value of 312 HV. This can be due to the stabilisation of β phase.

For Ti-5Mn, an increase in strength to around 850 MPa is observed. While the same sample when β forged experience a further spike in the strength (1250 MPa) mainly due to closing of the existing porosity (Figure 2.14). Ti-9Mn presented an ultimate tensile strength of around 1000 MPa with an elongation of 5% and 17% as seen in Figure 2.18. The reason for the low ductility in the former can be attributed to the presence of carbide precipitates and porosity as they were produced via MIM while the latter was produced by CCLM [32; 57]. Ti-13Mn by Santos et al. [57] exhibited tensile strength of around 950 MPa and an elongation of 13% while the Ti-13Mn alloy produced by metal injection moulding showed a similar tensile strength but had a brittle fracture. The reason for such a behaviour is due to the presence of precipitates that blocked the movement of dislocation similar to that of Ti-9Mn. A similar behaviour is observed

with Ti-17Mn and 18Mn alloys where the strength has dropped to less than 400 MPa as seen in Figure 2.18.

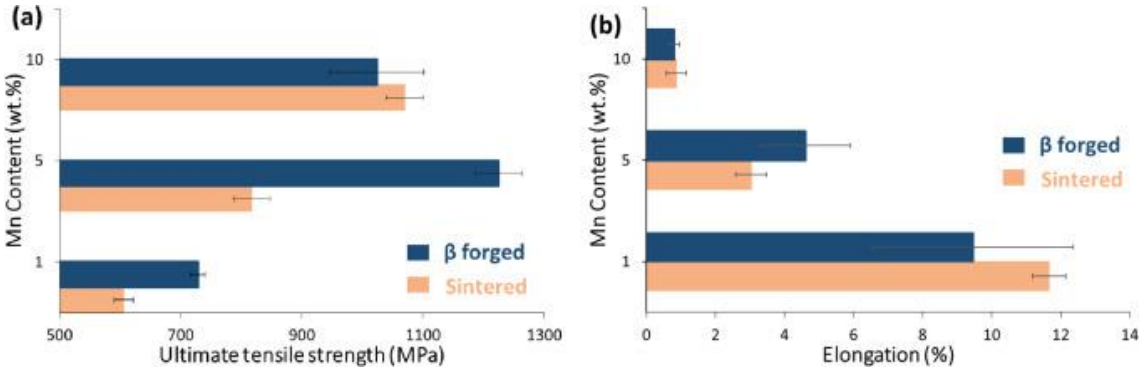

Figure 2.17 Mechanical properties of Ti-(1,5,10) Mn by a) as sintered and b) β forged, respectively [56].

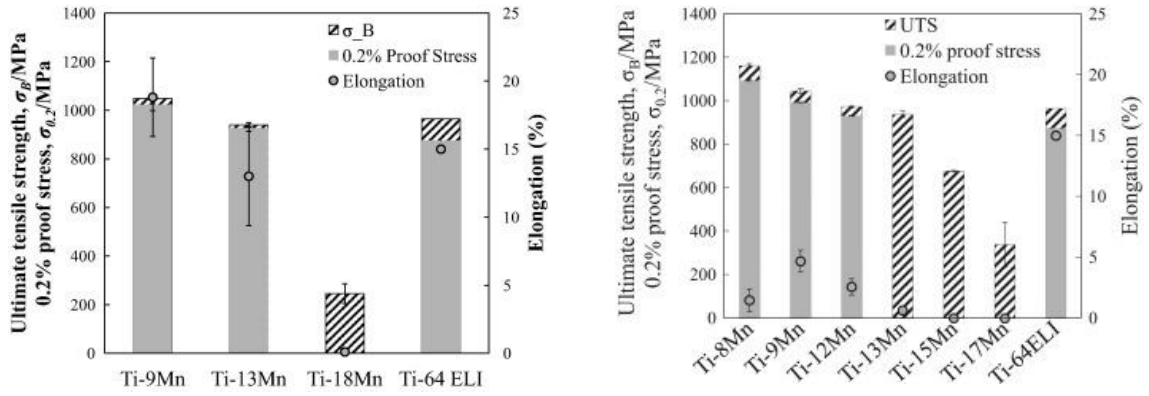

Figure 2.18 a) Mechanical properties of Ti-(9-18) Mn by CCLM and b) Mechanical properties of Ti-(8-17) Mn by MIM [51; 57]

Ti-(1,5,10) Mn alloys produced by BE element exhibit a Young's modulus of around 97 ± 4 GPa and it is notable that β forging did not affect the Young's modulus values [56]. However, Ti-5Mn alloy produced by arc melting has a Young's modulus of around 130 GPa. This difference can be attributed to the presence of the athermal phase as shown in Figure 2.19. A similar behaviour is seen in Ti-6Mn alloy. With further addition of Mn content despite a few differences, all alloys exhibit a Young's modulus close to about 100 GPa which is lesser than Ti-6Al-4V -ELI [56].

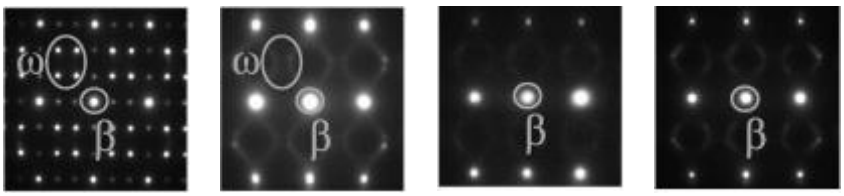

Figure 2.19 Selective area electron diffraction of: a) Ti-6Mn b) Ti-9Mn c) Ti-13Mn d) Ti-18Mn, respectively [57].

Santos et al. [57] investigated the ion release and cytotoxicity behaviour of Ti-(6,9,13,18) Mn alloys produced by CCLM. The ion release behaviour was tested under two solutions viz., $HBSS^{+}$ solution and 1% lactic acid solution. It was inferred that the amount of Ti and Mn ions released onto the $HBSS^{+}$ solution (0.06 µg/cm^2 and 0.015 µg/cm^2, respectively) was similar for all Ti-Mn alloys and the ion release into the 1% lactic acid solution was dependant on the Mn content. Ti-6Mn had the minimum ion release of 0.18 µg/cm^2 and Ti-18Mn had the maximum of 0.88 µg/cm^2. The representative graphs are presented in Figure 2.20**.**

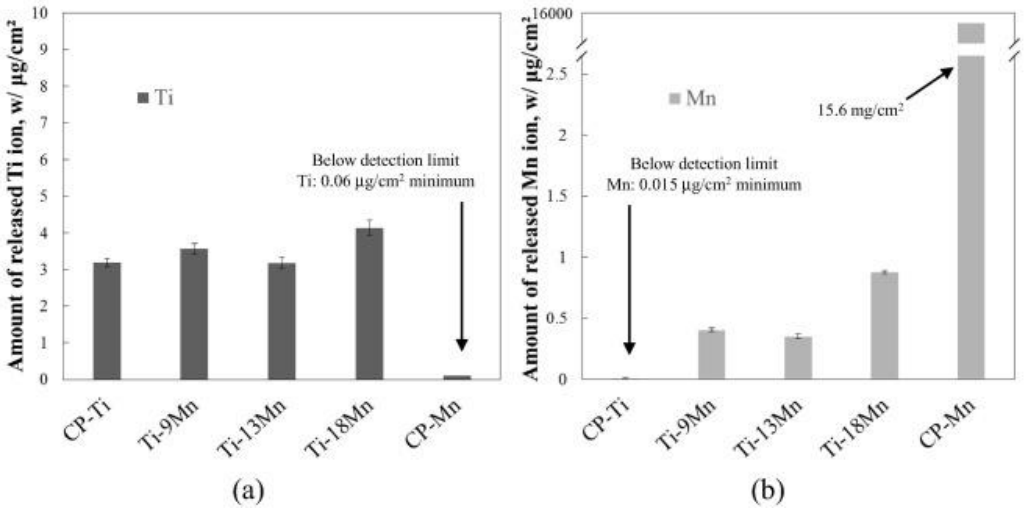

Figure 2.20 Ion release behaviour of Ti-Mn alloys in: a) $HBSS^{+}$ solution b) 1% lactic acid solution [57]

The cytotoxicity of the alloys was tested by exposing the metals to the MC3T3-E1 assay and the viability of the cells were observed after 24h and 72h of exposure. No significant difference in cell growth and viability is seen the Ti-Mn alloys after 24h. However, after 72 h relatively poor cell attachment was seen in Ti-13Mn and Ti-18Mn as shown in Figure 2.21. The results of the ion release behaviour can be correlated with the cell viability assay and the poor cell attachment can be due to the increased release of Mn ions.

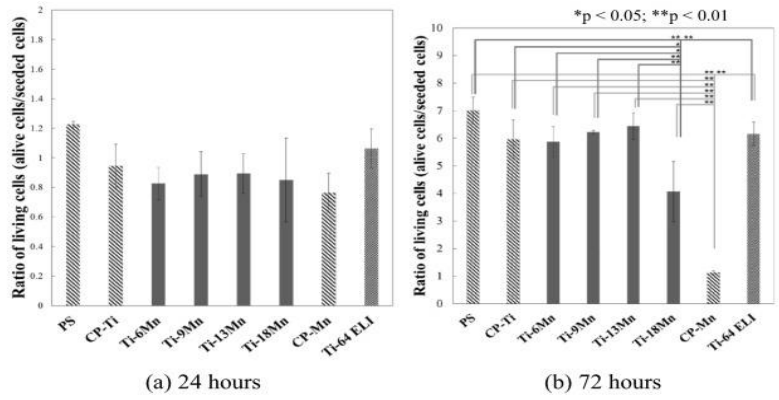

Figure 2.21 Cell viability assay after: a) 24h b) 72h of exposure to the metals, respectively [57].

It can be seen from above that there has been a wide range of research conducted on the Ti-Mn binary system. However, most of the research is conducted via casting and injection moulding. In order to understand the behaviour of the Ti-Mn alloys in the presence of Nb the compositions are designed in such a way that the gaps in the previous research is filled and the α+β and metastable region is majorly exploited.

2.1.3 Ti-Fe alloys

Ti alloys are widely used for medical devices due to its high specific strength, good corrosion resistance and biocompatibility [60; 61]. Fujii and Maeda reported that the tensile strength of Ti alloys containing Fe is much higher than conventional Ti alloys containing costly β stabilizing elements such as V [62]. Fe is an effective β stabiliser and helps to enhance the strength as it is a substitutional solid solution in the β matrix. With a high diffusion rate in Ti, Fe can be homogenized quickly while sintering [63]. Liu et al. [64] reported a remarkable increase in tensile strength and elongation with Fe more than 3wt%. Despite having the highest β stabilising strength among the other elements (Ta, Cr, V, Cu) usage of Fe is limited due to segregation of Fe while casting due to high density [36]. Powder metallurgy provides a remedy to such an issue as it is a solid-state processing route. Being abundantly available, addition of Fe to an alloy system results in the overall cost reduction of the material. Fe is a non-toxic, non-allergenic biocompatible β stabiliser [65].

Chen et al. [66] studied Ti- (3, 5, 7) Fe (wt%) that were produced by cold pressing and vacuum sintered by being isothermally held for 2h at 1150 ^{o}C. Gas atomised Ti and carbonyl Fe powders of size 25.2 and 3.4 µm were used. All the alloys achieved an overall relative density of above 96%. A few Kirkendall pores were found and is due to high diffusivity of Fe. It is

notable that all the pores were spherical and small. The spheroidization of the pores is identified to be due to the decrease in surface energies. Besides the usage of fine Fe powders and the choice of sintering temperature is attributed to the high relative density.

Figure 2.22 shows the XRD spectra of Ti-3Fe, Ti-5Fe and Ti-7Fe and it is seen that with the addition of Fe, the more β peaks were visible. This is evidence that Fe is a β stabiliser. Also, the addition of Fe suppressed the eutectoid reaction since no TiFe peaks were identified.

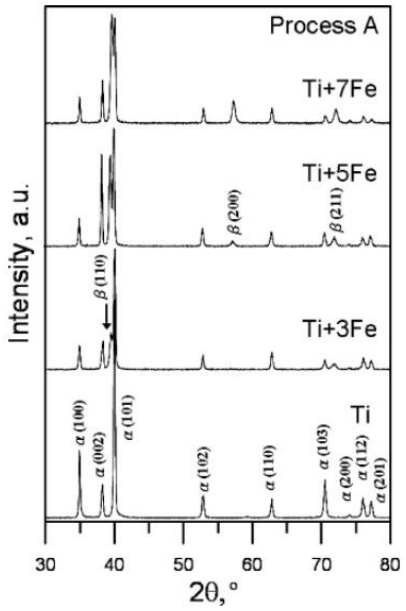

Figure 2.22 XRD spectra of Ti-3Fe, Ti-5Fe and Ti-7Fe produced by Chen et al [66].

Figure 2.23 shows the micrograph of Ti-3Fe, Ti-5Fe and Ti-7Fe and it is seen that the alloys are characterised by lamellar structure and the interlamellar spacing decreases with the addition of Fe. Addition of Fe also increases the strength and hardness at the expense of ductility.

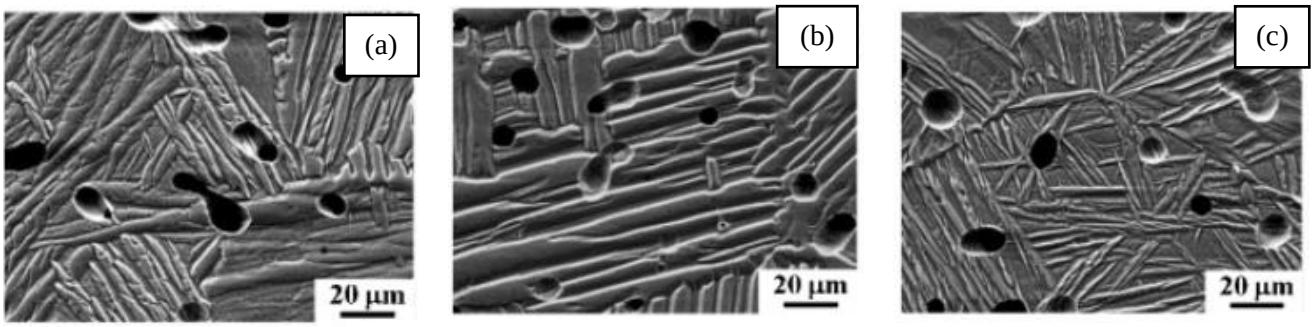

Figure 2.23 Micrograph of a)Ti-3Fe b) Ti-5Fe c) Ti-7Fe, respectively produced by Chen et al [66].

According to the Ti-Fe phase diagram [36], the maximum solubility of Fe in Ti is upto 7wt%. Addition of further Fe causes the formation of TiFe intermetallics. Therefore, there has been numerous researches conducted on Ti-Fe binary alloys and most of the research concludes that the addition of Fe, causes an increase in the proportion of β phase which results in refinement of the lamellae and the strength gradually increases as a consequence. Further, the hardness values also increase at the cost of ductility[67-69].

Among the binary Ti-Nb, Ti-Mn, Ti-Fe alloys, it is seen that most of the work is based on casting and injection moulding. For the Ti-Nb alloys, most of the work is conducted with large wt% of Nb and for the Ti-Mn system, most of the alloys seem to contain metastable phases.

2.2 Ternary alloys

2.2.1 Ti-Nb-Mn alloys

Ehtemam-Haghighi et al. [70] produced Ti-xNb-7Mn via the conventional powder metallurgy route. Ti and Nb powders with average particle size <50 μm and Mn powders of average particle size <10 um were chosen. SEM images of the elemental Ti, Nb and Mn powders are shown in Figure 2.24. The powders were chosen to have irregular morphology so as to facilitate mechanical interlocking which helps increase the green density of the samples. The mixed elemental powders were cold pressed at 550 MPa and vacuum sintered at 1170 ^{o}C at a heating rate of 4 ^{o}C/min while being isothermally held for 8h.

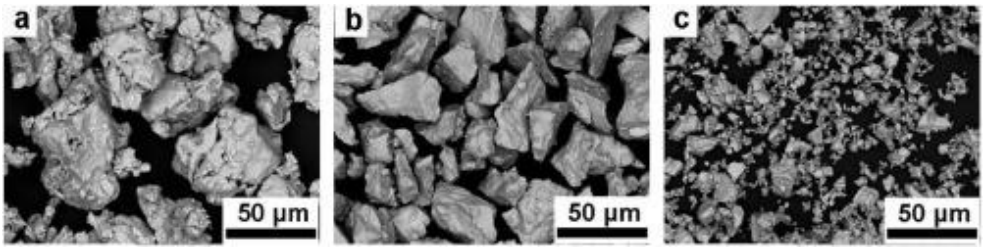

Figure 2.24 SEM micrograph of elemental a) Ti, b) Nb and c) Mn powders, respectively [70].

From the XRD spectra shown in Figure 2.25, it can be observed that the Ti-7Mn-xNb alloys exhibit peaks corresponding to both α and β phases with increase in the latter with increase in Nb content indicating β stabilisation. The ratio of the volume fraction of both the phases along with their lattice parameter is summarised in Table 2.2. It can be seen that the lattice parameter increases with the addition of Nb. As a result, the peaks tend to shift to a lower angle. The

reason for such behaviour can be attributed to higher atomic radii of Nb in comparison to Ti [71]. Decrease in density with increase in Nb content is due to the poor diffusivity of Nb in Ti matrix [14]. Owing to the relatively poor diffusivity of Nb compared to Mn, finer powders of size <50 μm were chosen as finer powders tend to sinter better due to higher surface area compared to coarse powders [42].

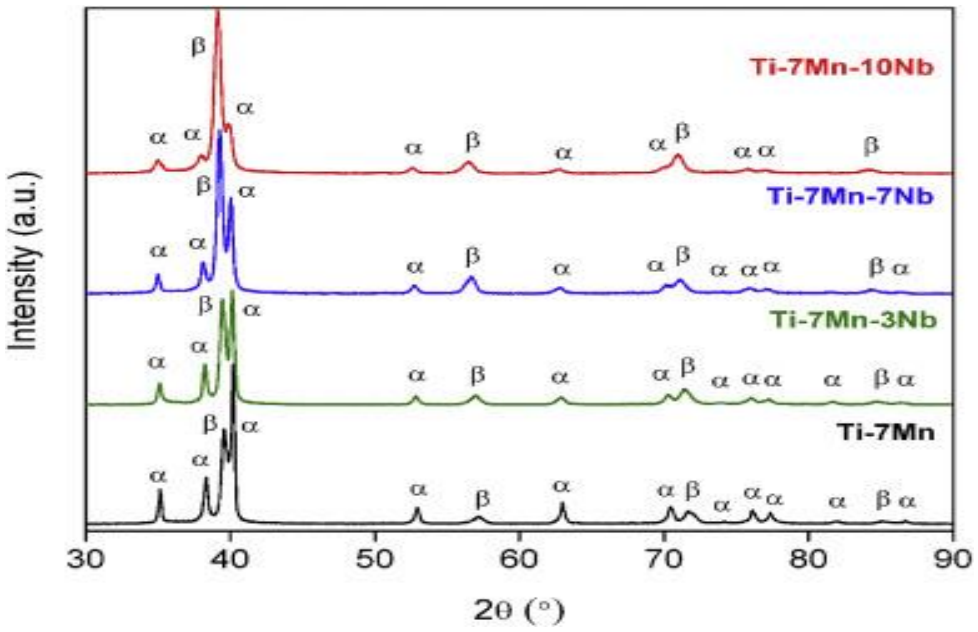

Figure 2.25 XRD spectra of Ti-7Mn-xNb produced by BE method [70].

Table 2.2 Volume fraction and relative density of Ti-7Mn-xNb alloys [70].

Alloy	α phase V_f (%)	β phase V_f (%)	β phase *a* (Å)	Relative density (%)
Ti-7Mn	61	39	3.219	96.31 ± 0.07
Ti-7Mn-3Nb	52	48	3.234	96.23 ± 0.06
Ti-7Mn-7Nb	39	61	3.246	96.12 ± 0.07
Ti-7Mn-10Nb	30	70	3.250	95.90 ± 0.11
C.P.-Ti	100	–	–	95.16 ± 0.10

The SEM images of the Ti-7Mn-xNb alloys are presented in Figure 2.26. It is clear that the alloys consist of a dual phase microstructure with the dark regions corresponding to α phase whereas the lighter regions constitute the β phase. Spherical and elongated pores can also be seen along the grain boundaries. Comparing the images, it is evident that the addition of Nb causes refinement in the coarse α-lamellae as the addition of Nb helps stabilise the β phase

while impeding β → α transformation [72-74]. The EDS maps of Ti-7Mn-10Nb shows the dark regions indicating the lack of a particular element. Line scan analysis shown in Figure 2.27 reveal a region of bright contrast (due to the presence of heavy atomic number: Nb). This can be due to the incomplete diffusion of undissolved Nb powders. However, Mn has seemed to be completely dissolved in the Ti matrix. Despite Ti-7Mn-10Nb, all other alloys seemed to be homogeneously blended as no unusual peaks were observed Figure 2.27**.**

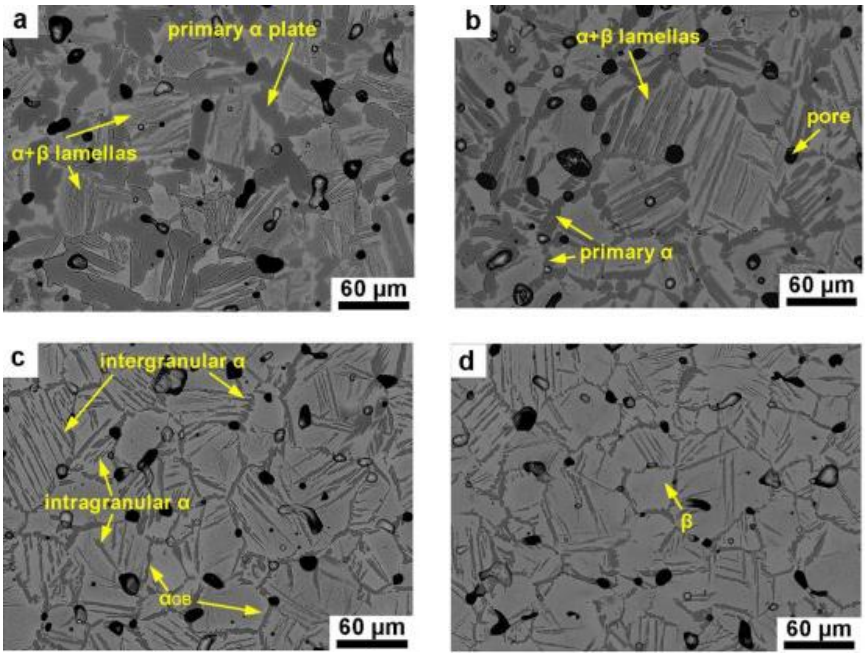

Figure 2.26 SEM micrographs of a) Ti-7Mn, b) Ti-7Mn-3Nb, c) Ti-7Mn-7Nb and d) Ti-7Mn-10Nb, respectively [75].

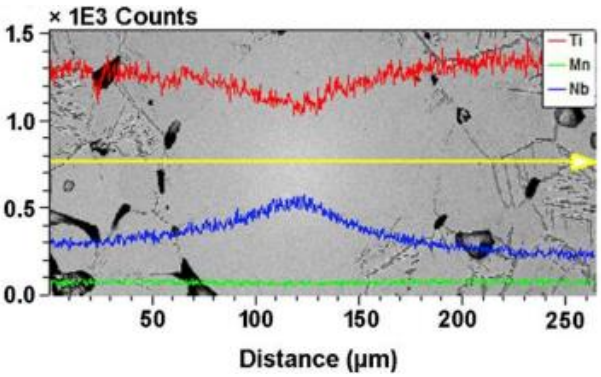

Figure 2.27 EDS of Ti-7Mn-10Nb [75].

Figure 2.28a display the mechanical properties of the Ti-7Mn-xNb alloys. Ti-7Mn alloy has a higher strength compared to C.P. Ti due to the addition of Mn. However, addition of Nb increases the elongation strain while decreasing the yield and ultimate compressive strength. Correspondingly, the Vickers' hardness (HV) and Young's modulus (E) also decreases with

the increase in Nb content. It is reported that the addition of Nb reduces the bond strength of the β crystal lattice and helps stabilises the β phase thereby directly affecting the Young's modulus. In order to study the nature of fracture, the surface of Ti-7Mn-10Nb was observed using an electron microscope. The microcracks observed in Figure 2.28b is due to the presence of pores at the point of fracture. Absence of interface powder particles suggest complete metallurgical bonding [75].

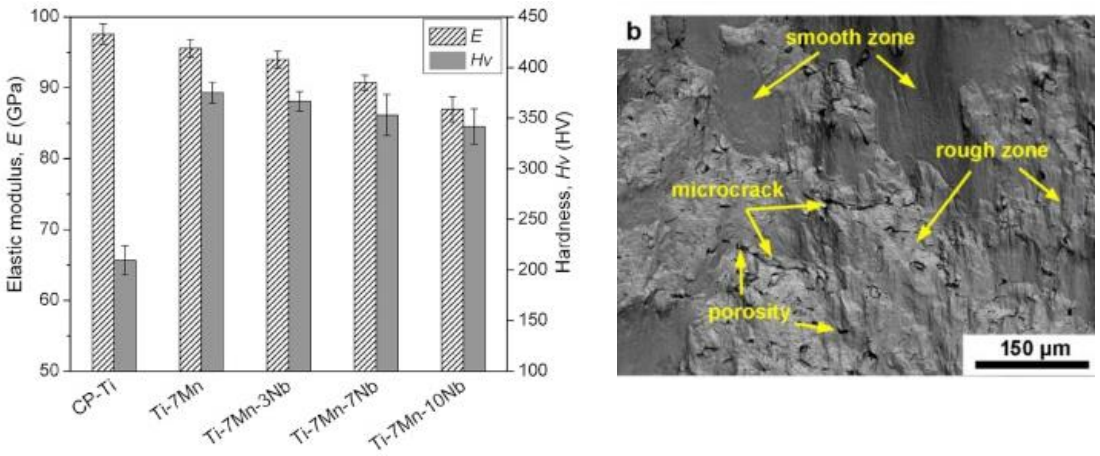

Figure 2.28 a) Young's modulus and Hardness of Ti-7Mn-xNb alloys and b) SEM fractograph indicating the ductile and brittle regions of fracture, respectively [75].

Ti-26Nb- (0,1, 4, 6, 8, 10) Mn wt% alloys were produced by Cold Crucible Levitation Melting in argon atmosphere. The metals were melted four times for homogeneity before cold rolling to achieve a thickness reduction of 60%. The cold rolled sheets were then solution treated at 900 ^{o}C for 30 min after which they were quenched in ice water [50].

The XRD spectra (Figure 2.29) indicated that the crystal structure is dependent on the Mn content. Ti-16Nb comprised of α'' and β phases. Addition of 1 wt% Mn gradually suppressed α''phase. However, at 4wt% and greater the athermal ω phase and the martensitic α'' phase disappeared making the β phase to be the only dominant phase. No diffraction peaks corresponding to athermal ω phase was observed except Ti-16Mn-1Mn. The lattice parameters of the orthorhombic α'' is a = 3.166 Å, b = 4.854 Å, and c = 4.652 Å.

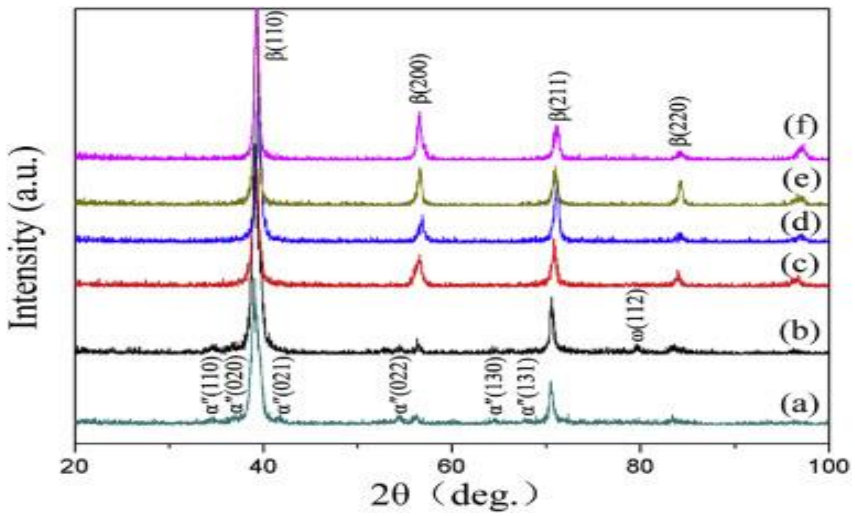

Figure 2.29 XRD spectra of a) Ti-26Nb-(0, 1, 4, 6, 8, 10)Mn [50].

In accordance to the XRD spectra, the Ti-26Nb-xMn alloys exhibit a microstructure consisting of α'' and β phases as shown in Figure 2.30. Figure 2.31 shows the SAED pattern images of the samples. Figure 2.29a displays the acicular α'' and Figure 2.29b shows the equiaxed β. With the addition of Mn, the acicular α'' gradually diminished. Figure 2.31c exhibits the ω and β phases in Ti-26-1Mn Figure 2.31d shows the SAED Ti-26Nb-7Mn, respectively.

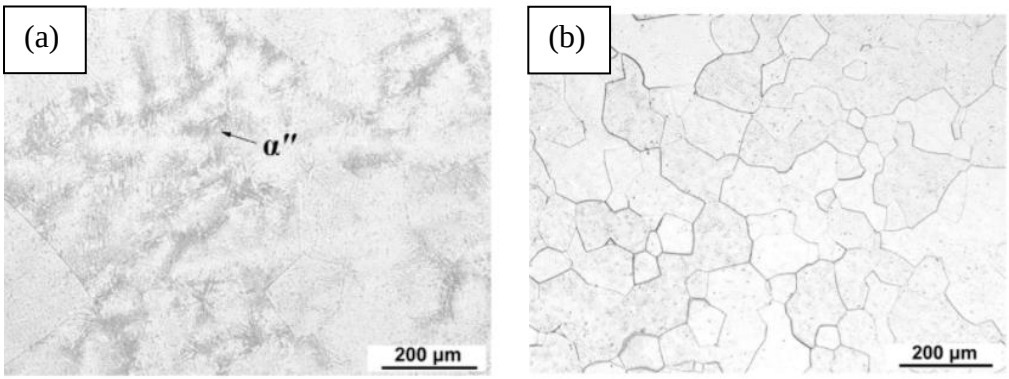

Figure 2.30 Optical micrographs of: a) Ti-26Nb and b)Ti-26Nb-3Mn, respectively [50].

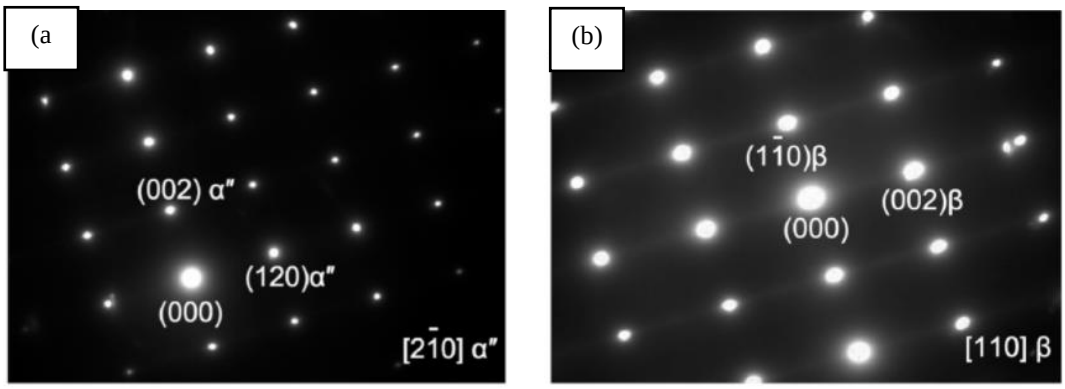

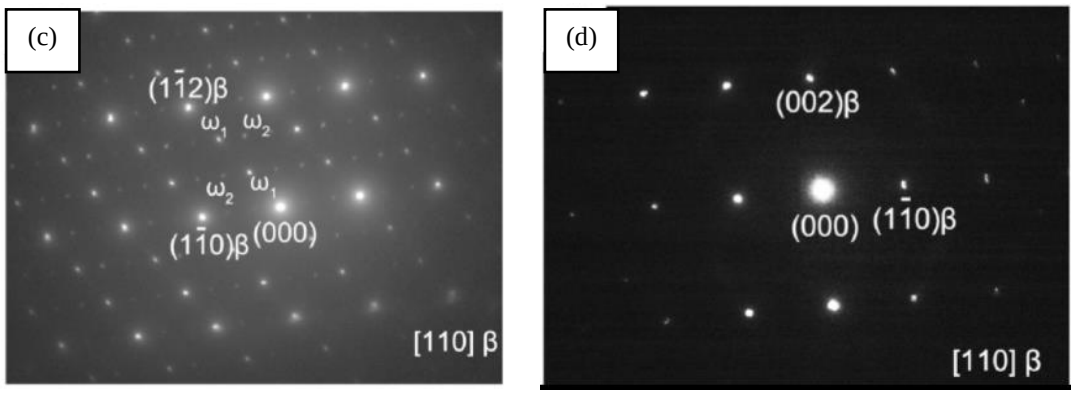

Figure 2.31 a) SAED pattern containing α'' phase in Ti-26Nb b) SAED pattern of β phase c) SAED pattern of omega(ω) phase in the β matrix in Ti-26Nb-1Mn d) β phases in Ti-26Nb-8Mn, respectively [50].

Table 2.3 shows the mechanical properties of the Ti-16Nb-xMn alloys and it is observed that the yield and ultimate tensile strength increases with addition of Mn. This is can be due to the combined effect of solid solution strengthening effect and the presence of athermal ω phase. The spike in the Young's modulus value and dip in the % elongation after the addition of 1at% Mn can be attributed to the presence of the athermal ω phase as indicated by fig 19. There is a sequential increase in the plastic strain and a decrease in the Young's modulus with increased addition of Mn.

Table 2.3 Mechanical properties of Ti-26Nb-xMn (wt%) [50]

Alloys (wt%)	**YS (MPa)**	**UTS (MPa)**	**Elongation (%)**	**Young's Modulus (GPa)**
Ti-26Nb	372	570	33	102
Ti-26Nb-1Mn	507	644	16	131
Ti-26Nb-4Mn	553	675	24	118
Ti-26Nb-6Mn	657	716	26	109
Ti-26Nb-8Mn	646	695	43	77
Ti-26Nb-10Mn	621	660	41	80

The SEM fractography of the samples as shown in Figure 2.32 illustrates the nature of failure of the samples. It is evident that Ti-16Nb consists of large dimples which is indicative of ductile fracture while 1Mn exhibits transgranular cleavage like features indicating a brittle behaviour (due to the omega phase). Ti-26Nb-4Mn and Ti-26Nb-6Mn samples are characterised by both dimples and cleavage like features however, due to the presence of more dimple regions the mode of fracture is concluded to be ductile. Finally, Ti-26Nb-8Mn and Ti-26Nb-10Mn

samples' surface completely comprises dimple like regions which is characteristic of ductile fracture [50].

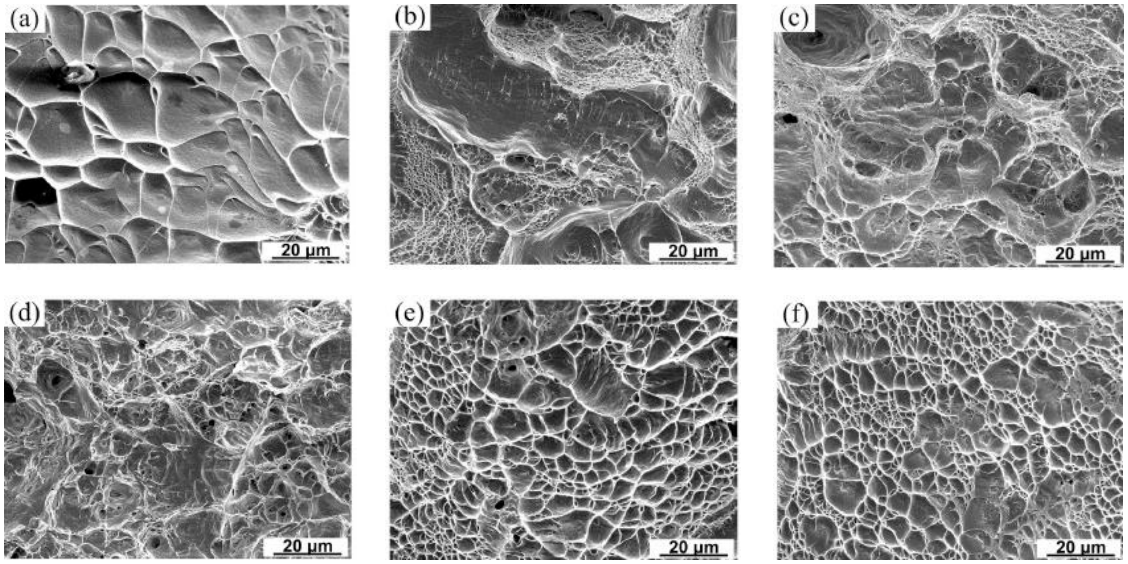

Figure 2.32 Fractographic surfaces of: a) Ti-26Nb, b) Ti-26Nb-1Mn, c) Ti-26Nb-4Mn, d) Ti-26Nb-6Mn, e) Ti-26Nb-8Mn and f) Ti-26Nb-10Mn, respectively [50].

2.2.2 Ti-Nb-Fe alloys

Ti-7Fe-xNb(x=0,1,4,6,9,11wt%) alloys were produced by Cold Crucible Levitation Melting (CCLM). XRD spectra of Ti-7Fe consists of a body centered cube and orthorhombic martensite (α'') structure as seen from Figure 2.33. After 1wt% addition of Nb, there is not much difference in the composition of the phases whereas once 4wt% or more Nb was added, the formation of the orthorhombic phase was gradually supressed. After 9wt% addition of Nb, the alloy consists of majority of β phase with minimal α martensite and finally with when 11 wt% Nb was added, the alloy showed only β phase peaks [75]. However, Hsu et al. [76] were able to detect the presence of omega phase in Ti-5Nb-xFe alloys using slow scanning speed in XRD. The alloys were produced via vacuum pressure arc melting.

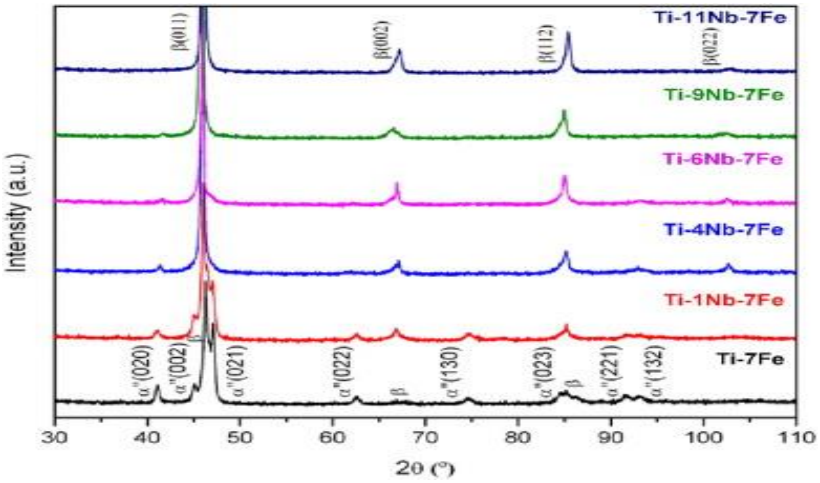

Figure 2.33 XRD spectra of Ti-7Fe-xNb [77].

Figure 2.34 shows the SEM micrograph of Ti-7Fe-xNb alloys and the images are in accordance with the diffraction spectra. The average β grain size of the alloys is measured to be 144 – 175 µm. Figure 2.35 is the representative fracture surface of Ti-5Nb-(2,3,4) Fe. It is observed that with increase in Nb content, the fracture surface seems to look smoother indicating a brittle fracture. Such behaviour can be attributed to the presence of ω phase. According to Afonso, the athermal omega phase can precipitate within the matrix leading the material to become fragile [36].

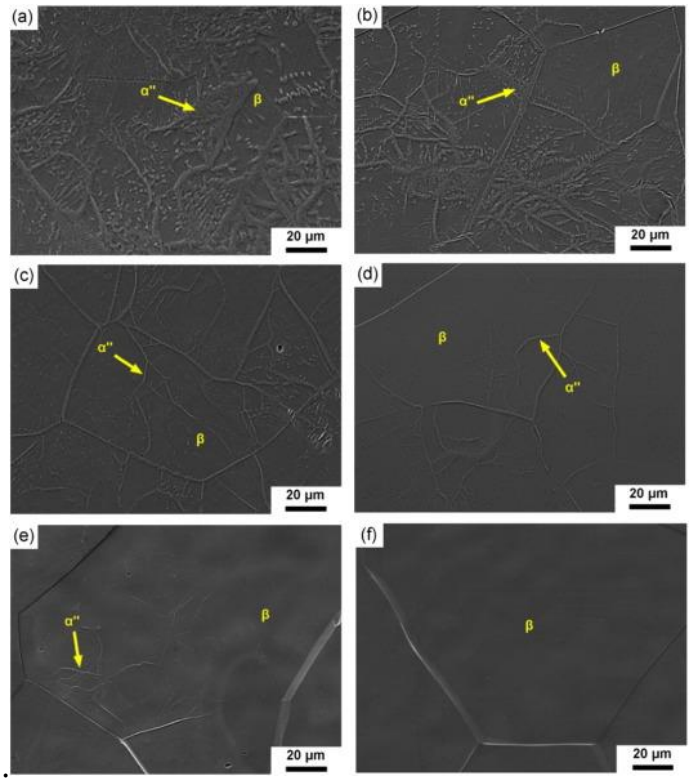

Figure 2.34 SEM micrograph of a) Ti-7Fe, b) Ti-7Fe-1Nb, c) Ti-7Fe-4Nb , d) Ti-7Fe-6Nb, e) Ti-7Fe-9Nb and f) Ti-7Fe-11Nb, respectively [77].

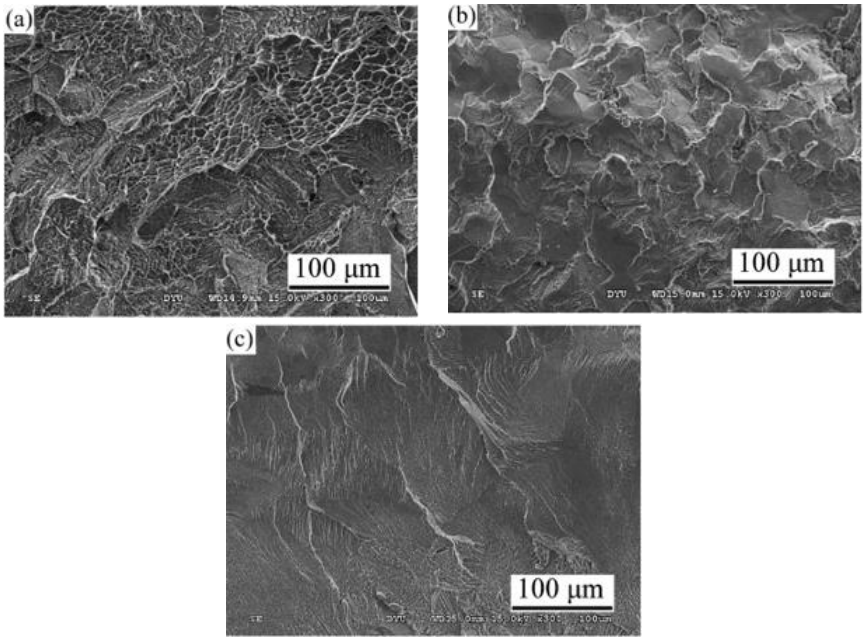

Figure 2.35 SEM fractograph of a) Ti-5Nb-2Fe, b) Ti-5Nb-3Fe and c) Ti-5Nb-4Fe, respectively [76].

It is evident that the mechanical properties are primarily governed by the microstructure and the existing phases. The mechanical properties of Ti-7Fe-xNb are summarised in table 5. It is seen that with the addition of Nb, the compressive strength, hardness and Young's modulus tend to decrease. Likewise, the compressive strain seems to increase with the addition of Nb as the β phase becomes the dominant phase. This can be attributed to the suppression of the formation of the martensitic phases due to the β stabilization as is evident from the microstructure and XRD.

Table 2.4 Mechanical Properties of Ti-7Fe-xNb alloys [77]

Alloy composition (wt.%)	**YS (MPa)**	**UCS (MPa)**	**Elongation (%)**	**Young's Modulus (GPa)**
Ti-7Fe	1847 ± 5	1990 ± 8	7.9 ± 0.2	130 ± 1
Ti-1Nb-7Fe	1785 ± 7	1972 ± 12	10.0 ± 0.9	124 ± 2
Ti-4Nb-7Fe	1539 ± 11	2093 ± 17	24.3 ± 0.3	115 ± 2
Ti-6Nb-7Fe	1144 ± 7	2014 ± 14	32.1 ± 1.7	97 ± 3
Ti-9Nb-7Fe	1010 ± 9	2007 ± 15	40.5 ± 1.9	89 ± 1
Ti-11Nb-7Fe	985 ± 8	2006 ± 14	41.5 ± 1.6	86 ± 1

Ehtemam-Haghighi et al. [78] produced Ti-11Nb-xFe (x=0.5, 3.5, 6, 9 wt%) alloys via CCLM and the XRD spectra from Figure 2.36 shows us that Ti-11Nb-0.5Fe exhibits a mixture of hexagonal closed pack structures and body centered cubic structures. However, with further addition of Nb, the β peaks gradually stabilise, suppressing the growth α-hcp while Ti-11Nb-9Fe shows only dominant β peaks.

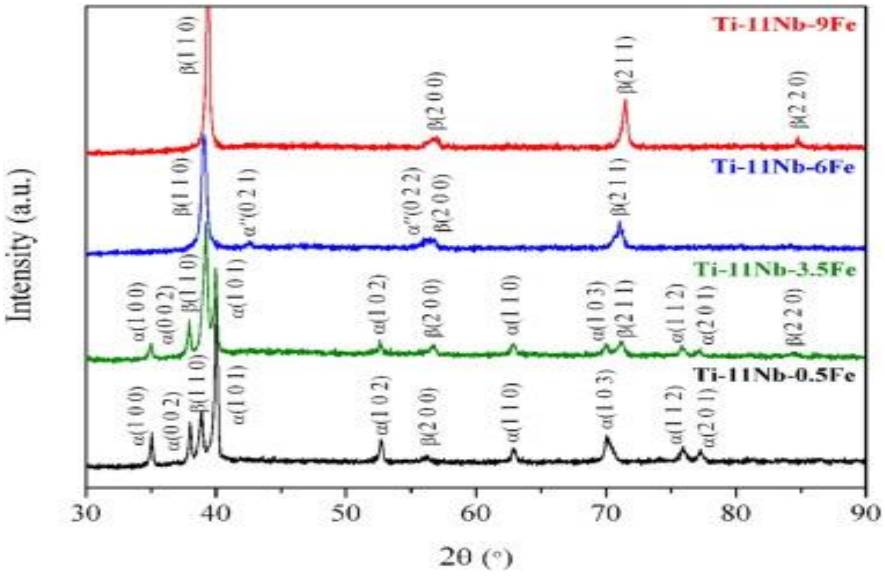

Figure 2.36 XRD spectra of Ti-11Nb-xFe [78]

The SEM micrograph (Figure 2.37**)** of the Ti-11Nb-0.5Fe alloy is characterised by an α+β Widmanstätten microstructure with refined α lamellae. With increase in the Nb content, the growth of the α phase is restricted resulting in prevalent β grains. Addition of 6% Nb results in predominant β grains with minimal martensitic α'' phases followed by equiaxed β grains at 9%Nb.

The mechanical properties of Ti-11Nb-xFe alloys are displayed in Table 2.5. It can be seen that the increase in strength due to addition of Fe is evident and gradually with the stabilization of the β phase, the elongation increases while the strength and hardness decreases along with the Young's modulus.

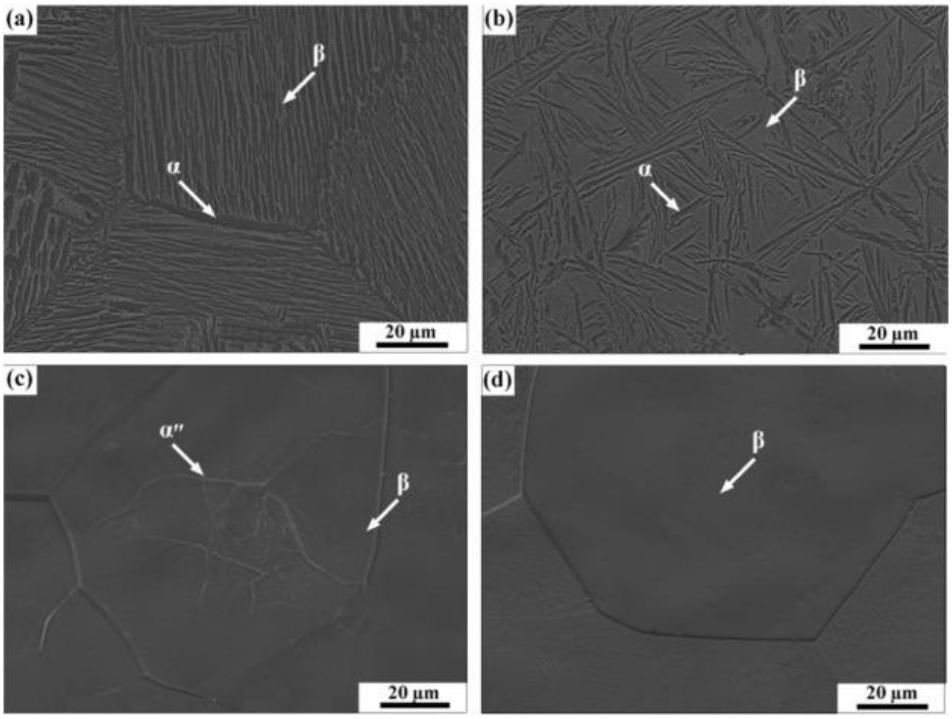

Figure 2.37 SEM micrograph of Ti-11Nb a)0.5Fe b)3.5Fe c)6Fe d)9Fe, respectively [78].

Table 2.5 Mechanical properties of Ti-11Nb-xFe alloys [78].

Alloy composition	**YS (MPa)**	**Elongation (%)**	**Hardness (HVC)**	**Young's modulus (GPa)**
Ti-11Nb-0.5Fe	796	18	278	109
Ti-11Nb-3.5Fe	932	29	303	101
Ti-11Nb-6Fe	1137	36	357	89
Ti-11Nb-9Fe	1078	38	334	82

The mechanical behaviour of the Ti-11Nb-xFe alloys can better understood with the aid of the SEM micrographs of the fracture surfaces as seen in Figure 2.38. The fractography indicate that the surfaces of Ti-11Nb-(0.5,3.5) Fe contain proportions of smooth regions as well as dimple like regions while the former is an evidence of a brittle fracture and the latter that of a ductile fracture. Hence the relatively less plastic strain is observed in 0.5Fe and 3.5Fe compared to the remaining alloys. The reason 3.5 %Fe and 6%Fe were not studied is because they never fractured.

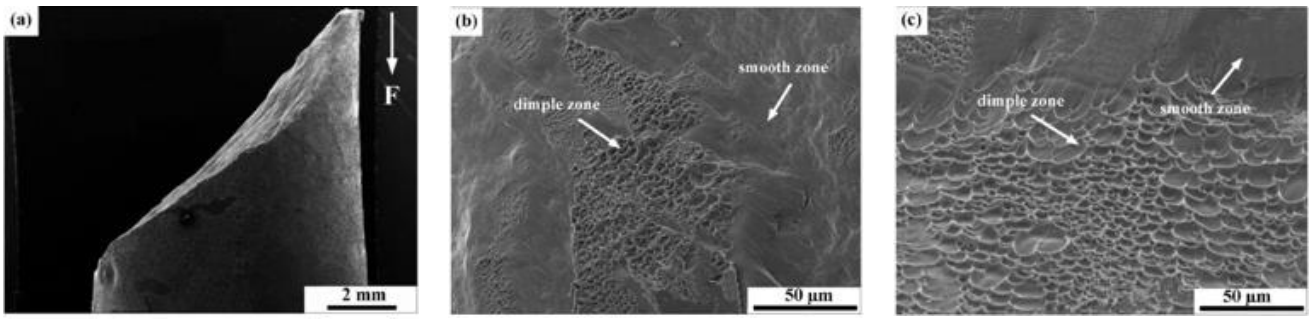

Figure 2.38 Fractographs after compressive testing: (a) macroscopic fracture morphology, (b) Ti-11Nb-0.5Fe and (c) Ti-11Nb-3.5Fe alloys, respectively [78].

The cell viability of MG-63 cells on Ti-5Nb-xFe alloys was assessed using an MTT assay. After incubating for 1 day and 4 days, it was observed that the Ti-5Nb-xFe alloys had better proliferation than C.P. Ti and Ti-6Al-4V. Figure 2.39 displays the absorbance values (number of viable cells) present after 24h and 96h on each sample.

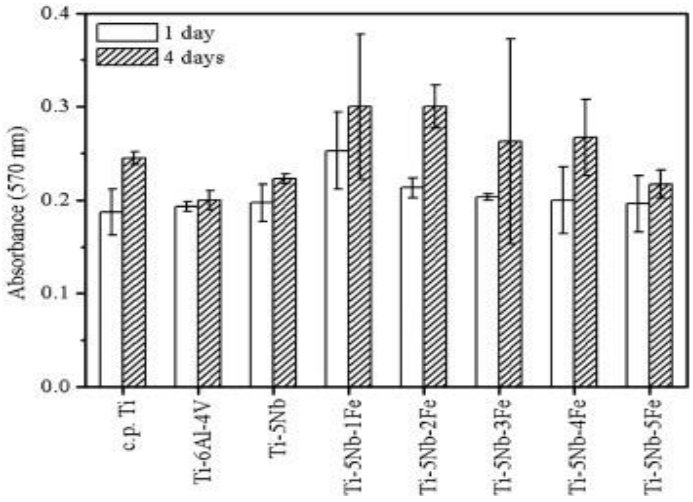

Figure 2.39 Cell viability assay after 1day and 4 days [78].

For both Ti-Nb-Mn and Ti-Nb-Fe ternary systems, it is seen that most of the research conducted is via casting. Also, the amount of Nb, Mn and Fe added as alloying elements are high. The compositions for the current project will be designed in such a way that the behaviour of the Ti-Nb-Mn and Ti-Nb-Fe alloys processed via powder metallurgy route is studied and the effect of adding alloying elements <10wt% on the microstructure and properties also is to be investigated. Further, it is observed that the formation of metastable phases is quite prominent among the alloys reviewed above. It is believed that the compositions chosen for the current project will have a minimal metastable phases/athermal phases.

Chapter Three

Motivation

Among the different classes of Ti alloys, β Ti alloys seem to be an appropriate choice for biomedical applications as their Young modulus is much closer to that of the human cortical bone in comparison with commercially pure Ti or other α+β Ti alloys. Especially since Ti-6Al-4V has been proven toxic due to release of metallic ions into the blood stream, material scientists came about with various β Ti alloys without any toxic elements such as vanadium, nickel, chromium etc., where Ti-13Nb-13Zr, Ti-15Mo, TMZF, TNTZ are considered to be the second generation of Ti based biomaterials.

Evidently, there are numerous reports that claim that Nb aids cell proliferation and has relatively less cytotoxic than Mo. But the usage of rare earth elements such as Ta reduces the purchasing power for the implant materials. Therefore, this research project is aimed at producing cost effective Ti-Nb based alloys that can potentially be used as implant materials. By adding elements like Mn or Fe, the resultant materials can be made widely accessible to the patients. Furthermore, by employing a technique such as powder metallurgy which is a solid-state near net shape manufacturing technique favours the cause of producing affordable implant materials.

Although there has been research conducted on the binary Ti-Mn, Ti-Nb and Ti-Fe systems, the number of research articles on the combination of the same is limited. Moreover, research on the development of Ti-Nb-Mn and Ti-Nb-Fe alloys via powder metallurgy is even rarer. Along with that, the existing reports pertaining to the above-mentioned systems only exploit a tiny window and a large part of is still uncharted.

Henceforth, the current thesis aims to investigate a wide range of compositions (in the Ti-Nb-Mn and Ti-Nb-Fe systems) and intend to develop α+β and metastable β alloys that could potentially be used as long-term structural implants.

3.1 Research Objectives

- Design various compositions for both the Ti-Nb-Mn and Ti-Nb-Fe systems aiming to produce α+β alloys and metastable stable β alloys based on the Molybdenum Equivalent (MoE) parameter and gaps from the previous research.

- Warm compaction of the elemental powders corresponding to the different systems and compositions.
- Choose appropriate sintering conditions in order to achieve a homogeneous microstructure with minimum porosity and prevent the formation of metastable phases.
- Perform X-ray diffraction on the alloys in order to identify the different phases and to check/confirm the presence of metastable phases.
- Investigate the microstructural features using optical and electron microscopy.
- Characterise the alloys for physical (density and porosity) and mechanical properties (yield and ultimate tensile strength, failure strain, Young's modulus and hardness) and check its correlation with the microstructural features.
- Compare the properties of the Ti-Nb-Mn and Ti-Nb-Fe alloys with the already existing alloys based on the literature values.

Chapter Four

Materials and Methods

This chapter presents the raw materials, design criteria, experimental methods and parameters utilised to produce Ti-Nb-Mn and Ti-Nb-Fe alloys.

4.1 Raw materials

The characteristics of the elemental titanium (Ti), niobium (Nb), manganese (Mn) and iron (Fe) powders are illustrated in Table 4.1. Figure 4.1 displays the SEM micrograph of the Ti, Nb, Mn and Fe powders, respectively. It can be seen that each elemental powder has different size and morphology. According to German [2], the mean particle size and the morphology of the powders affects the compressibility and therefore the green density of the samples. For instance, the difference in the size of Mn powders and that of Ti and Nb powders facilitate better mechanical interlocking. However, spherical powders have poor compressibility due to its shape factor. Hence, Fe powders were chosen to have small particle size. Fine powders tend to sinter better due to high surface energy and short diffusion path.

Table 4.1 Powder characteristics

Materials	Particle size	Morphology	Purity (%)	Supplier
Titanium	200 mesh (<75µm)	Irregular	99.4	Goodfellow Cambridge Ltd, UK
Niobium	325 mesh (<45µm)	Angular	99.8	Alfa Aesar (USA)
Manganese	325 mesh (63 µm)	Irregular	99.0	Sigma Aldrich, USA
Iron	1250mesh (<10 µm)	Spherical	99.0	Goodfellow Cambridge Ltd, UK

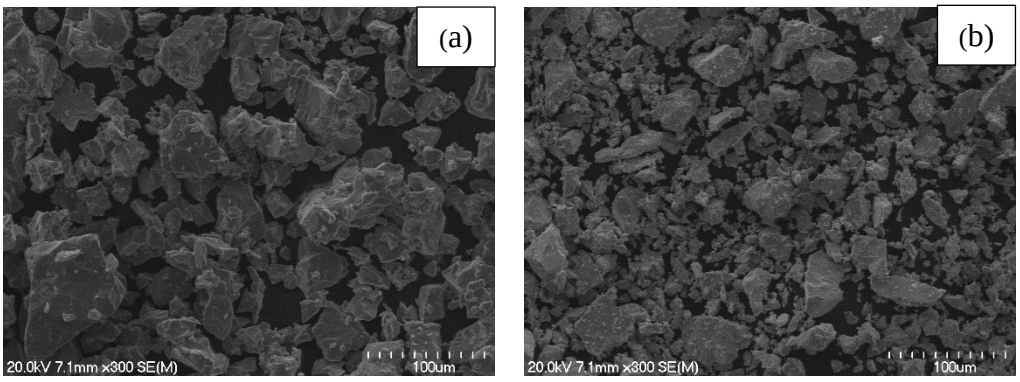

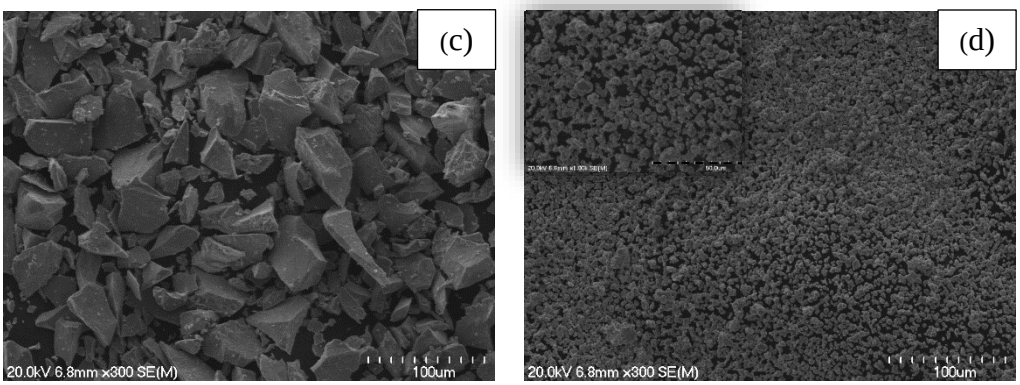

Figure 4.1 SEM micrograph of elemental powders a) Ti, b) Nb, c) Mn and (d) Fe

4.2 Design of the alloys

The Ti-Nb-Mn and Ti-Nb-Fe alloys were designed based on the Molybdenum equivalent (MoE) parameter to obtain a range of α+β and metastable β alloys. Brief explanation of MoE parameter is provided in Metallurgy of Ti (page 7). A simplified version of equations (1-1) and (1-2), based on the choice of alloying elements is mentioned in equation (4-1) [16]and equation (4-2) [17].

$$\mathrm{MoE} = (0.28 \times [\mathrm{Nb}]\mathrm{wt}\%) + (1.54 \times [\mathrm{Mn}]\ \mathrm{wt}\%) + (2.9 \times [\mathrm{Fe}]\ \mathrm{wt}\%) \quad (4\text{-}1)$$

$$\mathrm{MoE} = (0.28 \times [\mathrm{Nb}]\mathrm{wt}\%) + (2.26 \times [\mathrm{Mn}]\ \mathrm{wt}\%) + (1.93 \times [\mathrm{Fe}]\ \mathrm{wt}\%) \quad (4\text{-}2)$$

Theoretically, 10-15 wt% of Molybdenum is sufficient to produce a fully stable β Ti alloy [79]. However, Cotton et al. [80] classifies Ti alloys into β matrix α+β alloys (MoE ≤ 5), near β (5≤ MoE ≤10) and metastable alloys ranges between (10≤ MoE ≤30). Yet the formation of different phases is dependent on various parameters such as processing technique and the compositions. Taking that into account, the Ti-Nb-Mn and Ti-Nb-Fe alloys were designed to have MoE values ranging between 6-20. Table 4.2, displays the chosen Ti-Nb-Mn and Ti-Nb-Fe alloys and their MoE parameters (calculated from both the equations). In addition to the MoE parameter, preventing the formation of intermetallic compounds and the gaps in previous research were the criteria on which these alloys were designed.

Table 4.2 List of compositions for Ti-Nb-Mn and Ti-Nb-Fe alloys and their MoE values.

System	Alloys	Ti (wt%)	Nb (wt%)	Mn (wt%)	MoE (4-1)	MoE (4-2)
	C.P. Ti	100	0	0	0	0
Ti-5Mn	Ti-1Nb-5Mn	94	1	5	8.0	11.6
	Ti-5Nb-5Mn	90	5	5	9.1	12.7
Ti-8Mn	Ti-2Nb-8Mn	90	2	8	12.9	14.4
	Ti-6Nb-8Mn	86	6	8	14.0	15.2
Ti-6Mn	Ti-3Nb-6Mn	91	3	6	10.1	18.6
	Ti-6Nb-6Mn	88	6	6	11.0	19.8
Ti-4Nb	Ti-4Nb-7Mn	89	4	7	11.9	16.9
	Ti-4Nb-9Mn	87	4	9	15	21.5
Ti-2Nb	Ti-2Nb-3Fe	95	2	3	9.3	6.4
	Ti-2Nb-5Fe	93	2	5	15.1	10.2
	Ti-2Nb-6Fe	92	2	6	18.0	12.2
Ti-5Nb	Ti-5Nb-3Fe	92	5	3	10.1	7.2
	Ti-5Nb-4Fe	91	5	4	13.0	9.2
Ti-6Nb	Ti-6Nb-5Fe	89	6	5	16.2	11.4
	Ti-6Nb-6Fe	88	6	6	19.1	13.3
Ti-8Nb	Ti-8Nb-2Fe	90	8	2	8.1	6.2
	Ti-8Nb-4Fe	88	8	4	13.9	10.0
Ti-9Nb	Ti-9Nb-5Fe	86	9	5	17.1	12.2
	Ti-9Nb-6Fe	85	9	6	20.0	14.2
Ti-4Fe	Ti-3Nb-4Fe	93	3	4	12.5	8.6
	Ti-5Nb-4Fe	91	5	4	13.0	9.2
	Ti-8Nb-4Fe	88	8	4	13.9	10.0

From Table 4.2, it is noticed that the MoE values of Ti-Nb-Mn alloys calculated by equation (4-1) falls within the classification of near β and metastable β alloys. Whereas the MoE values of Ti-Nb-Fe alloys calculated by equation (4-2) falls within the range of α+β, near β and metastable β alloys.

The theoretical density (ρ_{th}) of the alloys was calculated using the rule of mixture. The formula for the calculation of theoretical density is shown in equation (4-3).

$$\rho_{alloy} = (\rho_{element\ 1} \text{ x wt\% [element 1]}) + (\rho_{element\ 2} \text{ x wt\% [element 2]}) + (\rho_{element\ 3} \text{ x wt\% [element 3]}) \quad (4\text{-}3)$$

According to the rule of mixtures, the theoretical density of the alloys is the product of the theoretical density of the individual elements, $\rho_{(Ti,Nb,Mn,Fe)}$ and the corresponding wt % (in grams). Density values were calculated in g/cm^3.

4.3 Processing route

The Ti-Nb-Mn and Ti-Nb-Fe alloys were produced via the Blended Elemental (BE) method through powder metallurgy route. These alloys were initially prepared according to the compositions mentioned in **Table 4.2.** The powders are then blended together in order to facilitate uniform distribution of the particles of different density. The blended powders are warm pressed (at 250^{o}C) and vacuum sintered to improve strength and achieve minimum porosity. These samples are then subjected to various characterisation techniques such as XRD, metallographic analysis, uniaxial tensile stress and Rockwell hardness. Detailed explanation regarding the process is explained in **1.5.2**

4.3.1 Powder mixing

The samples containing elemental powders with the proportion of alloying elements presented in **Table 4.2** were allowed to homogenise in the V-mixer at a frequency of 45 Hz for about 30 minutes at room temperature. In order to prevent contamination, the V-mixer was cleaned after every cycle. The mixing of elemental powders is expected to result in a uniform distribution of the powder particles as the density and characteristics of the individual powders are different.

4.3.2 Warm compaction

The homogeneous mixture of the powders was then uniaxially pressed using a 100-ton vertical hydraulic press (HRB-1010) at 600MPa at a temperature of 200^{o}C. Both the die and plunger were coated with graphite based colloidal solution. This acts as a lubrication allowing free movement between sample and die and also reduced die wall friction [2]. The warm pressed compacts are called green bodies or green compacts. The corresponding density is the green density. Compaction of powders at temperatures higher than room temperatures facilitate to increase the green density of the compacts by lowering the yield strength thereby causing increased plastic deformation. Detailed explanation of warm compaction and its advantages is discussed in details in 1.5.

4.3.3 Vacuum sintering

The green compacts are a result of mechanical interlocking of the elemental powders due to the load applied during warm compaction. As a result, the green bodies contain large fraction of porosity. Therefore, in order to minimise porosity and improve the strength, sintering is performed. The green bodies were heated up to 1300^{o}C in a vacuum furnace (ZSJ – 20 x 20 x 30) and were isothermally held for 2 hours. The vacuum was set to 10^{-3} Pa and the heating and cooling rates were set to 10^{o}C/min.

4.3.4 Characterisation

The theoretical density of the green compacts were calculated using the equation 4-3 and equation (4-4). The mass (m) of the samples (in grams) was measured using an analytical scale. The volume was calculated using equation (4-4). 'd' and 'h' are the diameter and height of the green compact respectively (measured in cm). The diameter and height of the samples was measured using a Vernier calliper. Three readings were measured and the mean was subsequently calculated.

$$\rho_{green} = \frac{Mass\ (g)}{Volume\ (cm^3)} \tag{4-3}$$

$$Volume, V = \pi \times \frac{(d^2)}{4} \times h \tag{4-4}$$

The sintered density, $\rho_{sintered}$ was measured using Archimedes' principle of liquid displacement according to ASTM B962 [81]. The sintered samples were weighed in air followed by in distilled water. Three readings were taken and the mean mass was calculated. W_{air} and W_{water} represents the mass of the sample in air and water respectively whereas ρ_{water} is the density of the distilled water used. (0.997 g/cm^3) [82]

$$Sintered\ density, \rho_{sintered} = \frac{W_{air}}{(W_{air} - W_{water})} \times \rho_{water} \tag{4-5}$$

The relative density is calculated from equation (4-6). The $\rho_{sintered}$ value obtained from equation (4-5) is used to determine the relative density.

$$Relative\ sintered\ density, \rho_{rel.sintered} = {\rho_{sintered}}/{\rho_{theoretical}} \times 100\% \quad (4\text{-}6)$$

Using the green and sintered density, the densification (Ψ) was calculated. Densification is defined as the ratio of actual change in density during sintering to the expected change in density [2]. In other words, it is a measure of effectiveness of densification. Equation (4-7) represents the formula to calculate Ψ.

$$\Psi = \frac{(\rho_S - \rho_G)}{(1 - \rho_G)} \times 100 \quad (4\text{-}7)$$

Using the % densification values, the % decrease in densification was calculated using equation (4-8).

$$\%\ Decrease\ in\ densification = \frac{(Starting\ value - Final\ value)}{Starting\ value} \times 100 \quad (4\text{-}8)$$

The sintered samples were cut into various samples in order to be characterised. The samples were cut using an Electrical Discharge Machining (EDM).

XRD was performed using a Philips X'pert diffractometer with Cu Kα radiation of wavelength of 1.54 Å. The operating conditions were 45 kV and 40 mA. For XRD, the samples were cut into thin plates with the dimension 20 x 10 x 2 mm^3. For metallographic characterisation, an Olympus BX60 optical microscope equipped with Nikon digital camera (DS-SMc) was used. A field emission type Hitachi S4700 Scanning Electron Microscope was used to analyse the chemical homogeneity, microstructural features and porosity of the samples. The accelerating voltage was kept at 20 keV. Tiny samples of dimension 4 x 4 x 20 mm^3 were cut and ground using #320, #600, #1000 grit silicon carbide grinding papers prior to using a Struers Tegramin-25 semi-automatic polisher. Non-drying colloidal silica suspension was used as a polishing compound. In order to perform microstructural characterisation, the samples were etched using Kroll's reagent (4% Hydrofluoric acid, 5% Nitric acid and 91% distilled water). The etchant was allowed to stay for 10-20 seconds after which they were washed off using isopropanol.

Tensile testing was performed using an Instron 33R 4204 universal testing machine. The cross-head speed was set to 0.1 mm/min. An INSTRON static axial strain gauge extensometer with a gauge length of 10 mm was used to obtain the elongation values. The samples were cut into dog-bone shaped tensile samples with a gauge length of 20 mm.

Hardness test was performed using a Rockwell Hardness tester (LCR-500). Rockwell scale ‘A’ was used. The indentations were made using a diamond indenter as per ASTM E-18 [83] on the gripping section of the tensile samples (post fracture). Six readings were noted and the mean hardness was calculated.

Chapter Five

Results & Discussion

5.1 Ti-Nb-Mn system

5.1.1 Density and porosity measurements

5.1.1.1 Ti-5Mn and Ti-6Mn systems

Table 5.1 displays the physical properties of C.P. Ti, Ti-1Nb-5Mn, Ti-5Nb-5Mn, Ti-3Nb-6Mn and Ti-6Nb-6Mn corresponding to the Ti-5Mn and Ti-6Mn systems, respectively. The density mentioned in Table 5,1 and discussed further denote the relative density (%). C.P. Ti has the highest green and sintered density and correspondingly highest densification. The green density of the individual alloys belonging to the Ti-5Mn and Ti-6Mn systems are similar. Among the other alloys, Ti-5Nb-5Mn has the lowest densification and Ti-1Nb-5Mn has the highest densification. Between the Ti-5Mn and Ti-6Mn systems, the decrease in densification between the alloys from the Ti-5Mn system is the highest.

Table 5.1 Physical properties of C.P. Ti, Ti-1Nb-5Mn, Ti-5Nb-5Mn, Ti-3Nb-6Mn and Ti-6Nb-6Mn corresponding to the Ti-5Mn and Ti-6Mn systems, respectively.

System	Material	ρ_{green} (%)	$\rho_{sintered}$ (%)	Porosity (%)	Densification Ψ (%)	Decrease in densification (%)
	C.P. Ti	96.2	99.0 ± 0.1	1.0	73	-
Ti-5Mn	Ti-1Nb-5Mn	94.1	97.9 ± 0.6	2.1	65	32.3
	Ti-5Nb-5Mn	93.8	96.5 ± 0.1	3.5	44	
Ti-6Mn	Ti-3Nb-6Mn	91.9	96.8 ± 0.6	3.2	60	20.2
	Ti-6Nb-6Mn	91.9	95.8 ± 0.6	4.2	48	

Figure 5.1 displays the relationship between densification and porosity for Ti-1Nb-5Mn, Ti-5Nb-5Mn, Ti-3Nb-6Mn and Ti-6Nb-6Mn corresponding to the Ti-5Mn and Ti-6Mn systems, respectively. Densification is a measure of effectiveness of sintering and is seen that it is inversely related to porosity. It is notable that the densification gradually decreases with the addition of Nb.

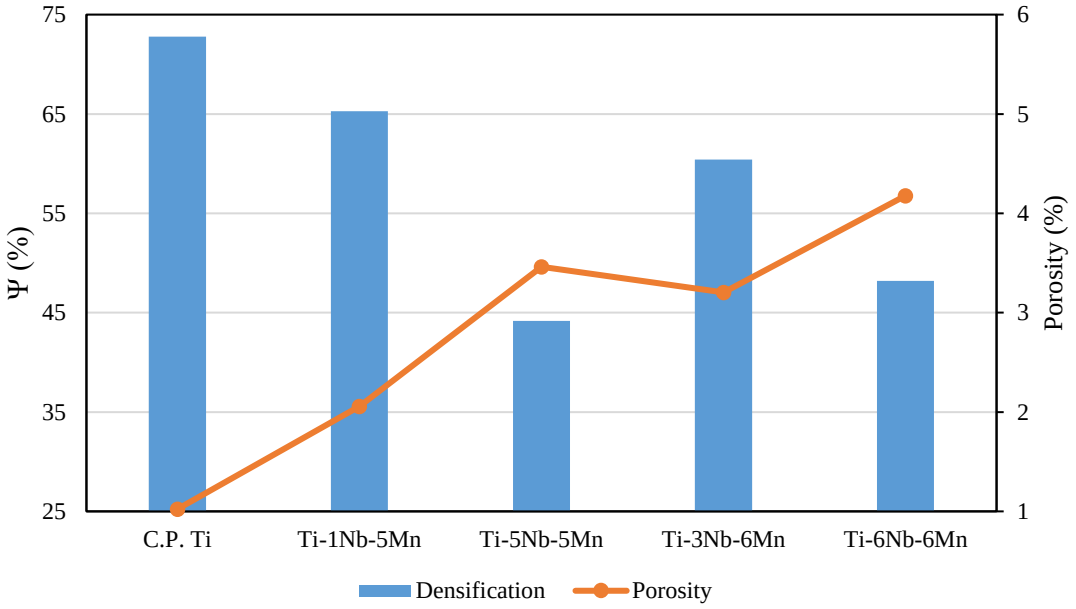

Figure 5.1 Relationship between densification and porosity for C.P. Ti, Ti-1Nb-5Mn, Ti-5Nb-5Mn, Ti-3Nb-6Mn and Ti-6Nb-6Mn corresponding to the Ti-5Mn and Ti-6Mn systems, respectively.

The reason for the negligible change in the green density can be attributed to the nature of the elemental powders such as average particle size and morphology (as explained in Chapter 4.1). Further, the decrease in the densification is the maximum in the Ti-5Mn system. This is attributed to the amount of Nb and the same is due to the poor diffusivity of the element [42].

5.1.1.2 Ti-8Mn and Ti-4Nb systems

Table 5.2 shows the physical properties of C.P. Ti, Ti-2Nb-8Mn, Ti-6Nb-8Mn, Ti-4Nb-7Mn and Ti-4Nb-9Mn corresponding to the Ti-8Mn and Ti-4Nb systems, respectively. C.P. Ti has the highest green and sintered density and correspondingly higher densification. The green density of the alloys from the Ti-8Mn and Ti-4Nb have a difference of approximately 1.5%. The decrease in densification for the Ti-4Nb system is the relatively less when compared to that of Ti-8Mn system.

Table 5.2 Physical properties of C.P. Ti, Ti-2Nb-8Mn, Ti-6Nb-8Mn, Ti-4Nb-7Mn and Ti-4Nb-9Mn corresponding to the Ti-8Mn and Ti-4Nb systems, respectively.

Sample	Material	ρ_{green} (%)	$\rho_{sintered}$ (%)	Porosity (%)	Densification Ψ (%)	Decrease in Densification (%)
	C.P. Ti	96.2	99.0 ± 0.1	1.0	72.8	-
Ti-8Mn	Ti-2Nb-8Mn	91.6	97.2 ± 0.4	2.8	66.7	25.8
	Ti-6Nb-8Mn	90.3	95.1 ± 0.3	4.9	49.5	
Ti-4Nb	Ti-4Nb-7Mn	91.0	96.1 ± 0.7	3.9	56.6	16.2
	Ti-4Nb-9Mn	92.7	96.2 ± 0.2	3.8	47.4	

Figure 5.2 displays the relationship between densification and porosity for the alloys from the Ti-8Mn and Ti-4Nb systems. In the Ti-8Mn system, it is seen that with the increase in Nb content the densification decreases and correspondingly the porosity increases. The porosity remains the same for the Ti-4Nb systems, despite the increase in Mn content.

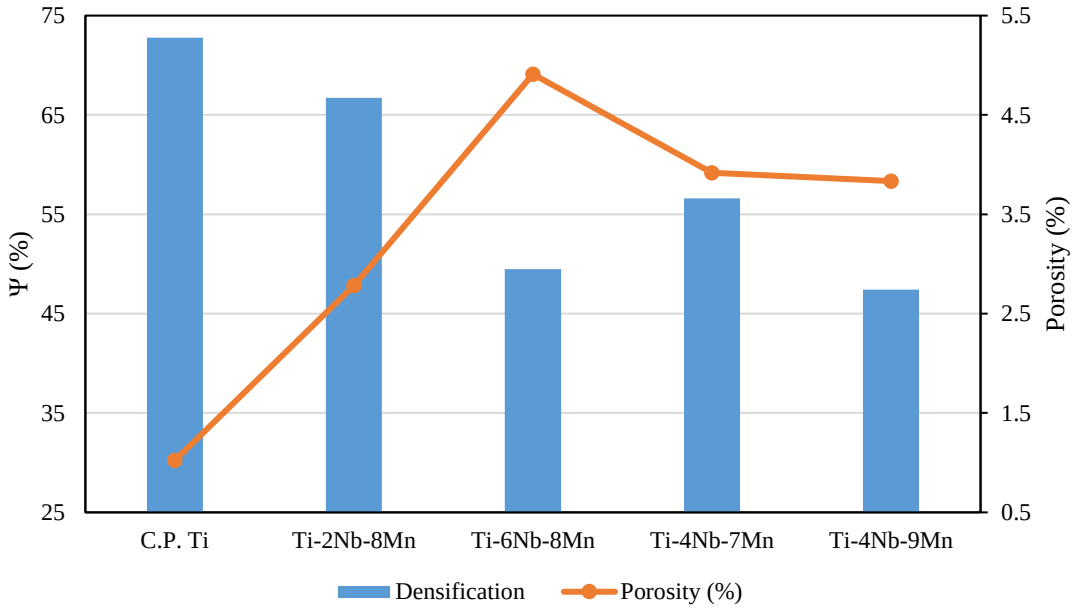

Figure 5.2 Relationship between densification and porosity of C.P. Ti, Ti-2Nb-8Mn, Ti-6Nb-8Mn, Ti-4Nb-7Mn and Ti-4Nb-9Mn corresponding to the Ti-8Mn and Ti-4Nb systems, respectively.

It is seen that increase in Nb content causes a reduction in the densification values which in turn affects the sintered density. Yilmaz et al[43]reported an increase in porosity due to the addition of Nb in Ti-xNb alloys produced by injection moulding. This behaviour is due to the poor diffusivity of Nb in Ti. However, Mn has very high diffusivity in Ti and as a result, there is little to no change in the sintered density despite the differences in green density of Ti-4Nb-7Mn and Ti-4Nb-9Mn.

In general, for the Ti-Nb-Mn alloys, the green density ranges between 90.3% and 94.1% for Ti-6Nb-8Mn and Ti-1Nb-5Mn, respectively. Correspondingly, the same alloys possess the lowest and highest sintered density of 95.1% and 97%. Among the various systems of Ti-Nb-Mn, the change in densification is the least for Ti-4Nb and is highest for the Ti-5Mn system. Hence, it is concluded that addition of Nb causes a reduction in the sintered density. This is attributed to the poor diffusivity of Nb powders.

5.1.2 Phase and microstructural analysis

5.1.2.1 Ti-5Mn and Ti-6Mn systems

Figure 5.3 displays the X-ray diffraction spectra of C.P. Ti, Ti-1Nb-5Mn, Ti-5Nb-5Mn, Ti-3Nb-6Mn and Ti-6Nb-6Mn corresponding to the Ti-5Mn and Ti-6Mn systems, respectively. It is seen that C.P. Ti exhibits only α peaks along the (1 0 0), (0 0 2), (1 0 1), (1 0 2), (1 1 0), (1 0 3), (1 1 2), (2 0 1) and (2 0 2) planes. For Ti-1Nb-5Mn and Ti-5Nb-5Mn samples, addition of Nb causes the rise of the β peak at 39°. The relative intensity of the α peaks decreases with the increase in Nb as seen in Ti-5Nb-5Mn. A similar trend of diminishing α peaks is observed in the Ti-3Nb-6Mn sample. In addition, the 57° β peak corresponding to the (2 0 0) plane gradually increases with the addition of β stabilisers (Nb and Mn). Chen et al. [50] also reports the increase in the 57° peak with the addition of β stabilisers. Among the samples from the Ti-5Mn and Ti-6Mn systems, it is evident that Ti-6Nb-6Mn exhibits the highest relative intensity of β peaks with minimum α peaks.

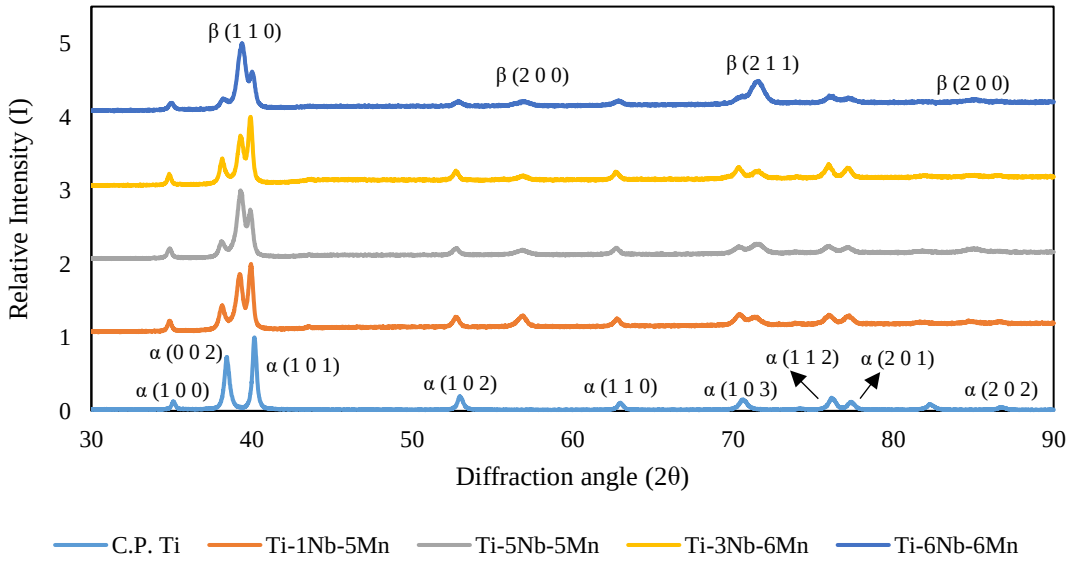

Figure 5.3 XRD spectra of C.P. Ti, Ti-1Nb-5Mn, Ti-5Nb-5Mn, Ti-3Nb-6Mn and Ti-6Nb-6Mn corresponding to the Ti-5Mn and Ti-6Mn systems, respectively.

Basically, C.P. Ti consists of only α peaks and with the addition of Nb and Mn, the α phase is gradually suppressed due to the stabilisation of the β phase. No unidentified peaks were observed which is suggestive of complete homogenisation of the powders.

Figure 5.4 represents the optical and SEM micrographs of the alloys corresponding to the Ti-5Mn and Ti-6Mn systems. Figure 5.4 (a, b) are representative micrographs of Ti-1Nb-5Mn and is characterised by α+β lamellae. The pores are predominantly spherical and closed. Closed spherical pores is indicative of the sintering reaching the final stage which occurs above 96% of relative sintered density (as indicated in Table 5.1) [2]. The micrograph of Ti-5Nb-5Mn as seen in Figure 5.4(c, d) show refinement of the α+β lamellae due to increase in the Nb content. The alloys exhibit Widmänstatten microstructure which is typical for an α+β alloy. The size of the pores in Ti-5Nb-5Mn are relatively larger when compared to Ti-1Nb-5Mn. Most pores are spherical with a few being elongated. The majority of the pores can be identified along the grain boundaries. It can be seen from Figure. 5.4 (g-j) that there is further refinement of the lamellae indicating the increase in the proportion of β phase in both Ti-3Nb-6Mn and Ti-6Nb-6Mn. The alloys exhibit a lamellar microstructure with the thickness and the proportion of α+β lamellae decreasing with the increase in Nb content. Although Ti-6Nb-6Mn exhibits a basket-weave microstructure (Widmänstatten structures) the proportion of α+β lamellae have significantly dropped and the interlamellar spacing has decreased further. Additionally, the pores in both the alloys are mostly elongated and is reflective on the sintered density values mentioned in Table 5.1.

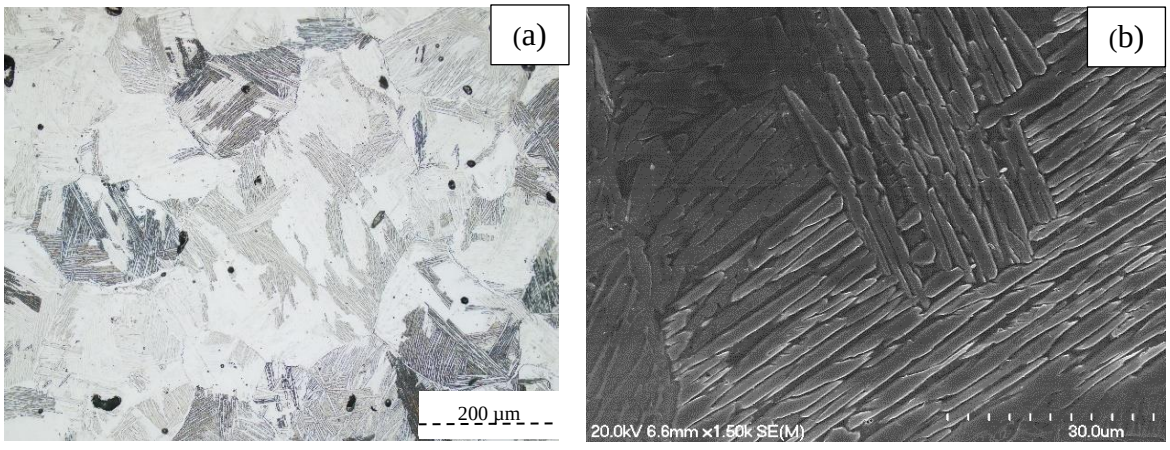

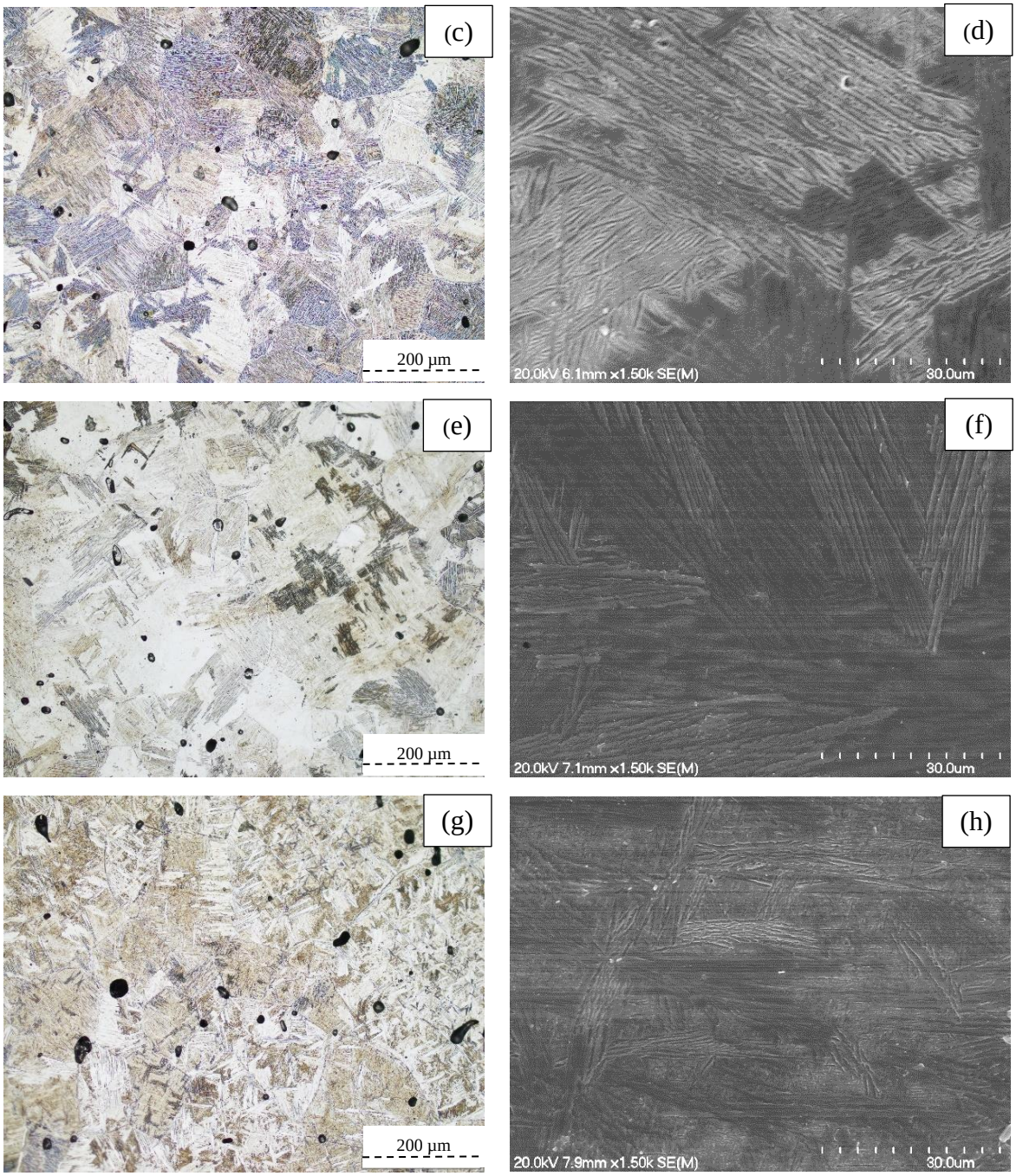

Figure 5.4 Optical and SEM micrograph of (a, b) Ti-1Nb-5Mn, (c, d) Ti-5Nb-5Mn, (a, b) Ti-3Nb-6Mn, (a, b) Ti-6Nb-6Mn corresponding to the Ti-5Mn and Ti-6Mn systems, respectively.

While all the alloys from the Ti-5Mn and Ti-6Mn systems exhibit a typical Widmänstatten microstructure, the thickness of the lamellae and the interlamellar spacing tends to vary with different compositions. All the pores are closed and spherical with a few elongated pores mostly found along the grain boundaries. This agrees with the sintered density values mentioned in Table 5.1 i.e. as the sintered density reaches 96% all pores tend to be closed and spherical. However, it is worth mentioning that a few alloys did have elongated pores localised near the grain boundaries. Furthermore, the XRD spectra of Ti-5Mn and Ti-6Mn systems as

shown in Figure 5.3 is concordant with the micrographs where the relative intensities of the β peaks are gradually increasing.

The XRD spectra of Ti-1Nb-5Mn, Ti-5Nb-5Mn and Ti-3Nb-6Mn consists of β peaks with varying relative intensities based on the amount of Nb and Mn. Correspondingly, the micrographs are also characterised by Widmanstätten microstructures which is typical for an α+β alloy. However, Ti-6Nb-6Mn shows a dominant β peaks amidst the presence of other α peaks while the micrographs show very fine overlapping α+β lamellae. Due to this ambiguity, Ti-6Nb-6Mn is categorised as near β alloy which lies in between α+β and metastable β alloys [80].

5.1.2.2 Ti-8Mn and Ti-4Nb systems

Figure 5.5 displays the XRD spectra of C.P. Ti, Ti-2Nb-8Mn, Ti-6Nb-8Mn, Ti-4Nb-7Mn and Ti-4Nb-9Mn corresponding to the Ti-8Mn and Ti-4Nb systems, respectively. C.P. Ti exhibits only α peaks. It can be seen that all four alloys primarily display dominant peaks corresponding to the β phase especially in comparison with the Ti-5Mn and Ti-6Mn systems. A significant rise in the relative intensity of the β peak at 39^{o} corresponding to (1 1 0) plane can be observed among all the samples. As reported by Ehteman-Haghighi et al. [70], the β peak corresponding to the (2 1 1) plane is seen to have risen the highest in Ti-4Nb-9Mn. Additionally, Ti-4Nb-9Mn exhibits only β peaks along the (1 1 2), (2 0 0) and (2 1 1) planes with almost no α peaks in the spectrum. The tiny peak seen around 43^{o} in Ti-4Nb-9Mn is identified to be an orthorhombic α'' phase. Chen et al. [50] reported that the XRD spectra of Ti-25Nb and Ti-26Nb-1.3Mn produced by CCLM shows a tiny peak at 43^{o} corresponding to an orthorhombic α'' phase corresponding to the (0 2 1) plane. The lattice parameters of the orthorhombic α'' phase in the Ti-26Nb alloy were found to be a = 31.7 Å, b = 48.5 Å, and c = 4.652 Å. Similarly, Karre et al.[84] also reported α'' in Ti-25Nb isochronically sintered at 1300 ^{o}C and held for 60 and 180 min. It is worth mentioning that Ti-25Nb sintered with a holding time of 20, 40 and 120 min did not show any peaks for the orthorhombic phase. It is worth mentioning that with the addition of β stabilisers the α'' gradually diminish.

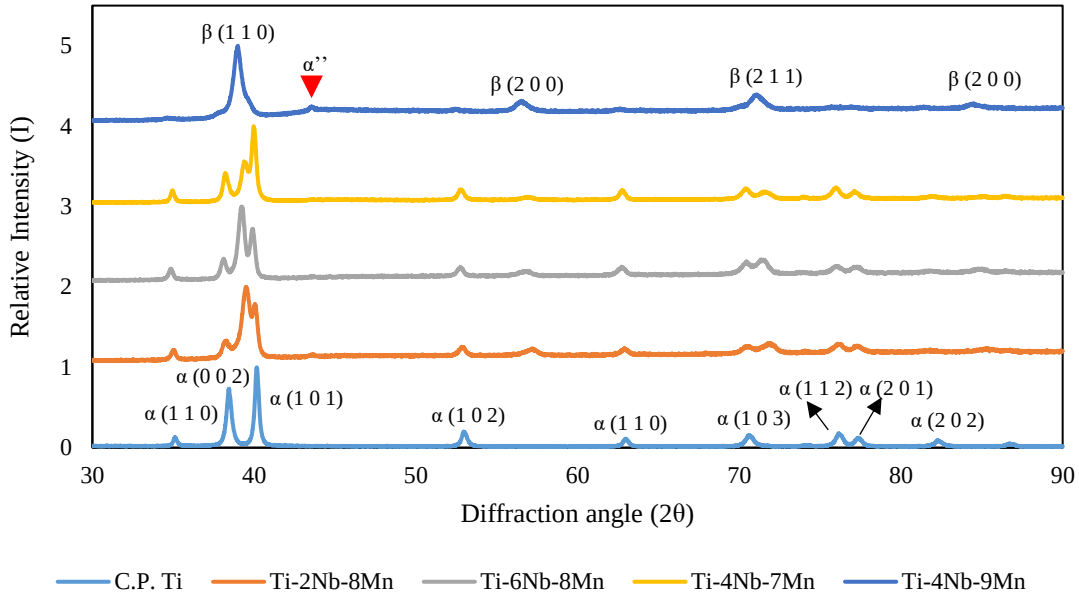

Figure 5.5 XRD spectra of C.P. Ti, Ti-2Nb-8Mn, Ti-6Nb-8Mn, Ti-4Nb-7Mn and Ti-4Nb-9Mn corresponding to the Ti-8Mn and Ti-4Nb systems, respectively.

From the XRD spectra of the alloys corresponding to the Ti-8Mn and Ti-4Nb systems as seen in Figure 5.5, it is inferred that all the alloys display prominent peaks corresponding to the β phase and Ti-4Nb-9Mn has the highest relative intensity of β peaks in addition to a tiny α'' phase.

Figure 5.6 represents the optical and SEM micrographs of Ti-2Nb-8Mn, Ti-6Nb-8Mn, Ti-4Nb-7Mn and Ti-4Nb-9Mn corresponding to the Ti-8Mn and Ti-4Nb systems, respectively. It can be seen that both Ti-2Nb-8Mn and Ti-6Nb-8Mn are characterised by equiaxed β grains and fine acicular α originating from the grain boundaries. However, the proportion of the α lamellae in the Ti-6Nb-8Mn is relatively less than that of Ti-2Nb-8Mn. Ti-2Nb-8Mn is characterised by closed spherical pores while Ti-6Nb-8Mn is characterised primarily by elongated pores segregated along the grain boundaries. Figure 5.6 (e-h) show the representative micrographs of Ti-4Nb-7Mn and Ti-4Nb-9Mn, respectively. Both alloys are characterised mainly by spherical pores with a few elongated pores especially along the grain boundaries. Ti-4Nb-7Mn microstructure consists of acicular α lamellae originating from the grain boundaries and minor proportion of Widmänstatten structures with fine α+β lamellae. Similar to Ti-6Nb-8Mn system, Ti-4Nb-9Mn alloy is characterised by equiaxed β grains and acicular α lamellae.

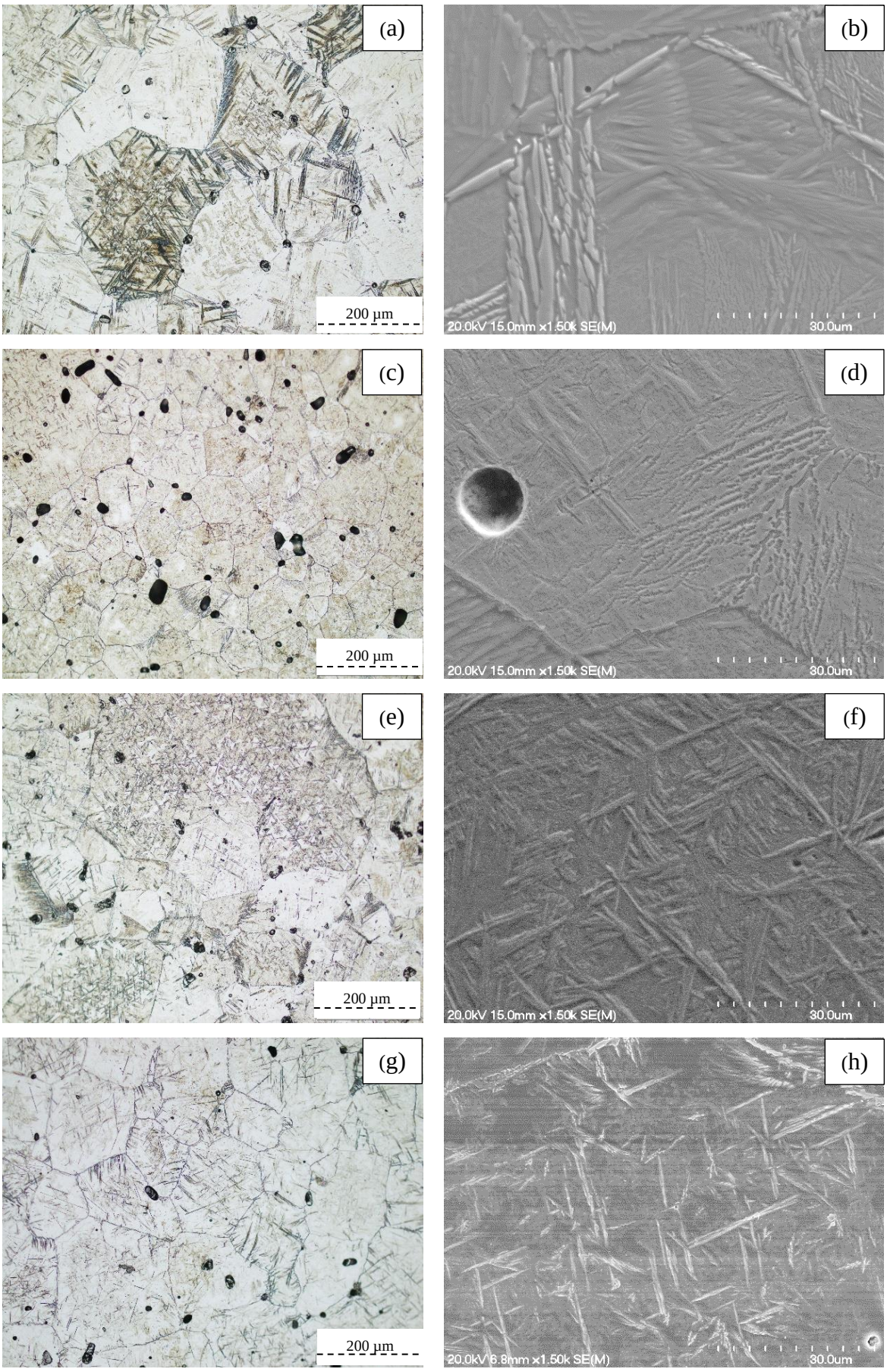

Figure 5.6 Optical and SEM micrograph of (a, b) Ti-2Nb-8Mn, (c, d) Ti-6Nb-8Mn, (e, f) Ti-4Nb-7Mn and (g, h) Ti-4Nb-9Mn corresponding to the Ti-8Mn and Ti-4Nb systems, respectively.

From the XRD spectra and micrographs, it is clear that all alloys belonging to the Ti-8Mn and Ti-4Nb systems, are characterised primarily by equiaxed β grains with acicular α and minor proportion of Widmanstätten microstructures. Ti-2Nb-8Mn and Ti-4Nb-7Mn consist of closed spherical pores whereas Ti-6Nb-8Mn and Ti-4Nb-9Mn consists of elongated pores. This is in accordance with the relative sintered density values from Table 5.1. i.e. as the sintered density reaches 96% all pores tend to be closed and spherical. Likewise, the trend of the XRD spectra as seen in Figure 5.5, is concurrent with the that of the micrographs where all the alloys show a predominant β phase.

Since all alloys show dominant peaks and the micrographs are characterised by almost equiaxed grains and individual α lamellae and α'' peak Ti-2Nb-8Mn, Ti-6Nb-8Mn, Ti-4Nb-7Mn and Ti-4Nb-9Mn are categorised as metastable β alloys.

Overall, among the Ti-Nb-Mn alloys, the alloys from the Ti-5Mn and Ti-6Mn systems show XRD peaks corresponding to both α and β phases with the gradual emergence of the β peaks with the addition of Nb and Mn (β stabilisers). Correspondingly, the micrographs consist of Widmanstätten microstructures with varying thickness of the lamellae. For the Ti-8Mn and Ti-4Nb systems, the XRD spectra consists primarily by dominant β peaks where the α peaks are suppressed. Of them, Ti-4Nb-9Mn shows a tiny peak corresponding to the orthorhombic phase. Similarly, the micrographs consist of acicular α lamellae with minor proportions of Widmanstätten microstructures. The nature of porosity (mixture of closed and elongated) observed in the micrographs is in line with the density values (≥ 95%) mentioned in Table 5.1 and Table 5.2.

Based on the XRD spectra from Figure 5.3 and Figure 5.5, micrographs Figure 5.4 and Figure 5.6) and MoE (4-1) values (Table 4.2), Ti-1Nb-5Mn, Ti-5Nb-5Mn and Ti-3Nb-6Mn are categorised as β matrix α+β alloy, Ti-6Nb-6Mn as near β and all alloys from the Ti-4Nb systems as metastable β [80].

5.1.3 Mechanical Properties

5.1.3.1 Ti-5Mn and Ti-6Mn systems

Table 5.3 shows the mechanical properties of C.P. Ti, Ti-1Nb-5Mn, Ti-5Nb-5Mn, Ti-3Nb-6Mn and Ti-6Nb-6Mn from the Ti-5Mn and Ti-6Mn systems, respectively. It is seen that C.P. Ti has the lowest yield and ultimate tensile strength of 453 and 588 MPa. However, it exhibits the highest elongation to failure of 10.3%. Among the other alloys, Ti-1Nb-5Mn and Ti-6Nb-

6Mn has the lowest and highest yield and ultimate tensile strength, respectively. Further, Ti-5Nb-5Mn exhibits the highest elongation to failure. The hardness values range between 66 - 67.5 HRA for Ti-1Nb-5Mn and Ti-6Nb-6Mn, respectively.

Table 5.3 Mechanical properties of C.P. Ti, Ti-1Nb-5Mn, Ti-5Nb-5Mn, Ti-3Nb-6Mn and Ti-6Nb-6Mn corresponding to the Ti-5Mn and Ti-6Mn systems, respectively.

System	Material	Alloying elements (wt%)	YS (MPa)	UTS (MPa)	Elongation (%)	Hardness (HRA)
	C.P. Ti	0	453 ± 38	588 ± 42	10.3 ± 2.2	58.4 ± 2.0
Ti-5Mn	Ti-1Nb-5Mn	6	778 ± 41	841 ± 61	2.6 ± 1.2	65.8 ± 0.4
	Ti-5Nb-5Mn	10	822 ± 20	904 ± 7	5.0 ± 1.5	66.3 ± 0.7
Ti-6Mn	Ti-3Nb-6Mn	9	833 ± 14	889 ± 14	2.9 ± 0.5	66.0 ± 1.1
	Ti-6Nb-6Mn	12	927 ±31	979 ± 13	3.4 ± 2.2	67.4 ± 0.8

Figure 5.7 shows the relationship between the strength and ductility of C.P. Ti, Ti-1Nb-5Mn, Ti-5Nb-5Mn, Ti-3Nb-6Mn and Ti-6Nb-6Mn from the Ti-5Mn and Ti-6Mn, respectively. It is seen that the yield and ultimate tensile strength gradually increases with the addition of Nb and Mn. It can also be seen that the elongation to failure increases with the Nb content along with slight increase in tensile strength.

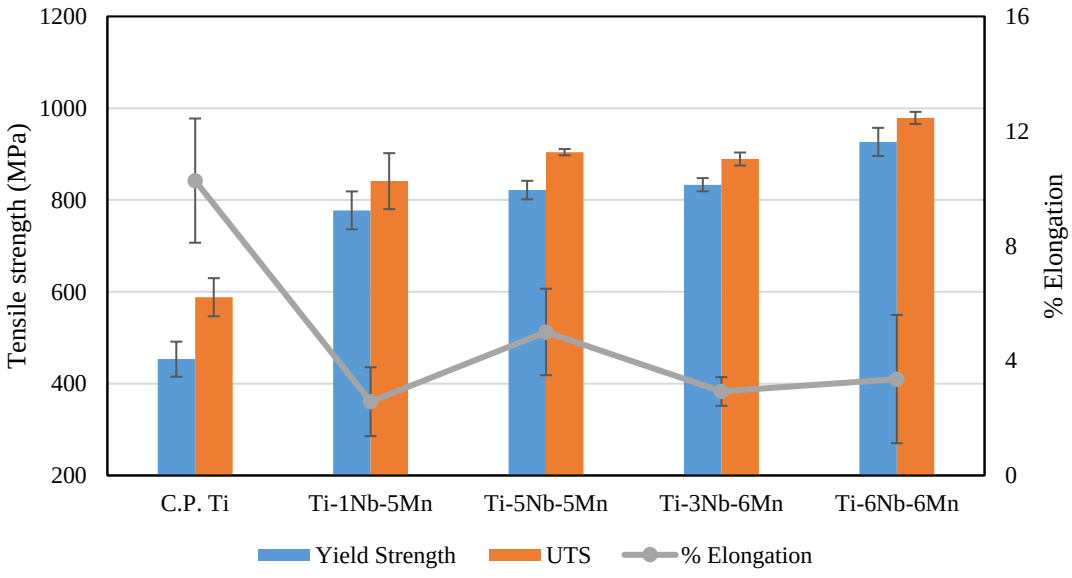

Figure 5.7 Relationship between the strength and ductility of C.P. Ti, Ti-1Nb-5Mn, Ti-5Nb-5Mn, Ti-3Nb-6Mn and Ti-6Nb-6Mn corresponding to theTi-5Mn and Ti-6Mn systems, respectively.

From Table 5.3, it is evident that the alloying elements is proportionate to the increase in the yield and ultimate tensile strength. Hence, the increase in strength noticed in both Ti-5Mn and

Ti-6Mn alloys can be attributed to the addition of alloying elements. The addition of Mn and Nb causes solid solution strengthening where the substitutional alloying elements obstruct the movement of the dislocations thereby demanding higher load to help the movement of dislocations resulting in increased strength [85; 86]. Similarly, as seen in Figure 5.7, the trend of elongation to failure is the converse of that of strength. On top of that, the addition of β stabilisers causes the β transus to drop thereby arresting the growth of α lamellae [87]. This causes a refinement in the thickness of the α+β lamellae causing the decrease in inter-lamellar spacing. The SEM micrographs as seen in Figure 5.4 clearly depicts the refinement occurring due to the addition of β stabilisers (Nb and Mn). According to Hall-Petch relationship, grain size is inversely related to the strength [88]. The increase in the proportion of the β phase also becomes evident from the XRD spectra as seen in Figure 5.3.

α+β alloys with their biphasic microstructure have a good combination of mechanical properties especially when compared with α-Ti alloys [8]. Therefore, addition of alloying elements has resulted in the increase in both strength and ductility. However, with further addition of alloying elements the increase in strength occurs with little compromise to ductility.

Figure 5.8 displays the Rockwell hardness vs alloying elements trend of C.P. Ti, Ti-1Nb-5Mn, Ti-5Nb-5Mn, Ti-3Nb-6Mn and Ti-6Nb-6Mn corresponding to the Ti-5Mn and Ti-6Mn systems, respectively. It is seen that the hardness values gradually increase with the addition of alloying elements. It is worth mentioning that the trend of hardness is similar to that of tensile strength.

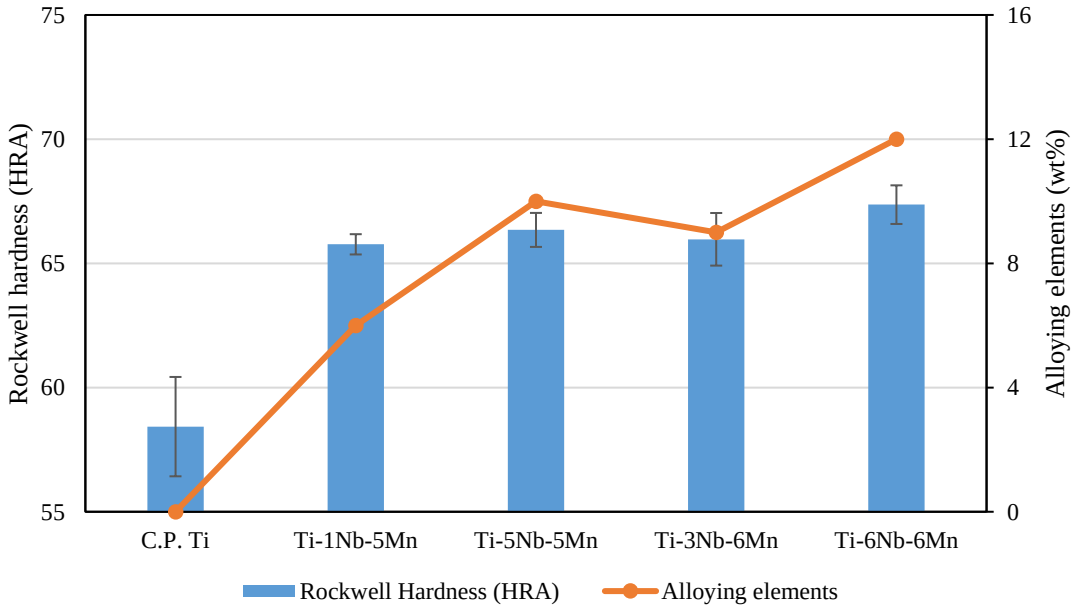

Figure 5.8 Rockwell Hardness vs alloying elements of C.P. Ti, Ti-1Nb-5Mn, Ti-5Nb-5Mn, Ti-3Nb-6Mn and Ti-6Nb-6Mn corresponding to theTi-5Mn and Ti-6Mn systems, respectively.

The increase in hardness due to the addition of alloying elements can also be attributed on the basis of solid solution strengthening. Due to the addition of alloying elements, the resistance to indentation increases which in turn causes the hardness to increase. From Figure 5.8, it can be observed that the increase in hardness in the Ti-6Mn system is higher than that of the Ti-5Mn. A similar (inverse) trend is observed in the elongation to failure values (Figure 5.7).

For the alloys from the Ti-5Mn and Ti-6Mn systems, the strength and hardness gradually increase with the addition of β stabilisers. It is seen that both strength and ductility increase which is a characteristic of α+β alloys, which is in line with the XRD spectra and micrographs (Figure 5.3 and Figure 5.4).

5.1.3.2 Ti-8Mn and Ti-4Nb systems

Table 5.4 displays the mechanical properties of C.P. Ti, Ti-2Nb-8Mn, Ti-6Nb-8Mn, Ti-4Nb-7Mn and Ti-4Nb-9Mn corresponding to the Ti-8Mn and Ti-4Nb systems, respectively. C.P. Ti has the lowest yield and ultimate tensile strength of 453 MPa and 588 MPa, respectively and it exhibits the highest elongation to failure of 10.3%. Among the other alloys, the yield strength ranges between 972 MPa for Ti-4Nb-7Mn to 1050 MPa for Ti-6Nb-8Mn. No yield strength was observed for Ti-4Nb-9Mn as it failed elastically. It is worth mentioning that the elongation to failure for all alloys from the Ti-8Mn and Ti-4Nb system is 1.5% (±0.2). Ti-6Nb-8Mn exhibits the highest yield strength of 1050 MPa. The hardness values range between 67-69.5 HRA for Ti-4Nb-7Mn and Ti-4Nb-9Mn, respectively.

Table 5.4 Mechanical properties of Ti-2Nb-8Mn, Ti-6Nb-8Mn, Ti-4Nb-7Mn and Ti-4Nb-9Mn corresponding to the Ti-8Mn and Ti-4Nb systems, respectively.

System	Material	Alloying elements (wt%)	YS (MPa)	UTS (MPa)	Elongation (%)	Hardness (HRA)
	C.P. Ti	0	453 ± 38	588 ± 42	10.3 ± 2.2	58.4 ± 2.0
Ti-8Mn	Ti-2Nb-8Mn	10	1022 ±20	1050 ± 32	1.6 ± 0.2	69.1 ± 0.8
	Ti-6Nb-8Mn	14	1050 ± 10	1090 ± 19	1.7 ± 0.1	68.5 ± 1.0
Ti-4Nb	Ti-4Nb-7Mn	11	972 ± 10	1001 ± 9	1.7 ± 0.1	67.2 ± 0.8
	Ti-4Nb-9Mn	13	-	1037 ± 69	1.3 ± 0.2	69.5 ± 0.8

Figure 5.9 illustrates the relationship between strength and ductility of C.P. Ti, Ti-2Nb-8Mn, Ti-6Nb-8Mn, Ti-4Nb-7Mn and Ti-4Nb-9Mn corresponding to the Ti-8Mn and Ti-4Nb systems, respectively. It is seen that the yield and ultimate tensile strength gradually increases

with the addition of Nb and Mn, whereas there is no change in elongation to failure. It is clear that Ti-4Nb-9Mn failed elastically.

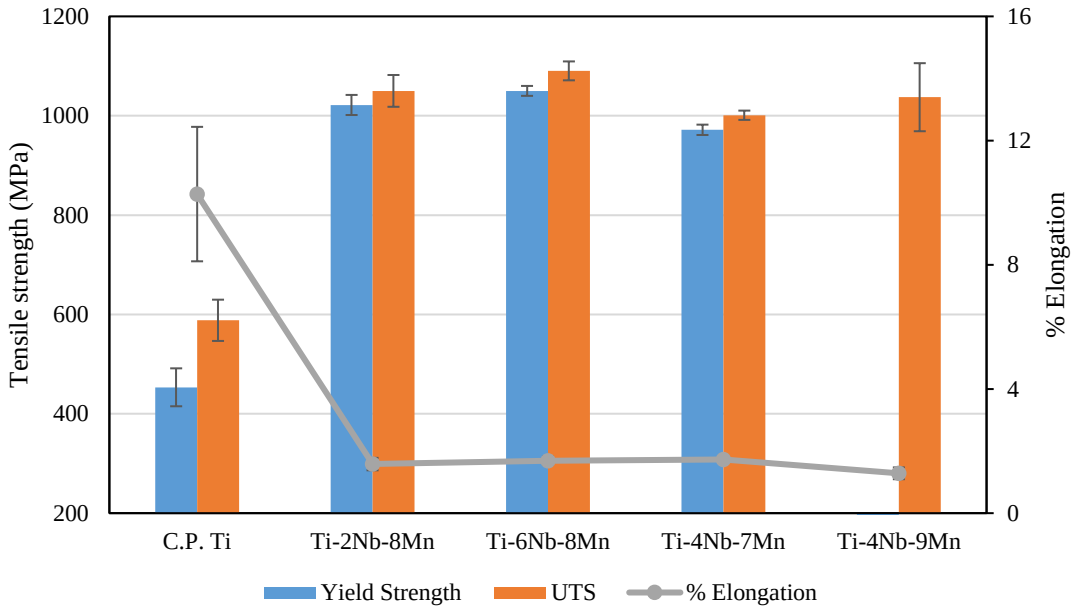

Figure 5.9 Relationship between the strength and ductility of C.P. Ti, Ti-2Nb-8Mn, Ti-6Nb-8Mn, Ti-4Nb-7Mn and Ti-4Nb-9Mn corresponding to the Ti-8Mn and Ti-4Nb systems, respectively.

From Figure 5.9**,** it can be seen that all alloys except Ti-4Nb-7Mn show almost equal values of ultimate tensile strength (based on the standard deviation). However, the elongation to failure values remain constant for all the alloys. Despite the differences in the density values, all the alloys from the Ti-8Mn and Ti-4Nb system have high tensile strength. The only exception being Ti-4Nb-7Mn which is characterised by a mixture of Widmanstätten microstructures and few regions of acicular α. Such a behaviour can be attributed to the presence of acicular α lamellae in all the alloys. In addition to the orthorhombic phase detected in Ti-4Nb-9Mn. The fine acicular α lamellae has a significant effect in obstructing the dislocations. As discussed in Chapter 5.1.3.1, the effect of adding alloying elements result in solid solution strengthening which in turn causes the strength values to spike [86]. The same can be attributed to the severe decline in ductility. Especially, for the Ti-6Nb-8Mn with large elongated pores as seen in Figure 5.6 (c, d). The formation of acicular α is a result of dominant β peaks with a few minor α peaks which is evident from the XRD spectra (as seen in Figure 5.5) of the alloys from Ti-8Mn and Ti-4Nb systems.

Figure 5.10 displays the Rockwell hardness vs alloying elements trend for C.P. Ti, Ti-2Nb-8Mn, Ti-6Nb-8Mn, Ti-4Nb-7Mn and Ti-4Nb-9Mn corresponding to the Ti-8Mn and Ti-4Nb systems, respectively. For Ti-2Nb-8Mn and Ti-6Nb-8Mn, despite the increase in alloying

elements the hardness values do not change. However, with Ti-4Nb-7Mn and Ti-4Nb-9Mn, there is a direct dependence between the alloying elements and Rockwell hardness. Ti-4Nb-7Mn and Ti-4Nb-9Mn exhibit the highest and lowest hardness, respectively.

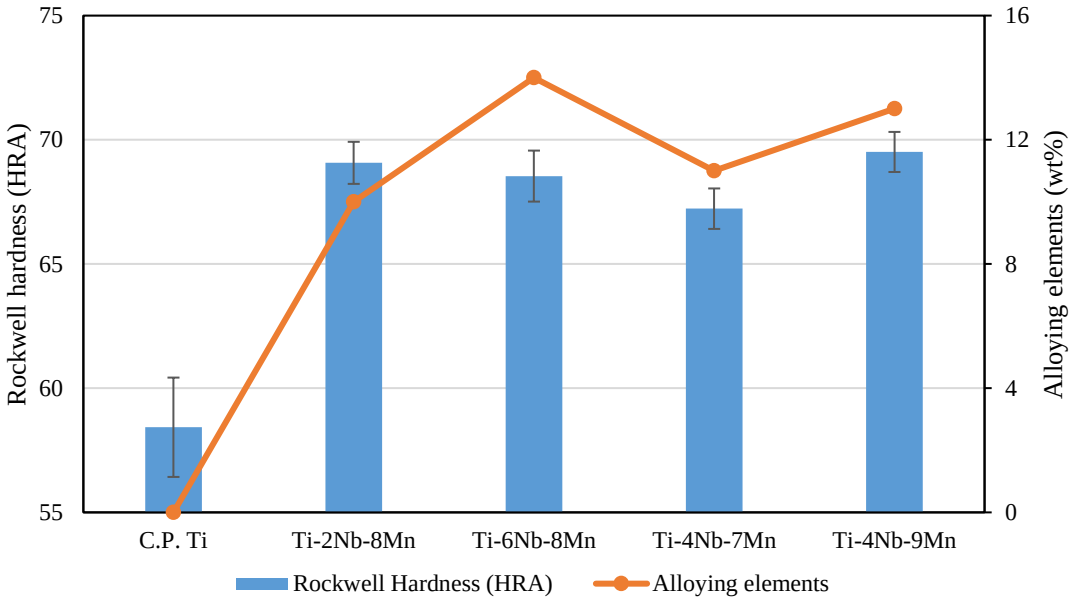

Figure 5.10 Rockwell Hardness vs alloying elements for Ti-2Nb-8Mn, Ti-6Nb-8Mn, Ti-4Nb-7Mn and Ti-4Nb-9Mn corresponding to the Ti-8Mn and Ti-4Nb systems, respectively.

The drop in the hardness values despite the addition of alloying elements in Ti-6Nb-8Mn can be attributed to the increased distribution of spherical and elongated pores as seen in Figure 5.6(c, d). For the Ti-4Nb-9Mn the presence of orthorhombic α'' increases the strength and hardness [70]. For the other alloys, the hardness values follow a trend that is similar to that of the tensile strength as the substitutional alloying elements increases the resistance to indentation.

For the Ti-Nb-Mn alloys, the Ti-1Nb-5Mn and Ti-6Nb-8Mn shows the highest tensile strength (841 MPa and 1090 MPa, respectively) and Ti-5Nb-5Mn shows the highest elongation to failure. With the addition of alloying elements, despite the decrease in density, the increase in strength is due to solid solution strengthening and grain boundary strengthening. It can be inferred from Figure 5.7, that addition of Nb, helps improve ductility. However, the presence of elongated pores and acicular α in Ti-6Nb-8Mn reasons for the brittle behaviour. It is worth mentioning that hardness also follows a similar trend as tensile strength. It is seen that both strength and ductility increase for the alloys from the Ti-5Mn and Ti-6Mn systems. This is due to the presence of dominant α peaks amidst few β peaks. This is representative of α+β alloys. However, for the Ti-8Mn and Ti-4Nb systems, the tensile strength is very high and the ductility

is relatively low. This is attributed to the presence of prominent β peaks amidst minimal α peaks, acicular α lamellae and the orthorhombic α''. Such is a characteristic of a metastable β alloy.

5.1.4 Fractography

5.1.4.1 Ti-5Mn and Ti-6Mn

Figure 5.11 shows the representative fractographs of Ti-1Nb-5Mn, Ti-5Nb-5Mn, Ti-3Nb-6Mn and Ti-6Nb-6Mn corresponding to the Ti-5Mn and Ti-6Mn systems, respectively . Figure 5.11a represents the fracture surface of Ti-1Nb-5Mn alloy. It can be seen that the surface is characterised by a mixture of dimples and smooth flat surfaces. The dimple like features indicate a ductile failure while the latter indicate brittle fracture [59]. Further, the hollow structures found in all the images represent the nature of porosity. The hemispherical topography is due to the fracture occurring at the spherical pores. Figure 5.11**b** represents the fracture surface of Ti-5Nb-5Mn alloy and it primarily consists of dimple like features and hemispheres indicating spherical pores. This is indicative of the fact that addition of Nb helps to improve ductility [45]. The presence of elongated pores in Figure 5.11b is line with the density values of Table 5.1 The fracture surface of Ti-3Nb-6Mn majorly consists of tiny patches of dimples alongside river like features. This is also reflective of the poor ductility behaviour seen in Figure 5.7**.** With increase in Nb, unlike Ti-5Nb-5Mn the fracture surface of Ti-6Nb-6Mn is completely characterised by a cleavage and few regions of flat surfaces. In addition, the surface also consists of slightly elongated pores.

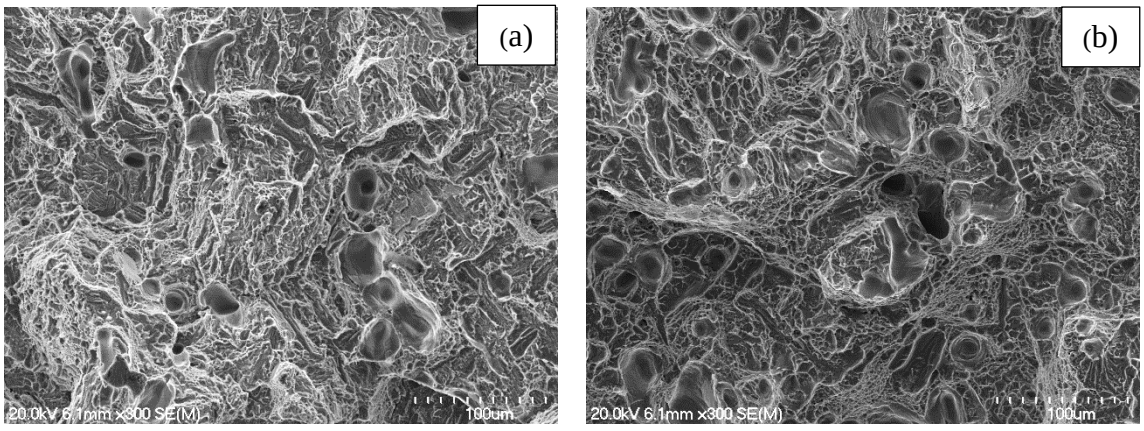

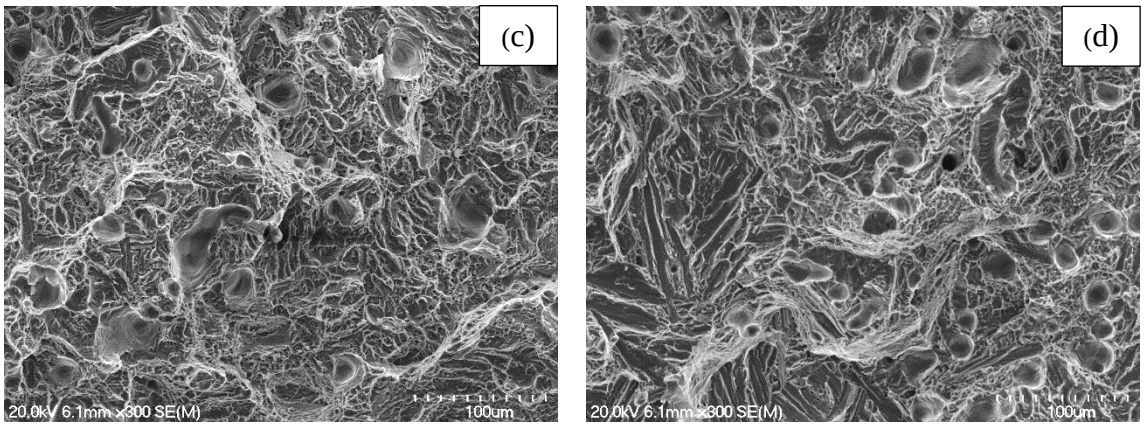

Figure 5.11 Representative fractographs of a) Ti-1Nb-5Mn, b) Ti-5Nb-5Mn, c) Ti-3Nb-6Mn and d) Ti-6Nb-6Mn corresponding to the Ti-5Mn and Ti-6Mn systems, respectively.

5.1.4.2 Ti-8Mn and Ti-4Nb systems

Figure 5.12 represents the fracture surface of Ti-2Nb-8Mn, Ti-6Nb-8Mn, Ti-4Nb-7Mn and Ti-4Nb-9Mn corresponding to the Ti-8Mn and Ti-4Nb systems, respectively. It can be seen that all alloys are characterised by tear-ridge, river like patterns and clear facets which is indicative of brittle fracture [59]. Large elongated pores can also be observed along the grain boundaries of Ti-6Nb-8Mn. As a result of containing a few regions of Widmanstätten microstructures besides the individual α lamellae in Ti-4Nb-7Mn and shows a few dimples.

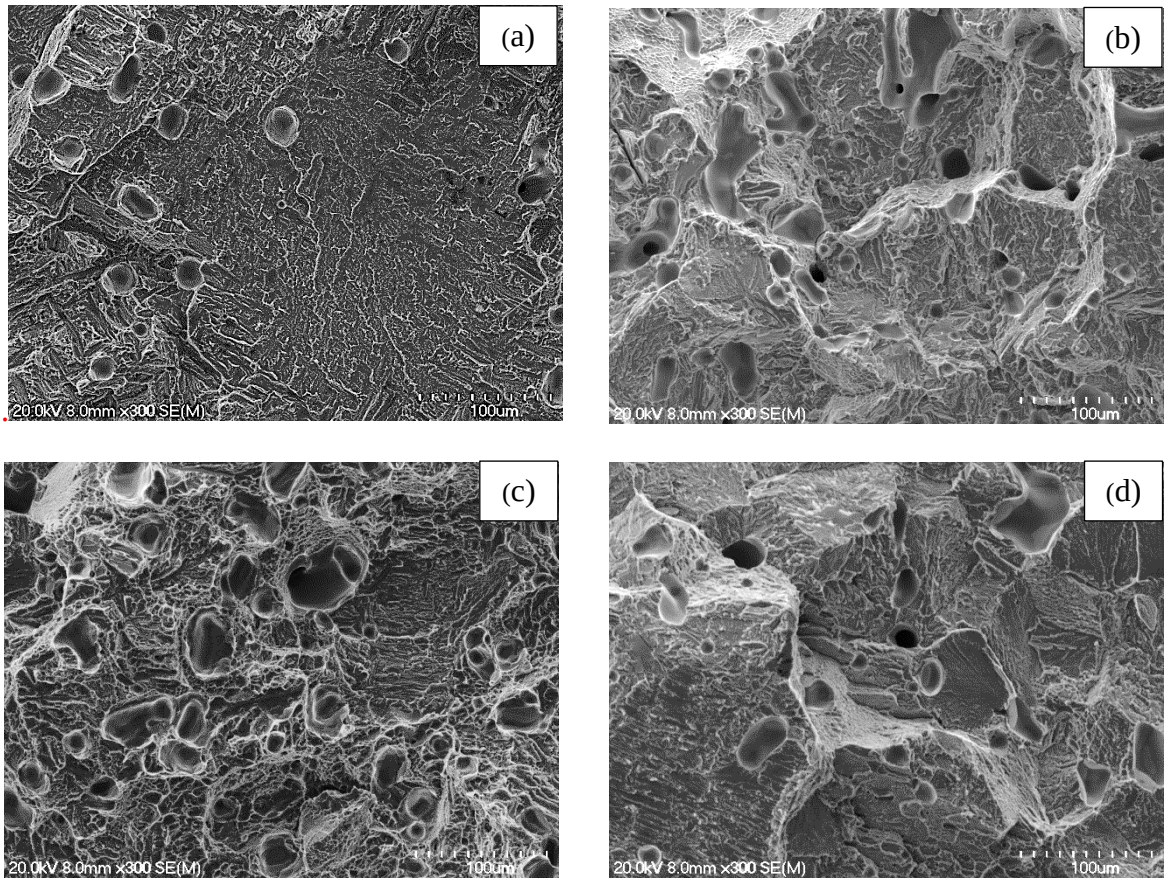

Figure 5.12 Representative fractographs of a) Ti-2Nb-8Mn, b) Ti-6Nb-8Mn, c) Ti-4Nb-7Mn and d) Ti-4Nb-9Mn alloys corresponding to the Ti-8Mn and Ti-4Nb systems, respectively.

The presence of porosity and metastable α'' also causes a brittleness which becomes evident in the case of Ti-6Nb-8Mn and Ti-4Nb-9Mn, respectively.

Summarising the behaviour of all Ti-Nb-Mn alloys in the Ti-5Mn and Ti-6Mn systems there is no huge change in the green density due to the morphology and particle size of the elemental powders. A mixture of large angular and medium sized irregularly shaped powders when warm pressed aid in better mechanical interlocking [2; 24]. However, for Ti-8Mn and Ti-4Nb systems, the green density tend to decrease, especially for the Ti-6Nb-8Mn. It is speculated that the resistance to compaction tend to escalate beyond a critical value of 6wt% of Nb. There is a gradual decline in the sintered density values of the alloys. This is due to the poor diffusivity of Nb in Ti. However, all alloys have a sintered density above 95% indicating that the alloys have reached the final stage of sintering. The alloys from the Ti-4Nb system possess the lowest decrease in densification. The high diffusivity of Mn can be attributed to the increased densification [70]. The nature of porosity as observed from the micrographs and fractography (Figure 5.4 and Figure 5.11, respectively) is in-line with the density values mentioned in Table 5.1and Table 5.2.

From the XRD spectra of alloys from the Ti-5Nb and Ti-6Nb systems it is seen that the addition of Nb and Mn gradually helps to stabilise the β phase. This becomes evident from Figure 5.3, as the β peaks gradually emerges. The stabilisation of the β phase causes refinement in the microstructures as seen in Figure 5.4. However, from Figure 5.3 it is evident that all the alloys from the Ti-8Mn and Ti-4Nb systems exhibit prominent β peaks indicating that these alloys consist of a major proportion of the β phase. This becomes conclusive from the optical and SEM micrographs that are primarily characterised by equiaxed β grains and varying proportions of acicular α lamellar for different alloys.

Ti alloys are categorised as β matrix α+β alloys (MoE≤ 5), near β (5 ≤ MoE ≤10), metastable β (10 ≤ MoE ≤30) and fully stable β (MoE ≥ 30) [80; 87]. Keeping these MoE ranges as baseline the alloys were classified on the basis of their XRD and microstructures.

Based on the the XRD spectra and micrographs it can be concluded that Ti-1Nb-5Mn, Ti-5Nb-5Mn and Ti-3Nb-6Mn are β matrix α+β alloys, Ti-6Nb-6Mn as near β and all alloys from the Ti-4Nb systems as metastable β alloys. Table 5.5 shows the classification of Ti-Nb-Mn alloys and their MoE values (from equation (4-1) and (4-2)). As stated in Chapter 4.2, the MoE values calculated from equation (4-1) is more consistent with the experimentally observed results.

Table 5.5 Classification of Ti-Nb-Mn alloys.

System	Material	MoE (4-1)	MoE (4-2)	Classification
Ti-5Mn	Ti-1Nb-5Mn	8.0	11.6	β matrix α+β
	Ti-5Nb-5Mn	9.1	12.7	β matrix α+β
Ti-6Mn	Ti-3Nb-6Mn	10.1	14.4	β matrix α+β
	Ti-6Nb-6Mn	11.0	15.2	near β
Ti-8Mn	Ti-2Nb-8Mn	12.9	18.6	Metastable β
	Ti-6Nb-8Mn	14.0	19.8	Metastable β
Ti-4Nb	Ti-4Nb-7Mn	11.9	16.9	Metastable β
	Ti-4Nb-9Mn	15	21.5	Metastable β

The presence of different phases, their morphology and proportion reflect on the mechanical properties of the Ti-Nb-Mn alloys. For the Ti-5Mn and Ti-6Mn systems, despite the drop in the density, an increase in tensile strength is observed. Alongside, a gradual increase in ductility is also observed. However, due to extensive refinement the increase in ductility for the Ti-6Nb system is relatively less when compared with the Ti-5Mn system. The Rockwell hardness of the alloys also follow a similar trend as that of the tensile strength. With the addition of alloying elements, the hardness gradually increases. From the fractography of the alloys from the Ti-5Mn and Ti-6Mn systems, it becomes clear that the ductility is more dependent on the microstructural features than the porosity.

On the other hand, all the alloys from the Ti-8Mn and Ti-4Nb system in general exhibit a brittle behaviour. The presence of acicular α lamellae is primarily attributed to the increase in strength and brittle failure of all the alloys. In addition, a tiny peak corresponding to the α'' orthorhombic phase was found in Ti-4Nb-9Mn. Further, the presence of large number of spherical and elongated pores reasoned especially for Ti-6Nb-8Mn. The Fractographs clearly illustrate the presence of flat facets and cleavages for all the Ti-Nb-Mn alloys. It is worth mentioning that all the alloys possess tensile strengths almost twice of that of C.P. Ti however, the elongation to failure values is relatively less.

Figure 5.13 displays the tensile strength of various biomedical α+β and metastable β alloys and that of the Ti-Nb-Mn alloys from the current research. It is seen that Ti-6Nb-8Mn shows the highest ultimate tensile strength (1090 MPa) among the other alloys in Figure 5.13 while Ti-2Nb-8Mn (1050 MPa) are comparable with Ti-6Al-7Nb (1050 MPa) and Ti-5Al-2.5Fe (1033 MPa). It is worth mentioning that the tensile strength of Ti-4Nb-7Mn (1001 MPa) is comparable with Ti-35Nb-5Ta-4.6Zr (1010 MPa). In general, all of the metastable and near β Ti-Nb-Mn alloys have comparable and/or higher tensile strength than the existing first generation and second generation of biomedical alloys.

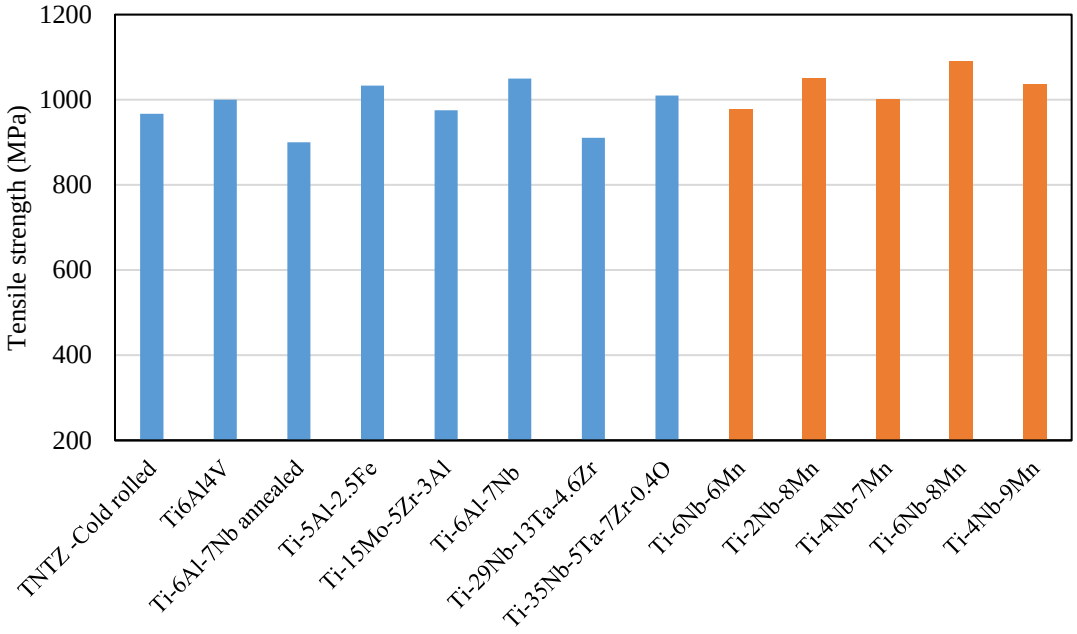

Figure 5.13 Tensile strength of various biomedical α+β, metastable alloys and near β/metastable Ti-Nb-Mn alloys from the current research [4; 41; 89-92].

5.2 Ti-Nb-Fe system

5.2.1 Density and porosity measurements

5.2.1.1 Ti-2Nb system

Table 5.6 displays physical properties of C.P. Ti, Ti-2Nb-3Fe, Ti-2Nb-5Fe and Ti-2Nb-6Fe alloys corresponding to the Ti-2Nb system. The density mentioned in Table 5.6 and discussed further denote the relative density (%). C.P. Ti has the highest green and sintered density and correspondingly highest densification. The green density of Ti-2Nb-3Fe, Ti-2Nb-5Fe and Ti-2Nb-6Fe do not seem to vary much. The slight decrease is attributed to the increase in Fe content. The decrease in densification is negligible and is mainly due to the changes in green density.

Table 5.6 Physical properties of C.P. Ti, Ti-2Nb-3Fe, Ti-2Nb-5Fe and Ti-2Nb-6Fe alloys corresponding to the Ti-2Nb system.

System	Material	ρ_{green} (%)	$\rho_{sintered}$ (%)	Porosity (%)	Densification Ψ (%)	Decrease in densification (%)
	C.P. Ti	96.2	99.0 ± 0.1	1.0	72.8	-
Ti-2Nb	Ti-2Nb-3Fe	94.1	98.4 ± 0.9	1.6	72.5	2.1
	Ti-2Nb-5Fe	93.8	98.2 ± 0.2	1.8	71.0	
	Ti-2Nb-6Fe	93.5	98.0 ± 0.2	2.0	68.7	5.2

Figure 5.14 shows the relationship between densification and porosity for Ti-2Nb-3Fe, Ti-2Nb-5Fe and Ti-2Nb-6Fe alloys corresponding to the Ti-2Nb system. It can be seen that the porosity gradually increases with the addition of Fe. However, the increase is negligible (~1%).

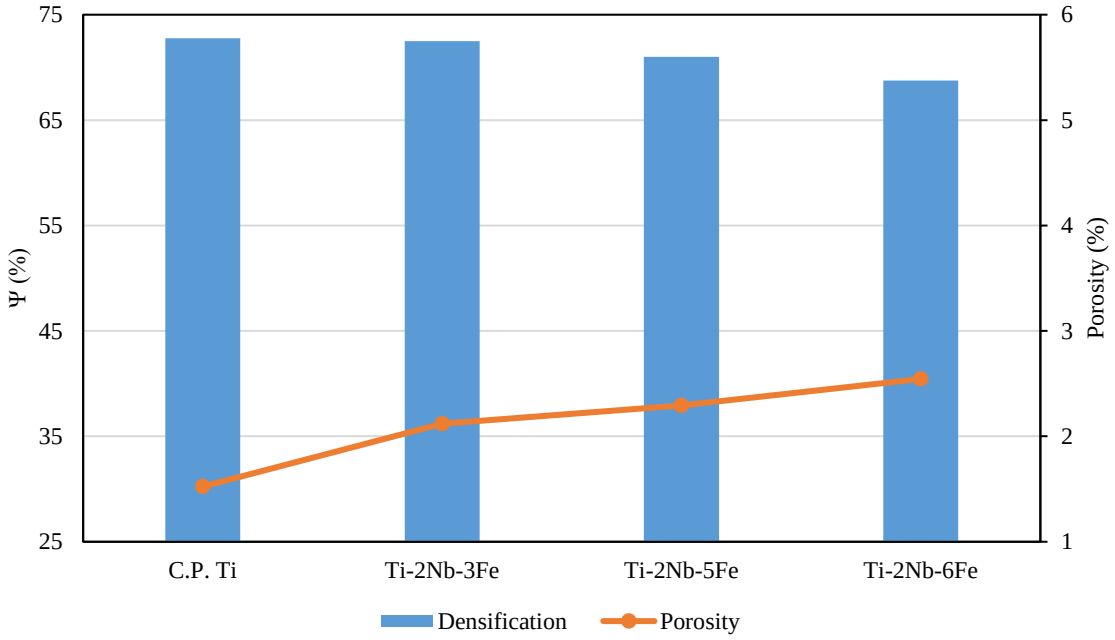

Figure 5.14 Relationship between densification and porosity for C.P. Ti, Ti-2Nb-3Fe, Ti-2Nb-5Fe and Ti-2Nb-6Fe alloys corresponding to the Ti-2Nb system.

The increase in Fe content increases the resistance during compaction as spherical powders are more difficult to press. In addition, finer powders require more pressure than coarse powders. Despite that, finer powders tend to aid sintering due to their short diffusion paths and high surface energies. Thus, the change in density is very negligible.

5.2.1.2 Ti-5Nb and Ti-6Nb systems

Table 5.7 shows the physical properties of C.P. Ti, Ti-5Nb-3Fe, Ti-5Nb-4Fe, Ti-6Nb-5Fe and Ti-6Nb-6Fe alloys corresponding to the Ti-5Nb and Ti-6Nb systems, respectively. The difference in the green density values between the alloys from the individual system is small (~1%). Similarly, there is no huge difference in the sintered density. The slight changes in green density is due to the addition of alloying elements that tend to increase the resistance to compaction.

Table 5.7 Physical properties of C.P. Ti, Ti-5Nb-3Fe, Ti-5Nb-4Fe, Ti-6Nb-5Fe and Ti-6Nb-6Fe alloys corresponding to the Ti-5Nb and Ti-6Nb systems, respectively.

System	Material	ρ_{green} (%)	$\rho_{sintered}$ (%)	Porosity (%)	Densification Ψ (%)	Decrease in densification (%)
	C.P. Ti	96.2	99.0 ± 0.1	1.0	72.8	-
Ti-5Nb	Ti-5Nb-3Fe	92.7	97.2 ± 0.4	2.8	61.5	7.8
	Ti-5Nb-4Fe	91.7	96.4 ± 1.1	3.6	56.7	
Ti-6Nb	Ti-6Nb-5Fe	91.3	96.4 ± 0.1	3.6	58.6	9.4
	Ti-6Nb-6Fe	92.2	96.3 ± 0.1	3.7	53.1	

Figure 5.15 shows the relationship between densification and porosity for C.P. Ti, Ti-5Nb-3Fe, Ti-5Nb-4Fe, Ti-6Nb-5Fe and Ti-6Nb-6Fe corresponding to the Ti-5Nb and Ti-6Nb systems. It is seen that the densification gradually decreases with the addition of Fe for both the systems. As a result, porosity increases slightly for the Ti-5Nb system, but remains constant for the Ti-6Nb system. Fine Fe powders with high surface energy, short diffusion paths and high diffusivity is the reason for the porosity values to remain constant in the Ti-6Nb system

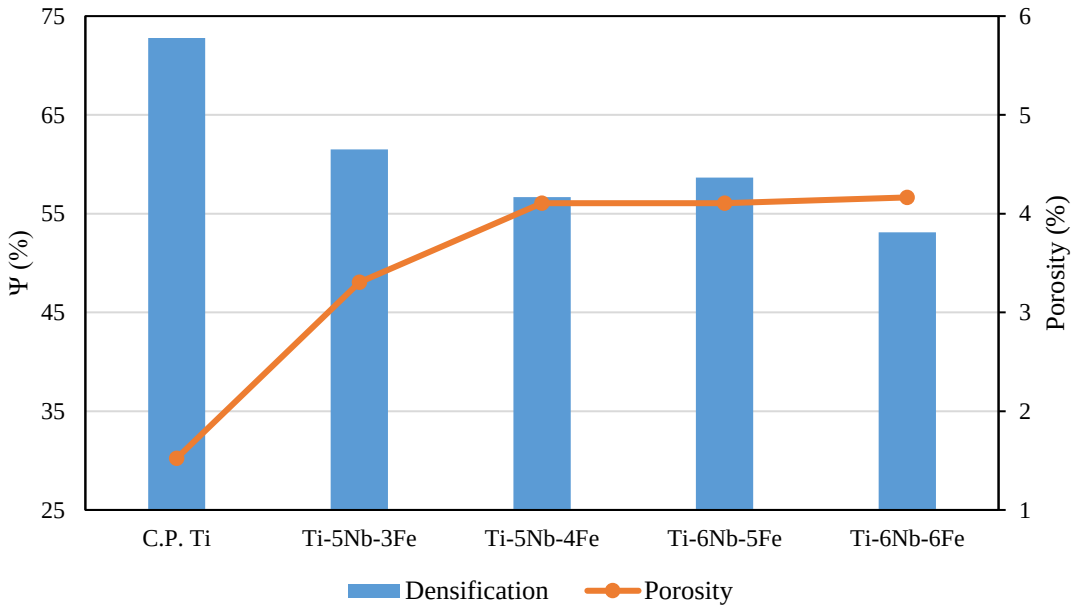

Figure 5.15 Relationship between densification and porosity for C.P. Ti, Ti-5Nb-3Fe, Ti-5Nb-4Fe, Ti-6Nb-5Fe and Ti-6Nb-6Fe corresponding to the Ti-5Nb and Ti-6Nb systems, respectively.

As explained previously, the addition of alloying elements generally increases the resistance to compaction. On the other hand, the high diffusivity of Fe is attributed to the little to no change in the sintered density [37].

5.2.1.3 Ti-8Nb and Ti-9Nb systems

Table 5.8 displays the physical properties of C.P. Ti, Ti-8Nb-2Fe, Ti-8Nb-4Fe, Ti-9Nb-5Fe and Ti-9Nb-6Fe alloys corresponding to the Ti-8Nb and Ti-9Nb systems, respectively. The green density values of the alloys belonging to both the systems vary slightly (~1.5%). It is notable that the densification values increase with the addition of Fe in both the systems as a result there is no huge difference in the sintered density of the alloys.

Table 5.8 Physical properties of C.P. Ti, Ti-8Nb-2Fe, Ti-8Nb-4Fe, Ti-9Nb-5Fe and Ti-9Nb-6Fe alloys corresponding to the Ti-8Nb and Ti-9Nb systems, respectively.

System	Material	ρ_{green} (%)	$\rho_{sintered}$ (%)	Porosity (%)	Densification Ψ (%)	Decrease in densification (%)
	C.P. Ti	96.2	99.0 ± 0.1	1.0	72.8	-
Ti-8Nb	Ti-8Nb-2Fe	91.6	95.6 ± 0.0	4.4	47.7	- 13.3
	Ti-8Nb-4Fe	89.9	95.4 ± 0.2	4.6	54.1	
Ti-9Nb	Ti-9Nb-5Fe	90.6	95.0 ± 0.2	5.0	46.6	- 13.4
	Ti-9Nb-6Fe	89.8	95.2 ± 0.1	4.8	52.8	

The reason for the drop in the green density values is be due to the Nb content being beyond the critical 6 wt%. It is speculated that the resistance to compaction escalates quickly beyond this critical value. Nevertheless, fine powders with high surface energy and generally high diffusivity of Fe results in balancing the drop in the green density.

Figure 5.16 displays the relationship between densification and porosity for C.P. Ti, Ti-8Nb-2Fe, Ti-8Nb-4Fe, Ti-9Nb-5Fe and Ti-9Nb-6Fe corresponding to the Ti-8Nb and Ti-9Nb systems, respectively. It is noticed that in both the systems, the densification increases. The porosity values tend to slightly increase for the Ti-8Nb system and decreases for the Ti-9Nb system. Nevertheless, the changes are negligible.

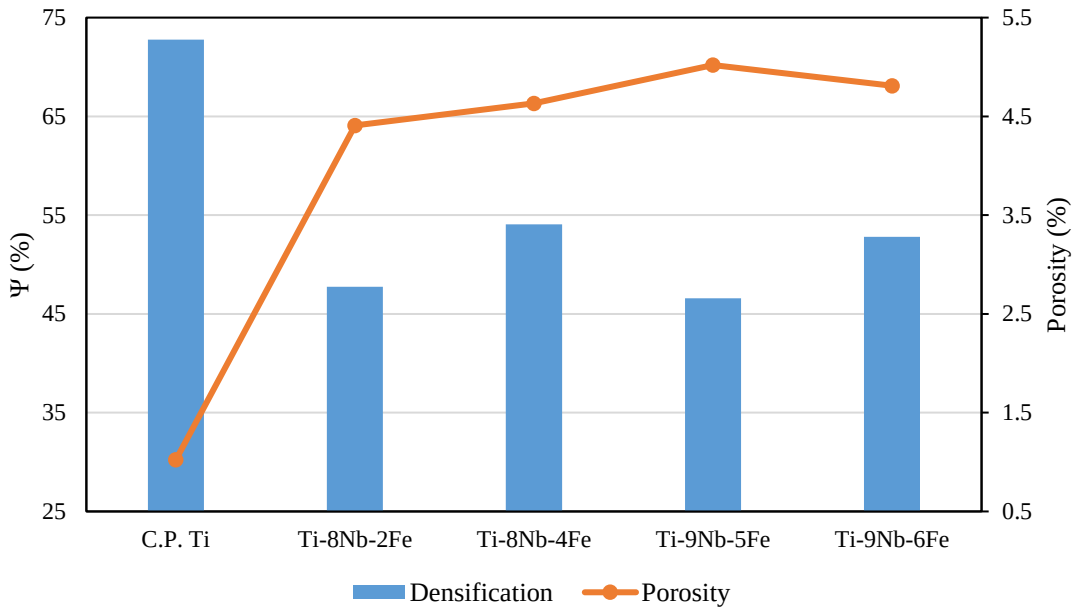

Figure 5.16 Relationship between densification and porosity for C.P. Ti, Ti-8Nb-2Fe, Ti-8Nb-4Fe, Ti-9Nb-5Fe and Ti-9Nb-6Fe corresponding to the Ti-8Nb and Ti-9Nb systems, respectively.

The high diffusivity and the size of elemental Fe powders lead to the increase in the densification for both the systems. As a result, despite the differences in the green density the sintered density values of all the alloys are similar.

5.2.1.4 Ti-4Fe system

Table 5.9 shows the physical properties of C.P. Ti, Ti-3Nb-4Fe, Ti-5Nb-4Fe, Ti-8Nb-4Fe alloys corresponding to the Ti-8Nb and Ti-9Nb systems, respectively. Among the alloys, it can be seen that the green density decreases with the addition of Nb. Except Ti-8Nb-4Fe, all other alloys possess sintered density above 96%. Higher standard deviation is observed for Ti-5Nb-4Fe. The drop in the densification is the highest between Ti-3Nb-4Fe and Ti-8Nb-4Fe.

Table 5.9 Physical properties of C.P. Ti, Ti-3Nb-4Fe, Ti-5Nb-4Fe, Ti-8Nb-4Fe alloys corresponding to the Ti-4Fe systems.

System	Material	$\rho_{relative\ green}$ (%)	$\rho_{sintered}$ (%)	Porosity (%)	Densification Ψ (%)	Decrease in densification (%)
	C.P. Ti	96.2	99.0 ± 0.1	1.0	72.8	-
Ti-4Fe	Ti-3Nb-4Fe	94.5	98.2 ± 0.7	1.8	66.9	15.3
	Ti-5Nb-4Fe	91.7	96.4 ± 1.1	3.6	56.7	
	Ti-8Nb-4Fe	89.9	95.4 ± 0.2	4.6	54.1	19.2

With the addition of alloying elements, the resistance to compaction generally increases. The nature of the elemental Nb and Fe powders can be attributed to observable change in the green density. Besides the spherical morphology of Fe powders are tedious to press due to their aspect ratio[2]. It is speculated that there is a critical Nb content beyond which the resistance to compaction rapidly increases. In order to overcome the difficulty involved in pressing spherical powders, the finer Fe powders were chosen as they tend to sinter effectively due to their short diffusion paths. High diffusivity of Fe is also be attributed to the increment in the sintered density. On the contrary, the huge drop in the densification especially between Ti-3Nb-4Fe and Ti-8Nb-4Fe is due to the poor diffusivity of Nb powders [70].

Figure 5.17 represents the relationship between densification and porosity for Ti-3Nb-4Fe, Ti-5Nb-4Fe and Ti-8Nb-4Fe Ti-9Nb-6Fe corresponding to the Ti-4Fe system. It can be clearly seen that increasing the amount of Nb significantly affects the sintered density and this behaviour is attributed to the poor diffusivity of Nb in Ti. The change in density due to increase in Fe content is relatively less when compared to the change (decrease) in density due to the addition of Nb.

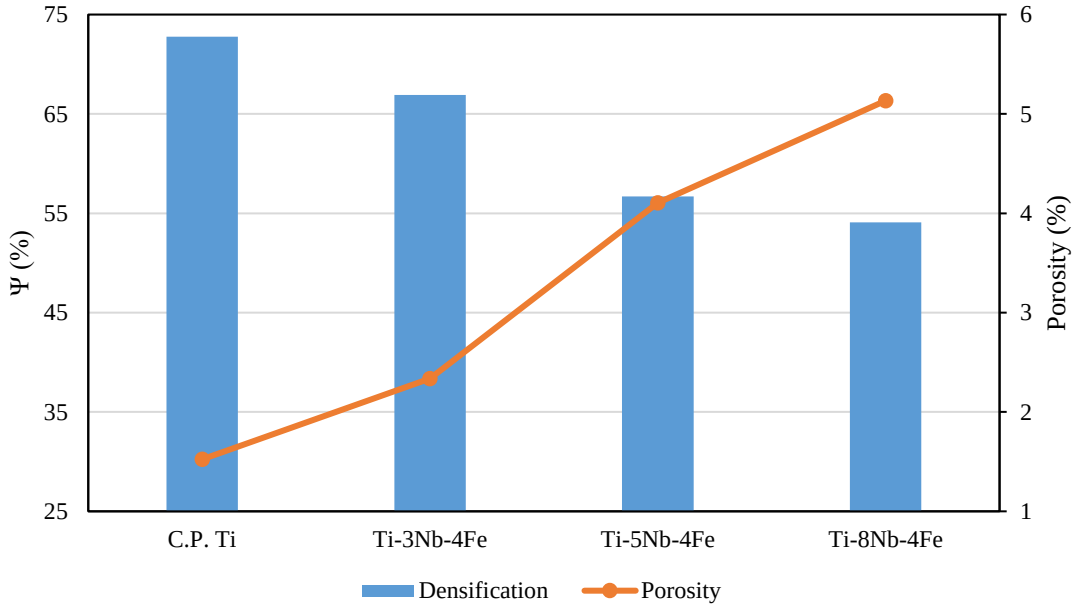

Figure 5.17 Relationship between densification and porosity for Ti-3Nb-4Fe, Ti-5Nb-4Fe and Ti-8Nb-4Fe corresponding to the Ti-4Fe system.

With the addition of alloying elements, the resistance to compaction generally increases which causes a drop in the green density [2]. Especially, the reason for the green density of Ti-8Nb-4Fe to be the lowest can be speculated to be due to the Nb content being above a critical point

of 6 wt%. Lower green density result in lower sintered density despite the presence of Fe powders.

For the Ti-Nb-Fe alloys, the green density range between 90% and 94.5%. The sintered density range between 95% and 98.4%. Ti-9Nb-5Fe and Ti-2Nb-3Fe has the lowest and the highest sintered density, respectively. Of all the systems, only Ti-8Nb and Ti-9Nb system shows an increase in densification. Consequently, sintered density reach around 95%. It is also noticed that highest change in green and sintered density is around 1.5% among all systems.

5.2.2 Phase and microstructural analysis

5.2.2.1 Ti-2Nb system

Figure 5.18 illustrates the XRD spectra of C.P. Ti, Ti-2Nb-3Fe, Ti-2Nb-5Fe and Ti-2Nb-6Fe, the alloys corresponding to the Ti-2Nb system. It is seen that C.P. Ti exhibits only α peaks. Ti-2Nb-3Fe, like C.P. Ti shows predominant α peaks along with the primary β at 39° slightly increasing. The increase in the primary β peak (39°) corresponding to the (1 1 0) is observed with the increase in Fe content. For Ti-2Nb-6Fe, the relative intensity of the 39° peak is the highest. It is worth mentioning that the 39° β peak and primary α peak at 40° seem to have equal relative intensities. In addition, the intensity of the (2 1 1) plane gradually increases and reaches a maximum in Ti-2Nb-6Fe. For Ti-2Nb-6Fe, despite the presence of prominent β peaks, the α peaks are also visible.

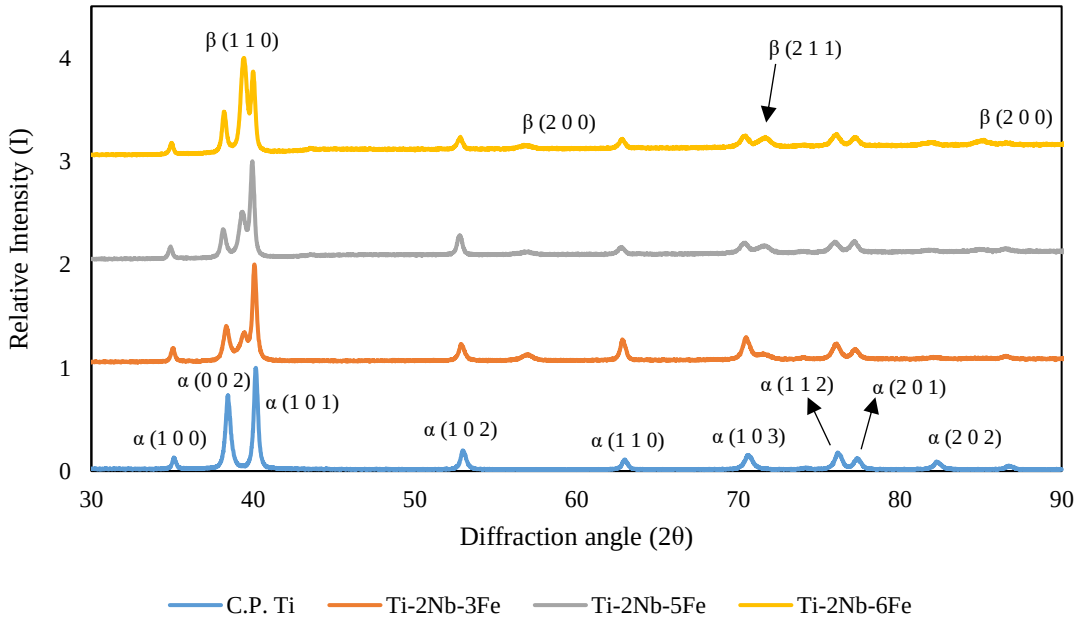

Figure 5.18 XRD spectra of Ti-2Nb-3Fe, Ti-2Nb-5Fe and Ti-2Nb-6Fe alloys corresponding to the Ti-2Nb system.

Figure 5.19 represents the optical and SEM micrographs of Ti-2Nb-3Fe, Ti-2Nb-5Fe and Ti-2Nb-6Fe alloys corresponding to the Ti-2Nb system. It can be seen that Ti-2Nb-3Fe consists of coarse grain boundaries and α+β lamellae. The individual lamellae are clearly shown in Figure 5.19b. The lamellae are observed to get refined with the addition of Fe (β stabiliser) as seen in Figure 5.19(c, d). The thickness and the interlamellar spacing also decreases. The lamellae of Ti-2Nb-6Fe appear to be finest among the alloys from the Ti-2Nb system. Figure 5.19 (e, f) show the fine almost needle like α+β lamellae with a few individual α lamellae originating from the grain boundary. All the alloys are seen to be characterised only by spherical pores that are sparsely distributed. Ti-2Nb-3Fe, Ti-2Nb-5Fe and Ti-2Nb-6Fe are characterised by Widmanstätten microstructures with varying degrees of refinement in the lamellae and interlamellar spacing.

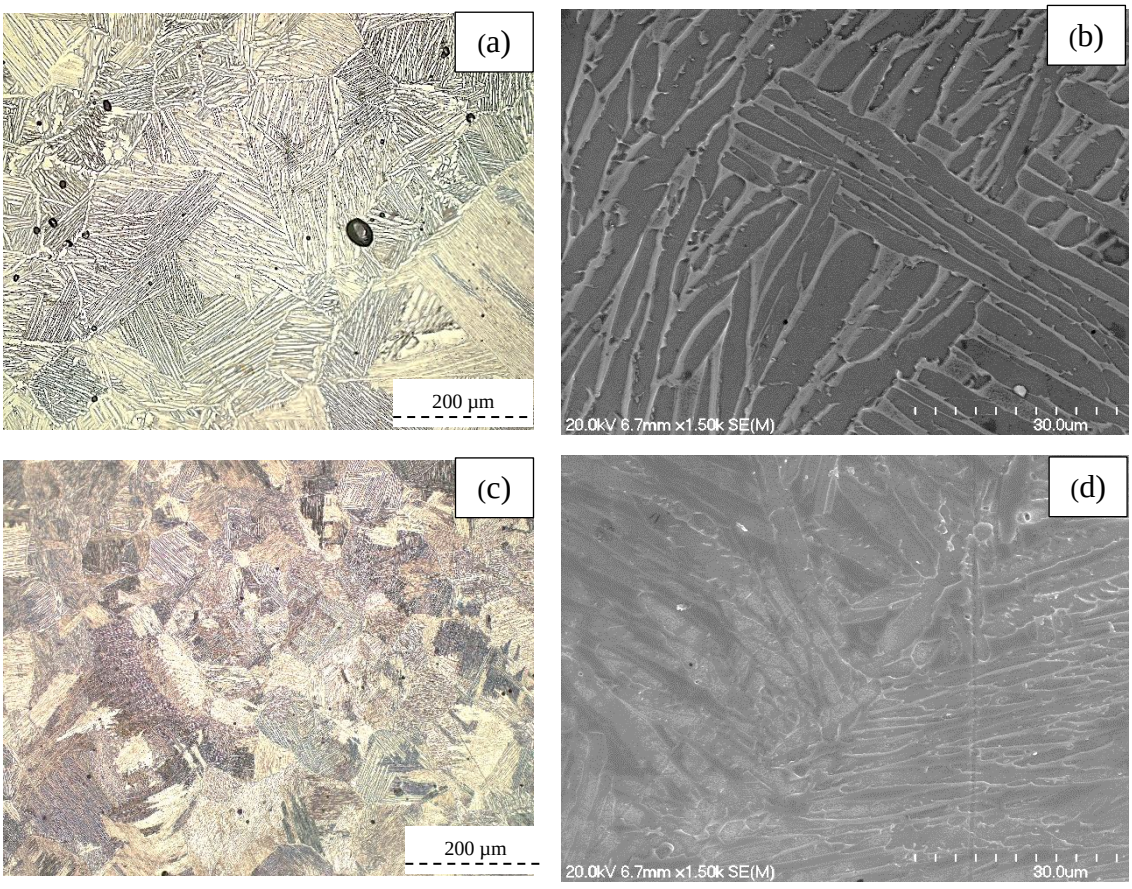

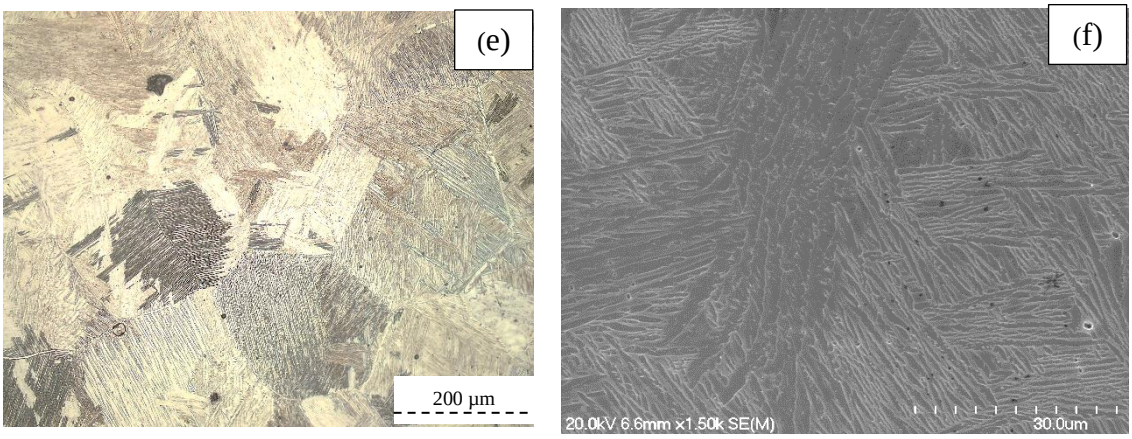

Figure 5.19 Optical and SEM micrographs of (a, b) Ti-2Nb-3Fe, (c, d) Ti-2Nb-5Fe, and (e, f) Ti-2Nb-6Fe alloys corresponding to the Ti-2Nb system.

In general, the alloys corresponding to the Ti-2Nb system is characterised primarily by Widmanstätten microstructures with the interlamellar spacing gradually decreasing with the addition of eutectoid β stabiliser. With the addition of β stabiliser, the β transus drops, thus establishing the β phase by arresting the formation of α phase [86]. Chaves et al. [93] also reported a similar phenomenon due to the addition of isomorphous Nb and eutectoid Fe. The nature of porosity of the alloys from the Ti-2Nb system as seen in **Figure** 5.19 is in line with the density values from Table 5.6. The micrographs are also coherent with the XRD spectra (Figure 5.18) wherein the addition of Fe results in a gradual increase in the relative intensities of the β peaks especially in Ti-2Nb-6Fe.

On the basis of the XRD spectra, the micrographs Ti-2Nb-3Fe and Ti-2Nb-5Fe are regarded as β matrix α+β alloys. While, Ti-2Nb-6Fe due to the presence of a few acicular α lamellae besides the basket-weave structures and dominant primary β peak, is regarded as a near β alloy [80].

5.2.2.2 Ti-5Nb and Ti-6Nb systems

Figure 5.20 represents the XRD spectra of C.P. Ti, Ti-5Nb-3Fe, Ti-5Nb-4Fe, Ti-6Nb-5Fe and Ti-6Nb-6Fe alloys corresponding to the Ti-5Nb and Ti-6Nb systems, respectively. C.P. Ti exhibits only α peaks along the (1 0 0), (0 0 2), (1 0 1), (1 0 2), (1 1 0), (1 0 3), (1 1 2), (2 0 1) and (2 0 2) planes. Ti-5Nb-3Fe and Ti-5Nb-4Fe expresses a trend that is similar to that of the Ti-2Nb system where there is a gradual rise in the β peak intensities due to the addition of β stabiliser. Although the spectra show the presence of β peaks, the α peaks remain domain in both Ti-5Nb-3Fe and Ti-5Nb-4Fe. It is noticed that the relative intensity of the primary β peak in Ti-5Nb-4Fe is greater than Ti-5Nb-4Fe. However, for Ti-6Nb-5Fe the relative intensities of

the primary α and β peaks is seen to be almost equal. But then Ti-6Nb-6Fe exhibits a prominent β peak at 39° with the highest relative intensity.

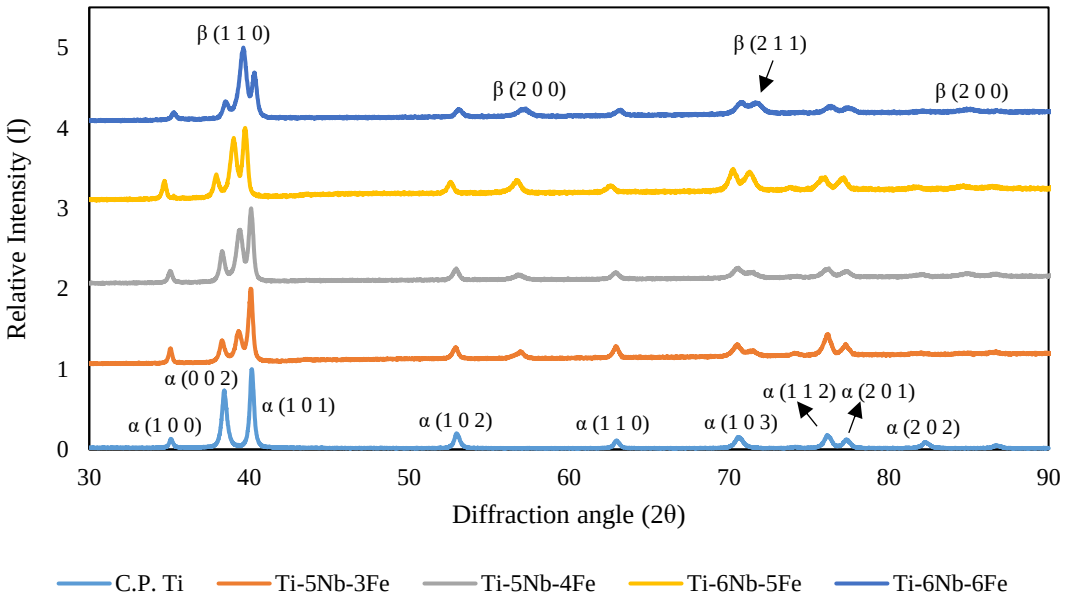

Figure 5.20 XRD spectra of C.P. Ti, Ti-5Nb-3Fe, Ti-5Nb-4Fe, Ti-6Nb-5Fe and Ti-6Nb-6Fe alloys corresponding to the Ti-5Nb and Ti-6Nb systems, respectively.

In general, C.P. Ti exhibits only α peaks while Ti-5Nb-3Fe and Ti-5Nb-4Fe display peaks corresponding to both α and β phases, α peaks remain dominant. The relative intensities of β peaks is seen to rise in Ti-9Nb-5Fe and Ti-9Nb-6Fe shows a dominant β peak where all the α peaks have less relative intensities.

Figure 5.21 represents the optical and SEM micrographs of the alloys corresponding to the Ti-5Nb and Ti-6Nb systems. Both Ti-5Nb-3Fe and Ti-5Nb-4Fe are characterised by basket-weave like microstructure as seen in Figure 5.21(a-d). The transformed β grain boundaries appear to be coarse and notably, the α+β lamellae gets finer with the increase in the Fe content. The alloys are characterised by spherical pores. Figure 5.21**(e-f)** show Ti-6Nb-5Fe and is characterised by Widmanstätten microstructure with very fine α+β lamellae. For Ti-6Nb-6Fe, as seen in Figure 5.21**(g-h)**, the micrograph primarily consists of needle shaped acicular α lamellae and a few regions of Widmanstätten microstructures with the very fine α+β overlapping. It is worth mentioning that the interlamellar spacing for Ti-6Nb-6Fe is noticeably smaller than Ti-6Nb-5Fe. The SEM micrographs clearly illustrates the refinement in the lamellae and the change in the interlamellar spacing in all the alloys from the Ti-5Nb and Ti-6Nb systems.

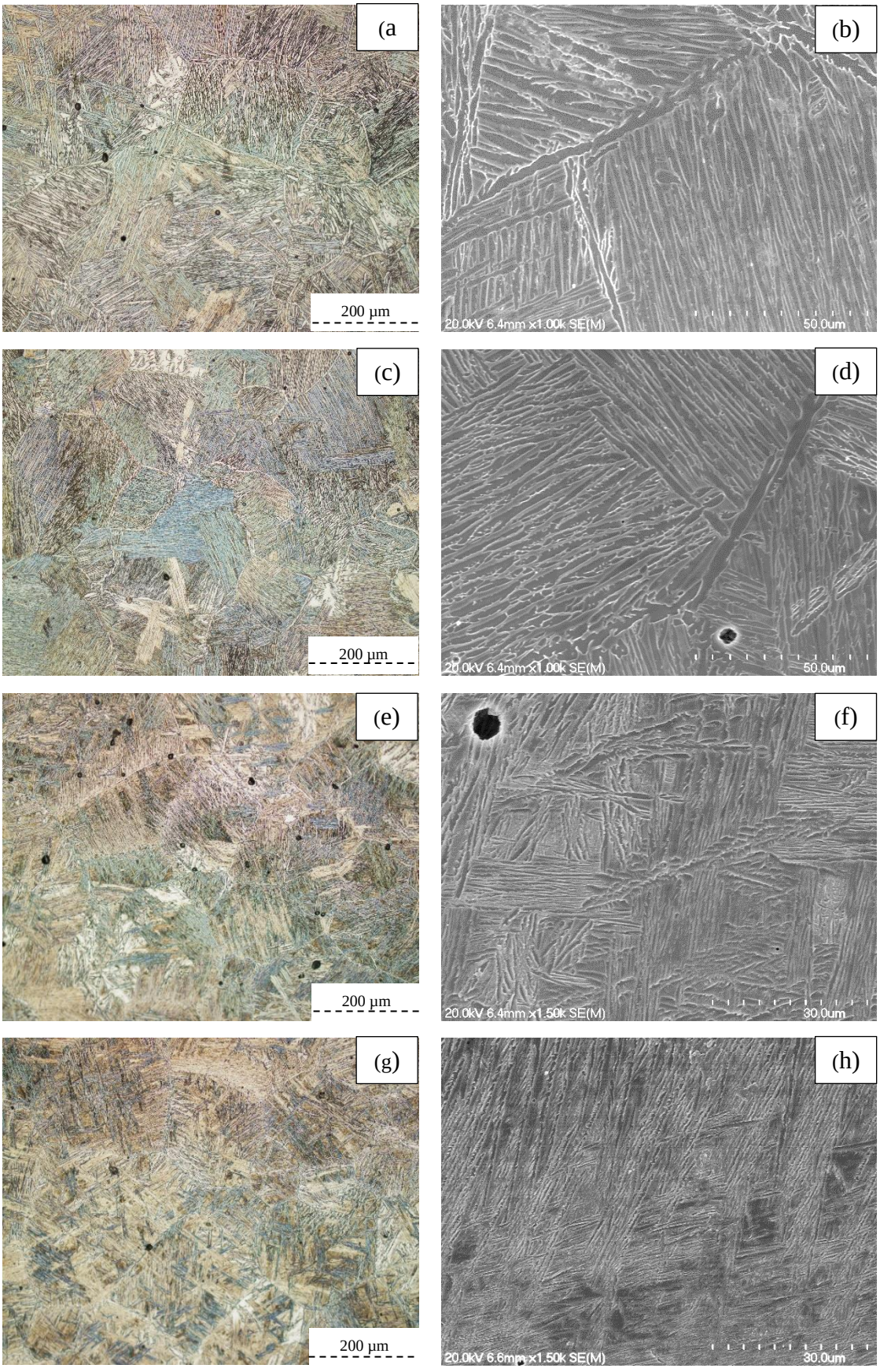

Figure 5.21 Optical and SEM micrographs of (a, b) Ti-5Nb-3Fe (c, d) Ti-5Nb-4Fe (e, f) Ti-6Nb-5Fe (g, h) Ti-6Nb-6Fe alloys corresponding to the Ti-5Nb and Ti-6Nb systems, respectively.

Based on the XRD spectra of the Ti-5Nb systems, there is high α peak intensity besides a few β peaks (Figure 5.20) and the micrographs (Figure 5.21) consists of Widmanstätten microstructures with decreasing interlamellar spacing. Similarly, the XRD spectra and optical micrograph of Ti-5Nb-6Fe and Ti-6Nb-6Fe are concurrent with each other. Further, the sintered density is higher than 96% therefore, all alloys possess spherical pores with varying distribution.

The presence of Widmanstätten microstructures and the proportion of α/β peaks imply that Ti-5Nb-3Fe and Ti-5Nb-4Fe are β matrix α+β alloys. A mixture of both Widmanstätten microstructures and acicular α lamella along with equal proportions of α and β peaks is the reason Ti-6Nb-5Fe is considered as near β alloy. Ti-6Nb-6Fe is predominantly characterised by dominant β peaks suppressing the other α peaks and fine α lamellae and minor proportions of Widmanstätten structures, hence, regarded as metastable β.

5.2.2.3 Ti-8Nb and Ti-9Nb systems

Figure 5.22 shows the XRD spectra of C.P. Ti, Ti-8Nb-2Fe, Ti-8Nb-4Fe, Ti-9Nb-5Fe and Ti-9Nb-6Fe, alloys corresponding to the Ti-8Nb and Ti-9Nb system. Ti-8Nb-2Fe displays a slight increase in the relative intensity of the primary β peak at 39^{o} however, the diffraction pattern primarily consists of prominent α peaks. Ti-8Nb-4Fe and Ti-9Nb-5Fe both show a similar increase in the peak intensities with one exception being the latter significantly suppressing the α peak at 38^{o}. It is noticeable that the primary α and β peaks show a similar relative intensity for both Ti-8Nb-4Fe and Ti-9Nb-5Fe. While the 70^{o}5 peak gradually increases in Ti-9b-5Fe. Ti-9Nb-6Fe has a dominant β peaks at 39^{o}, 57^{o} and 71^{o} corresponding to the (1 1 0), (2 0 0) and (2 1 1) planes, respectively. It is also worth mentioning that Ti-9Nb-6Fe presents the highest proportion of β peaks with minimum α peak intensities. The tiny peak at 43^{o}, indicate the presence of orthorhombic α'' phase. Ehtemam-Haghighi et al. [75] also reports the presence of α'' phase in Ti-7Fe-1Nb, Ti-7Fe-6Nb and Ti-7Fe-9Nb alloys produced by CCLM. It is worth mentioning that with the addition of β phases the intensity of the α'' phases gradually decreased.

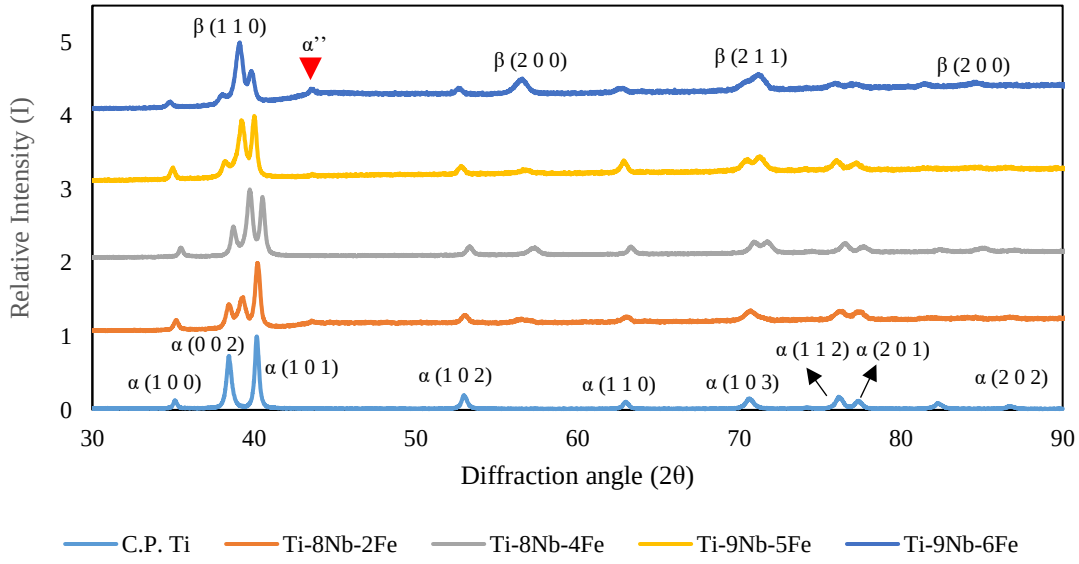

Figure 5.22 XRD spectra of C.P. Ti, Ti-8Nb-2Fe, Ti-8Nb-4Fe, Ti-9Nb-5Fe and Ti-9Nb-6Fe alloys corresponding to the Ti-8Nb and Ti-9Nb systems, respectively.

Figure 5.23 displays representative optical and SEM micrographs of Ti-8Nb-2Fe, Ti-8Nb-4Fe, Ti-9Nb-5Fe, and Ti-9Nb-6Fe corresponding to the Ti-8Nb and Ti-9Nb systems, respectively. All the alloys in this group with the exception to Ti-8Nb-2Fe, are characterised by fine acicular α lamellae. Ti-8Nb-2Fe is characterised by Widmanstätten microstructure with coarse transformed β grain boundaries and overlapping α+β lamellae. In Ti-8Nb-4Fe, the thickness of the α+β lamellae reduces as the proportion of β phase increases (Figure 5.23d). It is seen that the distribution of porosity in Ti-8Nb-4Fe is higher than that of Ti-8Nb-2Fe. Ti-9Nb-5Fe exhibits basket-weave microstructure and fine needle like acicular α lamellae emerging from the grain boundaries and Ti-9Nb-6Fe, as seen in Figure 5.23(e-h) is characterised by equiaxed β grains and large regions of fine needle like acicular α lamellae. Comparing Ti-9Nb-5Fe and Ti-9Nb-6Fe, the proportion of the acicular α is much less in the latter.

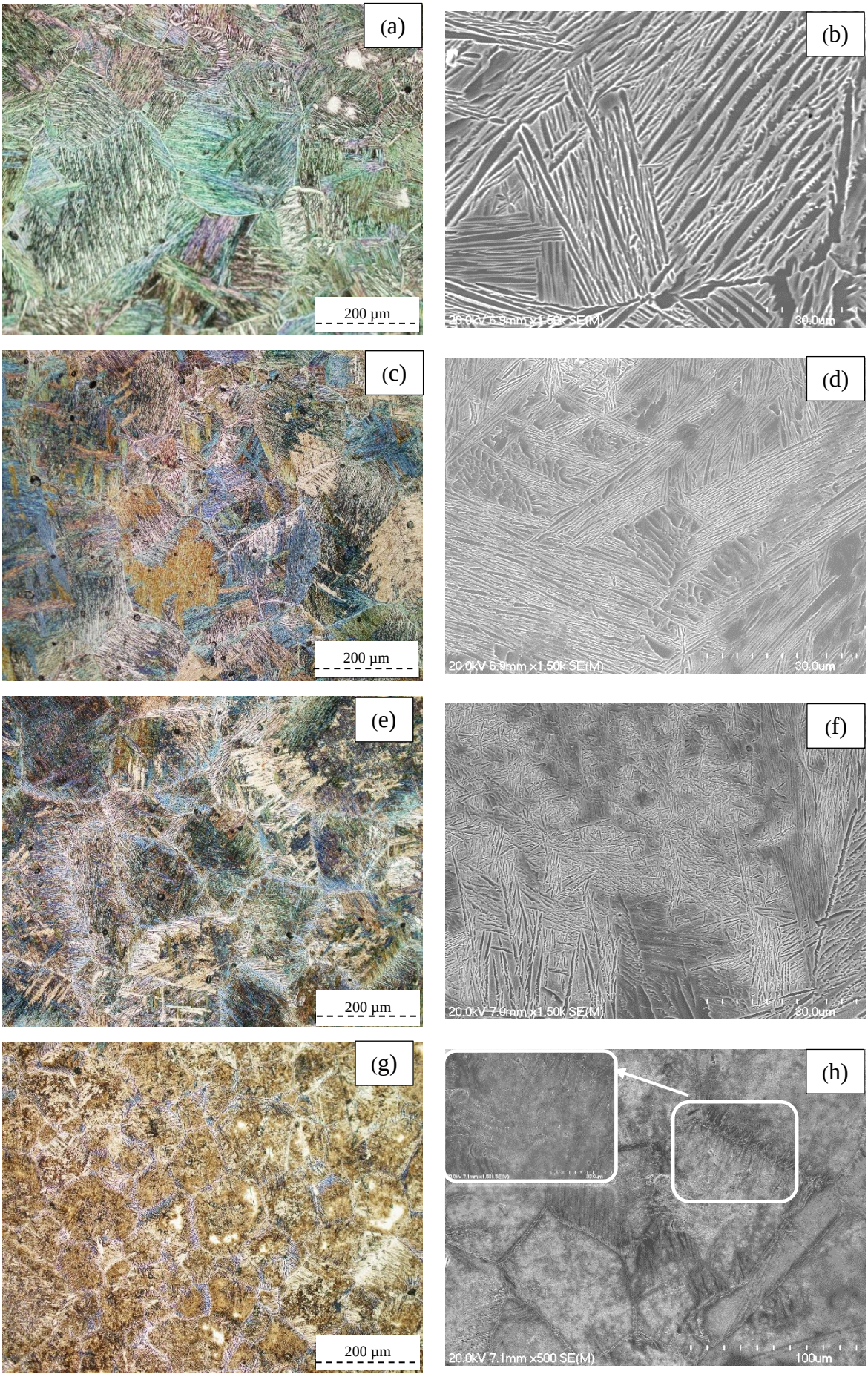

Figure 5.23 Optical and SEM micrographs of (a, b) Ti-8Nb-2Fe, (c, d) Ti-8Nb-4Fe, (e, f) Ti-9Nb-5Fe and (g, h) Ti-9Nb-6Fe alloys corresponding to the Ti-8Nb and Ti-9Nb systems, respectively.

The micrograph of Ti-8Nb-2Fe as seen in Figure 5.23(a, b) is in accordance with the XRD spectra (Figure 5.22) i.e. the addition of β stabilisers, causes a slight rise in the (1 1 0) plane resulting in a biphasic microstructure. With further increase in Fe, the β peaks gradually increases which results in the refinement of the lamellae of Ti-8Nb-4Fe. The XRD spectra of Ti-9Nb-5Fe is characterised by prominent peaks corresponding to both α and β phases and is reflected on the micrograph where there is a mixture of Widmanstätten structures and individual acicular α lamellae. Ti-9Nb-6Fe shows a diffraction pattern consisting of tiny proportion of α'' phase, dominant β peaks where all peaks corresponding to α are suppressed. Similarly, the micrographs of Ti-9Nb-6Fe as seen in Figure 5.23(g, h) shows primary equiaxed β grains with tiny proportions of individual α lamellae mostly along the grain boundaries.

Based on the above discussion, it is concluded that Ti-8Nb-2Fe belong to the β matrix α+β category and Ti-8Nb-4Fe as near β alloys. Ti-9Nb-5Fe and Ti-9Nb-6Fe are regarded as metastable β.

5.2.2.4 Ti-4Fe system

Figure 5.24 shows the XRD spectra of C.P. Ti, Ti-3Nb-4Fe, Ti-5Nb-4Fe and Ti-8Nb-4Fe corresponding to the Ti-4Fe system respectively. C.P. Ti exhibits only α peaks along the (1 0 0), (0 0 2), (1 0 1), (1 0 2), (1 1 0), (1 0 3), (1 1 2), (2 0 1) and (2 0 2) planes. Ti-3Nb-4Fe shows a small β peak at 39^{o} and 70^{o}5 corresponding to (1 1 0) and (2 1 1) planes. Otherwise, the spectra is completely characterised by dominant α peaks. For Ti-5Nb-4Fe, the primary β peak shows a higher relative intensity when compared to Ti-3Nb-4Fe, due to the increase in Nb content (β stabiliser). The 57^{o} peaks actually rises up in Ti-5Nb-4Fe. With further addition of Nb, the primary β peak becomes the dominant peak and the relative intensities of the other α peaks remain almost the same.

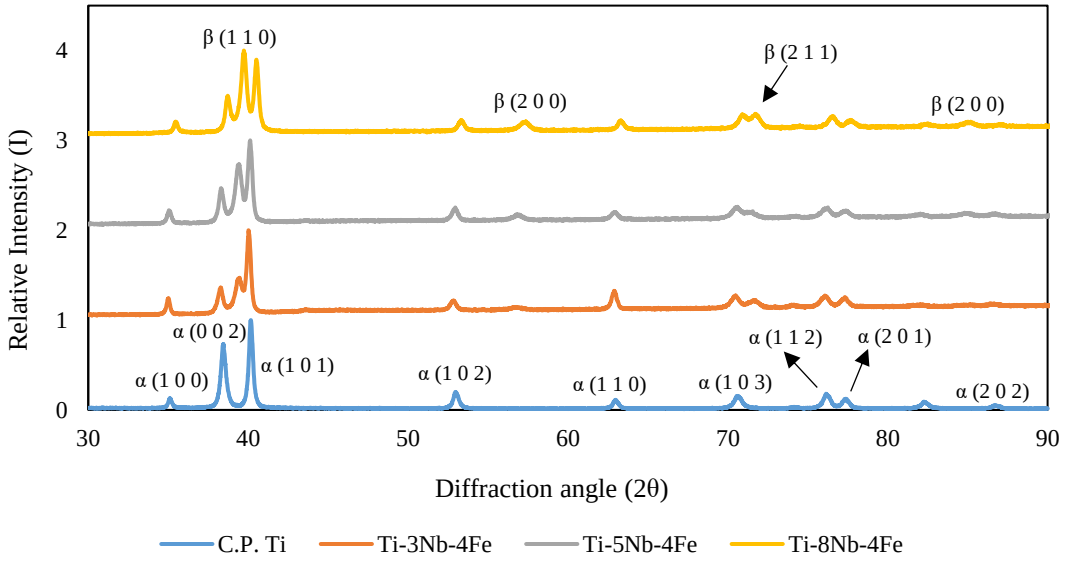

Figure 5.24 XRD spectra of Ti-3Nb-4Fe, Ti-5Nb-4Fe and Ti-8Nb-4Fe corresponding to the Ti-4Fe system.

In general, C.P. Ti exhibits only α peaks and with the addition of β stabilisers, the relative intensities of peaks corresponding to the β phase gradually increase however the α peaks remain dominant. Ti-8Nb-4Fe shows the highest β peak intensity at 39°.

Figure 5.25 represents the optical and SEM micrographs of Ti-3Nb-4Fe (a, b), Ti-5Nb-4Fe (c, d), Ti-8Nb-4Fe (e, f) corresponding to the Ti-4Fe system. It is seen that Ti-3Nb-4Fe consists of coarse overlapping α+β lamellae with coarse grain boundaries. The thickness of the lamellae is clearly shown in Figure 5.25b. As the Nb content is increased, the thickness of the lamellae reduces due to refinement. However, the microstructure is characterised by overlapping α+β lamellae. The increase in Nb content also causes the increase in porosity. Ti-5Nb-4Fe consists of closed spherical pores and the number of pores is high when compared with Ti-3Nb-4Fe. Ti-8Nb-4Fe is characterised by very fine α+β lamellae. The interlamellar spacing is seen to have decreased when compared to Ti-3Nb-4Fe and Ti-5Nb-4Fe. Also, due to high Nb content, the size and distribution of pores is the highest. Although most of the pores are spherical, a few elongated pores are also visible. Comparing the Ti-4Fe system with the other systems, it is seen that the effect of Nb in stabilising the β phase is relatively less when compared to Fe.

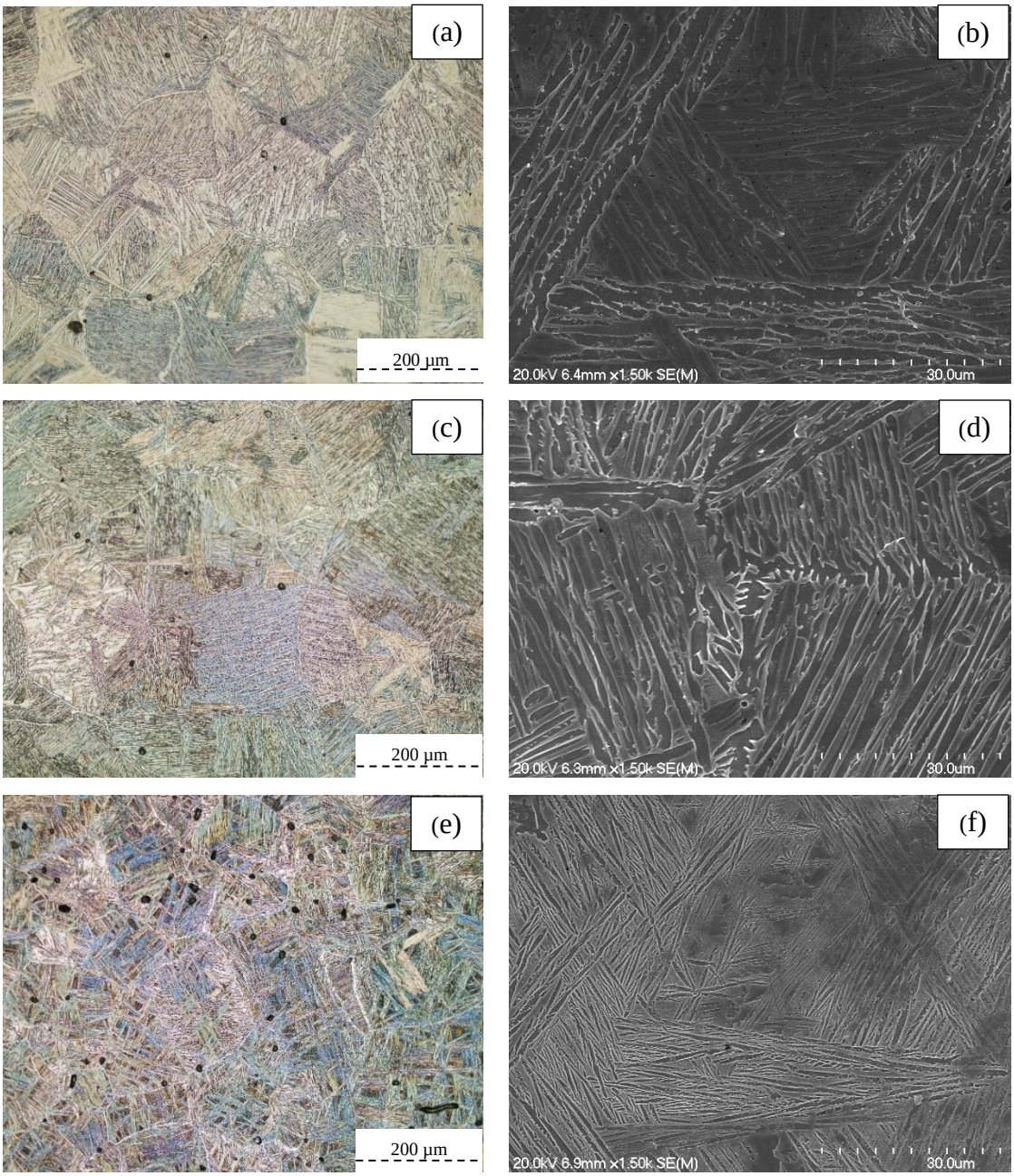

Figure 5.25 Optical and SEM micrographs of (a, b) Ti-3Nb-4Fe (c, d) Ti-5Nb-4Fe (e, f) Ti-8Nb-4Fe corresponding to the Ti-4Fe system.

With the increase in Nb content, Ti-3Nb-4Fe, Ti-5Nb-4Fe and Ti-8Nb-4Fe are characterised by Widmanstätten microstructures with different interlamellar spacing which is in line with the relative intensities of the corresponding alloys as shown in the XRD spectra (Figure 5.24). For Ti-8Nb-4Fe, although it exhibits prominent β peaks the relative intensities of both α and β peak are comparable and micrograph consists of very fine overlapping α+β lamellae.

Hence, Ti-3Nb-4Fe and Ti-5Nb-4Fe belong to the β matrix α+β alloy, while Ti-8Nb-4Fe is regarded to be near β due to the presence of fine Widmanstatten microstructures and dominant β peaks amidst the other α peaks.

For the Ti-Nb-Fe alloys, with the addition of Nb and Fe, the β peaks gradually increases among Ti-2Nb-6Fe, Ti-6Nb-5Fe, Ti-8Nb-4Fe which show equal proportion of α and β peaks and their micrographs are characterised by very fine α+β lamellae. Ti-6Nb-6Fe, Ti-9Nb-5Fe and Ti-9Nb-6Fe exhibit dominant β peaks with minimal α peaks. A tiny peak corresponding to an orthorhombic α'' phase is observed in Ti-9Nb-6Fe. The micrographs of these alloys consist of equiaxed β grains with needle shaped individual α lamellae. Analogous to the XRD spectra of Ti-2Nb-3Fe, Ti-2Nb-5Fe, Ti-3Nb-4Fe, Ti-5Nb-3Fe, Ti-5Nb-4Fe and Ti-8Nb-2Fe show Widmanstätten microstructures with differing thickness and interlamellar spacing.

Based on the XRD spectra and micrographs of Ti-Nb-Fe alloys, Ti-2Nb-3Fe, Ti-2Nb-5Fe, Ti-3Nb-4Fe, Ti-5Nb-3Fe, Ti-5Nb-4Fe, Ti-8Nb-2Fe belong to the β matrix α+β alloys. Ti-2Nb-6Fe, Ti-6Nb-5Fe and Ti-8Nb-4Fe are near β alloys and Ti-6Nb-6Fe, Ti-9Nb-5Fe and Ti-9Nb-6Fe belong to the metastable β alloy.

It is worth mentioning that there is a discrepancy between the MoE values and the above classification. This can be attributed to the choice of equation (Equation 4-1) to calculate the MoE values.

5.2.3 Mechanical properties

5.2.3.1 Ti-2Nb system

Table 5.10 shows the mechanical properties of C.P. Ti, Ti-2Nb-3Fe, Ti-2Nb-5Fe and Ti-2Nb-6Fe alloys corresponding to the Ti-2Nb system. It is seen that C.P. Ti has the lowest yield and ultimate tensile strength of 453 and 588 MPa. However, it exhibits a higher elongation to failure of 10.3%. Among the other alloys, Ti-2Nb-3Fe shows the least yield and ultimate tensile strength (608 MPa and 743 MPa, respectively) and the highest elongation to failure (11%) which is comparable with C.P. Ti. The Rockwell hardness range between 63 – 68 HRA for Ti-2Nb-3Fe and Ti-2Nb-6Fe, respectively.

Table 5.10 Mechanical properties of C.P. Ti, Ti-2Nb-3Fe, Ti-2Nb-5Fe and Ti-2Nb-6Fe alloys corresponding to the Ti-2Nb system.

System	Material	Alloying elements (wt%)	YS (MPa)	UTS (MPa)	Elongation (%)	Hardness (HRA)
	C.P. Ti	0	453 ± 38	588 ± 42	10.3 ± 2.2	58.4 ± 2.0
Ti-2Nb	Ti-2Nb-3Fe	5	608 ± 14	743 ± 23	11.0 ± 2.0	63.2 ± 1.0
	Ti-2Nb-5Fe	7	708 ± 15	828 ± 17	4.6 ± 1.5	66.5 ± 0.6
	Ti-2Nb-6Fe	8	782 ± 18	822 ± 50	1.6 ± 0.5	67.9 ± 0.4

Figure 5.26 shows the relationship between the strength and ductility of C.P. Ti, Ti-2Nb-3Fe, Ti-2Nb-5Fe and Ti-2Nb-6Fe alloys corresponding to the Ti-2Nb system. It is seen that with the addition of Fe the strength gradually increases at the expense of ductility. The addition of Fe causes solid solution strengthening where the substitutional Fe atoms impede the movement of dislocation requiring more load to propagate [85; 86]. As a result, the strength increases. Further, the addition of β stabilisers such as Fe, tend to reduce the β transus temperature thereby establishing the β phase [87]. This results in the refinement of the grains and according to Hall Petch's relationship, the finer grains possess high strength as compared to coarser grains [88]. The movement of the dislocations obstructed by the substitutional Fe atoms leads to lesser elongation to failure. It can be seen that as the wt% of Fe increases the elongation to failure gradually drops.

Despite the slight decrease in the sintered density, the tensile strength gradually increases with the addition of alloying elements. The refinement of lamellae due to the addition of Fe, can be seen in Figure 5.25.

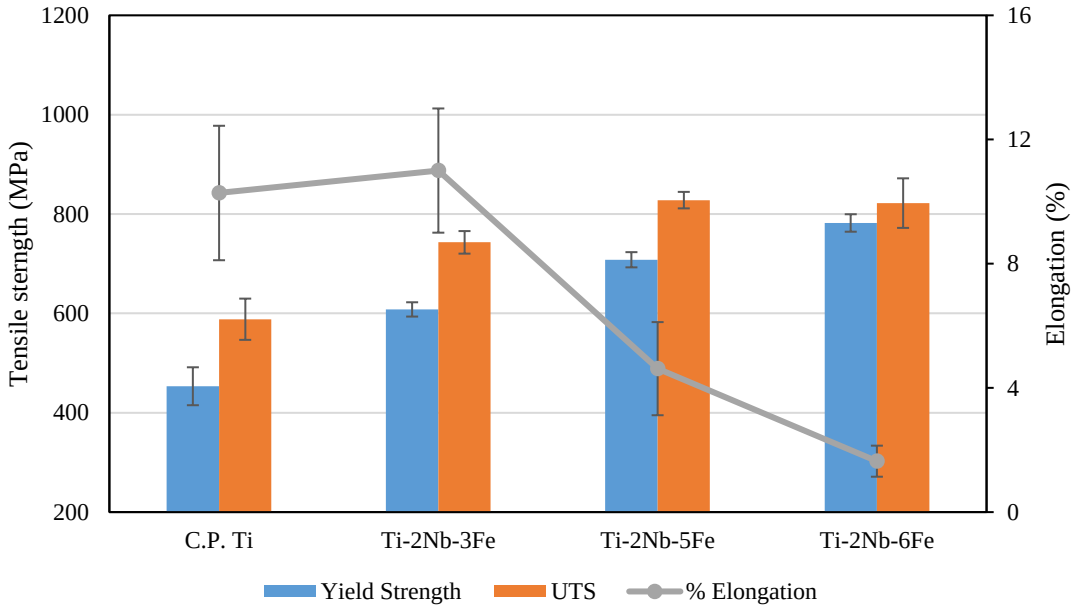

Figure 5.26 Relationship between the strength and ductility of C.P. Ti, Ti-2Nb-3Fe, Ti-2Nb-5Fe and Ti-2Nb-6Fe alloys corresponding to the Ti-2Nb system.

Figure 5.27 represents the Rockwell hardness vs alloying elements of C.P. Ti, Ti-2Nb-3Fe, Ti-2Nb-5Fe and Ti-2Nb-6Fe alloys corresponding to the Ti-2Nb system. It is seen that the hardness values increase with the addition of Fe. It is notable that C.P. Ti has the lowest hardness value. In line with the tensile strength, hardness values also increase as the substitutional alloying elements tend to increase the resistance to indentation.

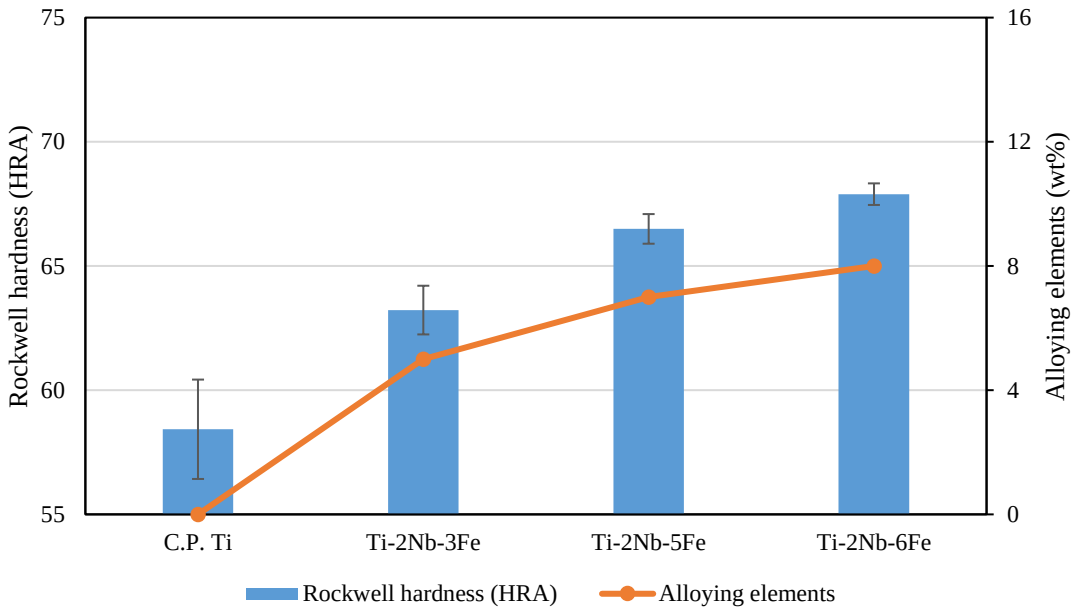

Figure 5.27 Rockwell Hardness vs Alloying elements of C.P. Ti, Ti-2Nb-3Fe, Ti-2Nb-5Fe and Ti-2Nb-6Fe alloys corresponding to the Ti-2Nb system.

In general, for the Ti-2Nb system, the addition of Fe, causes the β peaks to gradually increase and the causes the α+β lamellae to refine to stabilising of the β phase. Further the solid solution effect Fe causes the strength to increase at the cost of ductility. However, Ti-2Nb-3Fe and Ti-3Nb-5Fe shows a good combination of strength and ductility which is indicative that both these alloys belong to the β matrix α+β alloy and Ti-2Nb-6Fe, due to its very fine lamellae is characterised as a near β alloy.

5.2.3.2 Ti-5Nb and Ti-6Nb systems

Table 5.11 displays the mechanical properties of C.P. Ti, Ti-5Nb-3Fe, Ti-5Nb-4Fe, Ti-6Nb-5Fe and Ti-6Nb-6Fe alloys corresponding to the Ti-5Nb and Ti-6Nb systems, respectively. Among other alloys, Ti-5Nb-3Fe has the lowest yield and ultimate tensile strength (685 MPa and 783 MPa respectively). Ti-6Nb-6Fe possesses the highest yield and ultimate tensile strength (983 MPa and 1023 MPa respectively). Conversely, Ti-5Nb-3Fe displays the highest elongation to failure and vice versa. The Rockwell hardness values of the alloy ranges between 65-69 HRA. It is noticed that the hardness follows a similar as ultimate tensile strength.

Table 5.11 Mechanical properties of C.P. Ti, Ti-5Nb-3Fe, Ti-5Nb-4Fe, Ti-6Nb-5Fe and Ti-6Nb-6Fe alloys corresponding to the Ti-5Nb and Ti-6Nb systems, respectively.

System	Material	Alloying elements (wt%)	YS (MPa)	UTS (MPa)	Elongation (%)	Hardness (HRA)
	C.P. Ti	0	453.3 ± 38.2	588.2 ± 41.5	10.3 ± 2.2	58.4 ± 2.0
Ti-5Nb	Ti-5Nb-3Fe	8	685 ± 13.2	783 ± 7.4	6.0 ± 1.5	65.1 ± 0.4
	Ti-5Nb-4Fe	9	753 ± 5.8	834 ± 4.9	4.4 ± 1.6	66.4 ± 0.7
Ti-6Nb	Ti-6Nb-5Fe	11	832 ± 12.6	909 ± 20.3	3.4 ± 0.3	67.6 ± 0.7
	Ti-6Nb-6Fe	12	983 ± 25.2	1023 ± 32.7	2.0 ±0.6	69.2 ± 0.6

Figure 5.28 shows the relationship between the strength and ductility of C.P. Ti, Ti-5Nb-3Fe, Ti-5Nb-4Fe, Ti-6Nb-5Fe and Ti-6Nb-6Fe alloys corresponding to the Ti-5Nb and Ti-6Nb systems, respectively. It is seen that with the addition of alloying elements, the yield and ultimate tensile strength of the alloys gradually increase. Considering the standard error associated with the elongation to failure values of Ti-5Nb-3Fe and Ti-5Nb-4Fe, both the alloys possess the comparable elongation strain to failure values. However, the elongation to failure decreases for Ti-6Nb-6Fe.

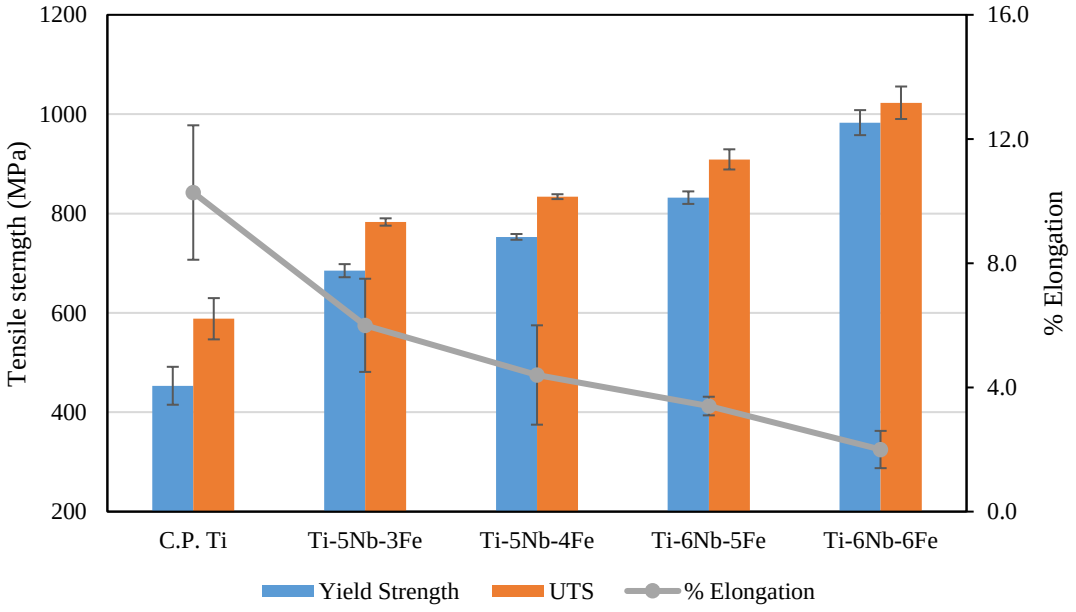

Figure 5.28 Relationship between the strength and ductility of C.P. Ti, Ti-5Nb-3Fe, Ti-5Nb-4Fe, Ti-6Nb-5Fe and Ti-6Nb-6Fe alloys corresponding to the Ti-5Nb and Ti-6Nb systems, respectively.

The reason for the increase in strength with the addition of Nb and Fe is the same as explained in 5.2.3.1. the Addition of alloying elements results in solid solution strengthening due to the substitutional alloying elements obstructing the movement of dislocations. Further, the increase in β stabilisers, reduces the β transus thereby stabilising the β phase. As a result, refinement

occurs and the interlamellar spacing decreases. According to Hall Petch's relationship, finer grains tend to possess high tensile strength [84-86].

Figure 5.29 shows the Rockwell Hardness vs alloying elements of C.P. Ti, Ti-5Nb-3Fe, Ti-5Nb-4Fe and Ti-6Nb-5Fe and Ti-6Nb-6Fe alloys corresponding to the Ti-5Nb and Ti-6Nb systems, respectively. C.P. Ti has the lowest hardness among them all. As discussed above, with the increase in Nb and Fe wt%, the substitutional alloying elements increase the resistance to indentation which in turn makes the alloys harder [69] . Therefore, it is implied that hardness is largely governed by the microstructure rather than porosity.

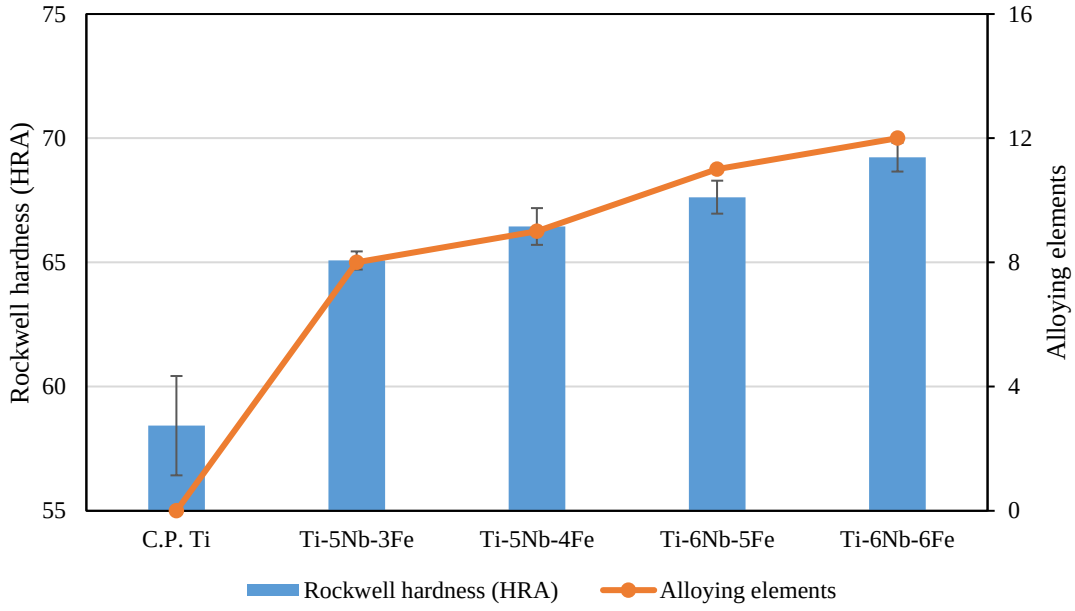

Figure 5.29 Rockwell Hardness vs alloying elements of C.P. Ti, Ti-5Nb-3Fe, Ti-5Nb-4Fe and Ti-6Nb-5Fe and Ti-6Nb-6Fe alloys corresponding to the Ti-5Nb and Ti-6Nb systems, respectively.

5.2.3.3 Ti-8Nb and Ti-9Nb systems

Table 5.12 shows the mechanical properties of C.P. Ti, Ti-8Nb-2Fe, Ti-8Nb-4Fe, Ti-9Nb-5Fe and Ti-9Nb-6Fe alloys corresponding to the Ti-8Nb and Ti-9Nb systems, respectively. C.P. Ti has the lowest yield and ultimate tensile strength of 453 and 588 MPa. It exhibits the highest elongation to failure of 10.3%. Among the other alloys, Ti-8Nb-2Fe has the lowest yield and ultimate tensile strength. Ti-9Nb-6Fe possesses the highest yield and ultimate tensile strength. Conversely, the former has the highest elongation to failure and is comparable with that of C.P. Ti. The hardness values range between 64 - 69.4 HRA following a similar trend as the tensile strength.

Table 5.12 Mechanical properties of C.P. Ti, Ti-8Nb-2Fe, Ti-8Nb-4Fe, Ti-9Nb-5Fe and Ti-9Nb-6Fe alloys corresponding to the Ti-8Nb and Ti-9Nb systems, respectively.

System	Material	Alloying elements (wt%)	YS (MPa)	UTS (MPa)	Elongation (%)	Hardness (HRA)
	C.P. Ti	0	453.3 ± 38.2	588.2 ± 41.5	10.3 ± 2.2	58.4 ± 2.0
Ti-8Nb	Ti-8Nb-2Fe	10	673 ± 11.5	775 ± 3.1	10.0 ± 2.0	63.9 ± 0.7
	Ti-8Nb-4Fe	12	797 ± 15.3	891 ± 28.9	6.2 ± 1.8	65 ± 0.3
Ti-9Nb	Ti-9Nb-5Fe	14	957 ± 16.1	1033 ± 13.4	5.0 ± 1.5	67.6 ± 0.3
	Ti-9Nb-6Fe	15	1059 ± 15.4	1071 ± 18.5	1.7 ± 0.4	69.4 ± 0.4

Figure 5.30 shows the relationship between the strength and ductility of C.P. Ti, Ti-8Nb-2Fe, Ti-8Nb-4Fe, Ti-9Nb-Fe and Ti-9Nb-6Fe corresponding to theTi-8Nb and Ti-9Nb systems, respectively. It is seen that the strength increases with the addition of Fe and with the increase in strength the elongation to failure gradually drops.

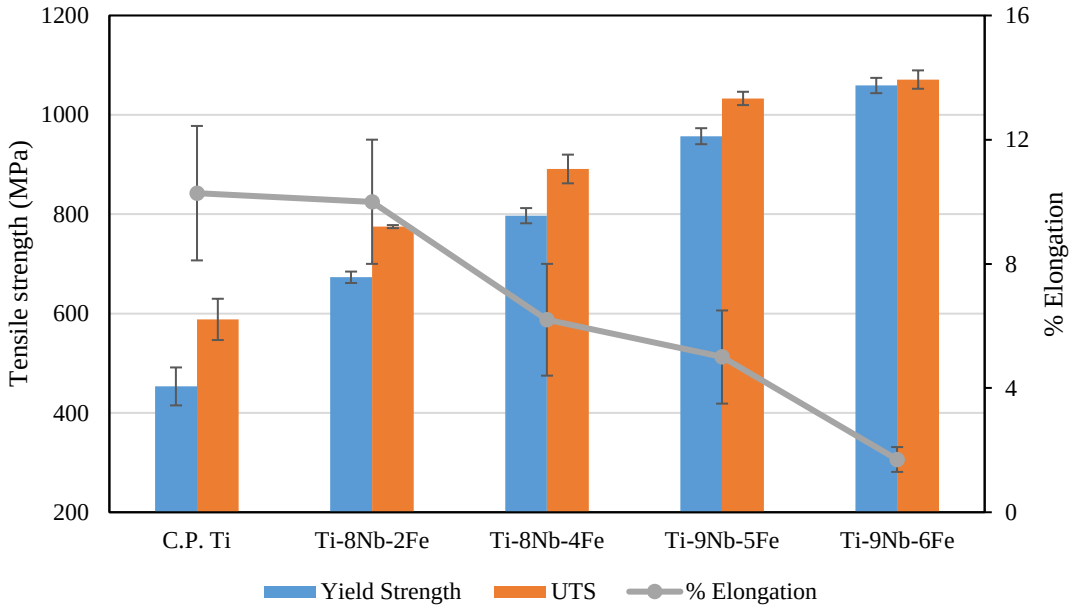

Figure 5.30 Relationship between the strength and ductility of C.P. Ti, Ti-8Nb-2Fe, Ti-8Nb-4Fe, Ti-9Nb-Fe and Ti-9Nb-6Fe corresponding to theTi-8Nb and Ti-9Nb systems, respectively.

The addition of substitutional alloying elements increases the strength by solid solution strengthening. As explained in the previous chapters, by impeding the movement of dislocation the higher load is required in order to mobilize the dislocations leading to failure. Movement of dislocation causes plastic deformation a.k.a elongation and the impediment of the same reduces the elongation to failure values [84; 86].

Figure 5.31 displays the relationship between Rockwell Hardness and alloying elements of C.P. Ti, Ti-8Nb-2Fe, Ti-8Nb-4Fe and Ti-9Nb-5Fe and Ti-9Nb-6Fe alloys corresponding to the Ti-8Nb and Ti-9Nb systems, respectively. It is seen that with the addition of alloying elements, the hardness values increase. Similar to the trend noticed in Figure 5.30, the addition of alloying elements increases the resistance to indentation by hindering plastic deformation which in turn increases the hardness.

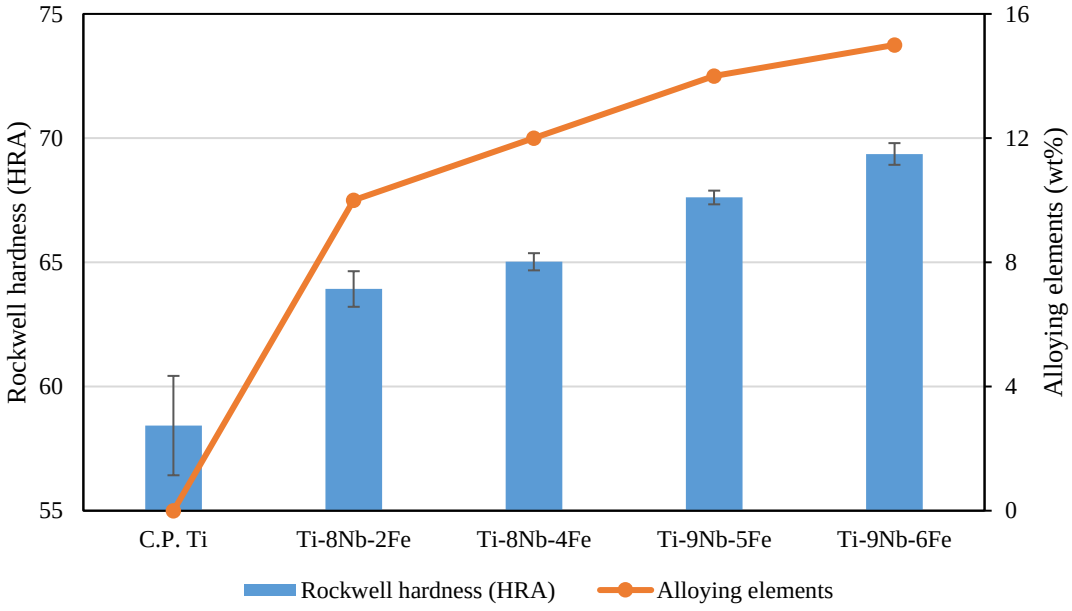

Figure 5.31 Rockwell Hardness vs alloying elements of C.P. Ti, Ti-8Nb-2Fe, Ti-8Nb-4Fe, Ti-9Nb-5Fe and Ti-9Nb-6Fe alloys corresponding to the Ti-8Nb and Ti-9Nb systems, respectively.

5.2.3.4 Ti-4Fe system

Table 5.13 shows the mechanical properties of C.P. Ti, Ti-3Nb-4Fe, Ti-5Nb-4Fe and Ti-8Nb-4Fe alloys corresponding to the Ti-4Fe system. Ti-3Nb-4Fe and Ti-5Nb-4Fe both have the same tensile strength. Although the latter shows a higher standard deviation. Ti-8Nb-4Fe possesses the highest ultimate tensile strength (891 MPa). Similarly, the elongation to failure values of all three alloys show a minimal variation among which Ti-8Nb-4Fe has the highest value (6.2%). All the alloys show similar hardness values.

Table 5.13 Mechanical properties of C.P. Ti, Ti-3Nb-4Fe, Ti-5Nb-4Fe, Ti-8Nb-4Fe alloys corresponding to the Ti-4Fe system.

System	Material	Alloying elements (wt%)	YS (MPa)	UTS(MPa)	% Elongation	Hardness (HRA)
	C.P. Ti	0	453.3 ± 38.2	588.2 ± 41.5	10.3 ± 2.2	58.4 ± 2.0
Ti-4Fe	Ti-3Nb-4Fe	7	727 ± 11.5	834 ± 17.3	5.0 ± 1.1	66.6 ± 0.6
	Ti-5Nb-4Fe	9	753 ± 5.8	834 ± 4.9	4.4 ± 1.6	66.4 ± 0.7
	Ti-8Nb-4Fe	12	797 ± 15.3	891 ± 28.9	6.2 ± 1.8	65 ± 0.3

Figure 5.32 displays the relationship between the strength and ductility of C.P. Ti, Ti-3Nb-4Fe, Ti-5Nb-4Fe, Ti-8Nb-4Fe alloys corresponding to the Ti-4Fe system. Despite the addition of Nb, the strength and ductility of Ti-3Nb-4Fe and Ti-5Nb-4Fe remains the same. In general, addition of Nb helps to improve ductility [70]. Further, from the Figure 5.24, with the addition of Nb, the proportion of β phase increases thereby increasing the ductility. The reason for the slight drop in the ductility can be majorly attributed to porosity.

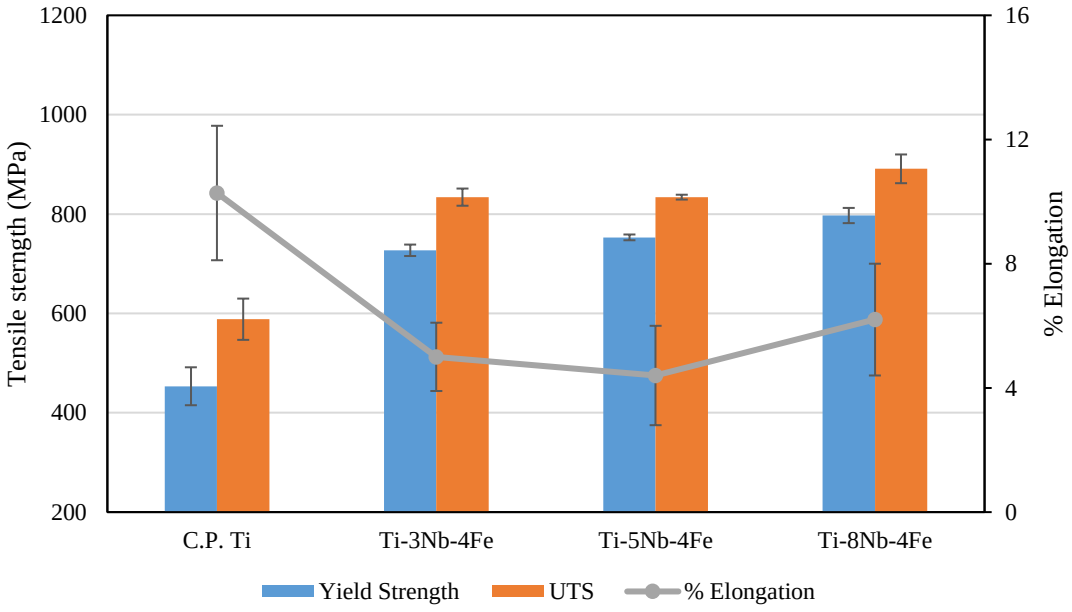

Figure 5.32 Relationship between the strength and ductility of C.P. Ti, Ti-3Nb-4Fe, Ti-5Nb-4Fe, Ti-8Nb-4Fe alloys corresponding to the Ti-4Fe system.

With the addition of Nb, the proportion of β proportion increases and is expected to increase the ductility. However, due to the low sintered density of Ti-8Nb-4Fe (Table 5.9), there is a huge standard deviation in the elongation strain. Further, if not for the pores, the ductility is expected to increase further. Otherwise, Ti-3Nb-4Fe and Ti-5Nb-4Fe possess similar strength while the latter might have better ductility if not for the pores. Although the sintered density of Ti-5Nb-4Fe is higher than 96%, the distribution of the pores causes the difference in ductility.

Figure 5.33 shows the Rockwell hardness vs alloying elements trend for C.P. Ti, Ti-3Nb-4Fe, Ti-5Nb-4Fe and Ti-8Nb-4Fe alloys corresponding to the Ti-4Fe system. It is seen that with the addition of Nb, there is a gradual decline in the hardness values. It can be noticed that the hardness values a similar trend as the sintered density (Table 5.9). An increase in porosity reduces the resistance the alloy offers to indentation. Hence it is concluded that hardness values of the alloys from the Ti-4Fe system is predominantly affected by porosity.

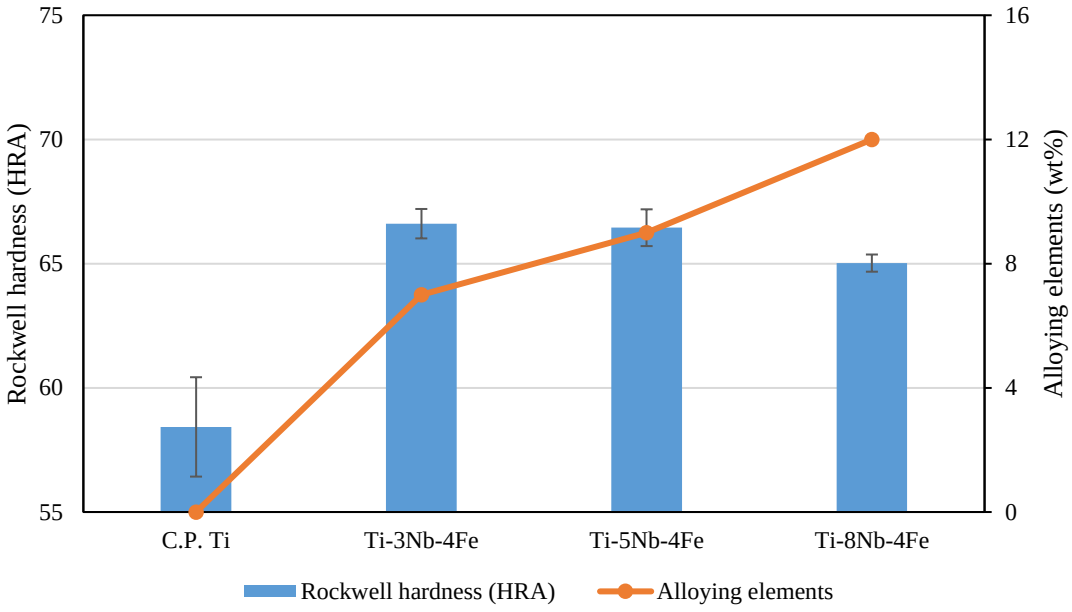

Figure 5.33 Rockwell hardness vs alloying elements of C.P. Ti, Ti-3Nb-4Fe, Ti-5Nb-4Fe and Ti-8Nb-4Fe alloys corresponding to the Ti-4Fe system.

Among the Ti-Nb-Fe alloys, Ti-2Nb-3Fe and Ti-9Nb-6Fe show the lowest and highest ultimate tensile strength of 743 MPa and 1071 MPa, respectively. On the contrary, Ti-2Nb-3Fe exhibits the highest elongation to failure (11 %) which is almost comparable to C.P. Ti (10.3%). Similar to tensile strength, Ti-2Nb-3Fe and Ti-9Nb-6Fe possess the lowest and highest hardness. The presence of orthorhombic α'' (Figure 5.22) also partly contributes to the hardness in addition to the microstructure. The addition of alloying elements results in solid solution and grain boundary strengthening causing a rise in strength and a corresponding deterioration of ductility [84]. The effect of refinement due to the addition of Fe and Nb is evident from the XRD and micrographs. Observing the Ti-4Fe system, contrary to the other systems, increase in Nb leads to negligible increases in strength and ductility. Further, from the trend of hardness observed in Figure 5.33, it is concluded that porosity increasing affects the hardness values of the Ti-4Fe alloys. The nature and distribution of the pores are visible from Figure 5.25. It is also seen that all metastable β alloys possess ultimate tensile strength greater than 1000 MPa, near β alloys

have slightly lesser strength and the β matrix α+β alloys have the least tensile strength compared to the other class of alloys. An inverse trend is however observed in the elongation to failure. It is notable that except for the Ti-4Fe system, the mechanical properties of the Ti-Nb-Fe alloys are primarily governed by the nature of the microstructure.

5.2.4 Fractography

5.2.4.1 Ti-2Nb system

Figure 5.34 shows the representative fractographs of Ti-2Nb-3Fe, Ti-2Nb-5Fe and Ti-2Nb-6Fe alloys corresponding to the Ti-2Nb system. It can be seen that, Ti-2Nb-3Fe consists only of dimples indicating a ductile fracture [51]. For Ti-2Nb-5Fe, with the addition of Fe, a few regions of flat surfaces and the other contains dimples can be observed. Ti-2Nb-6Fe is completely characterised by flat facets indicating a brittle fracture [94]. All three alloys possess spherical pores. Although the size and distribution are minimal.

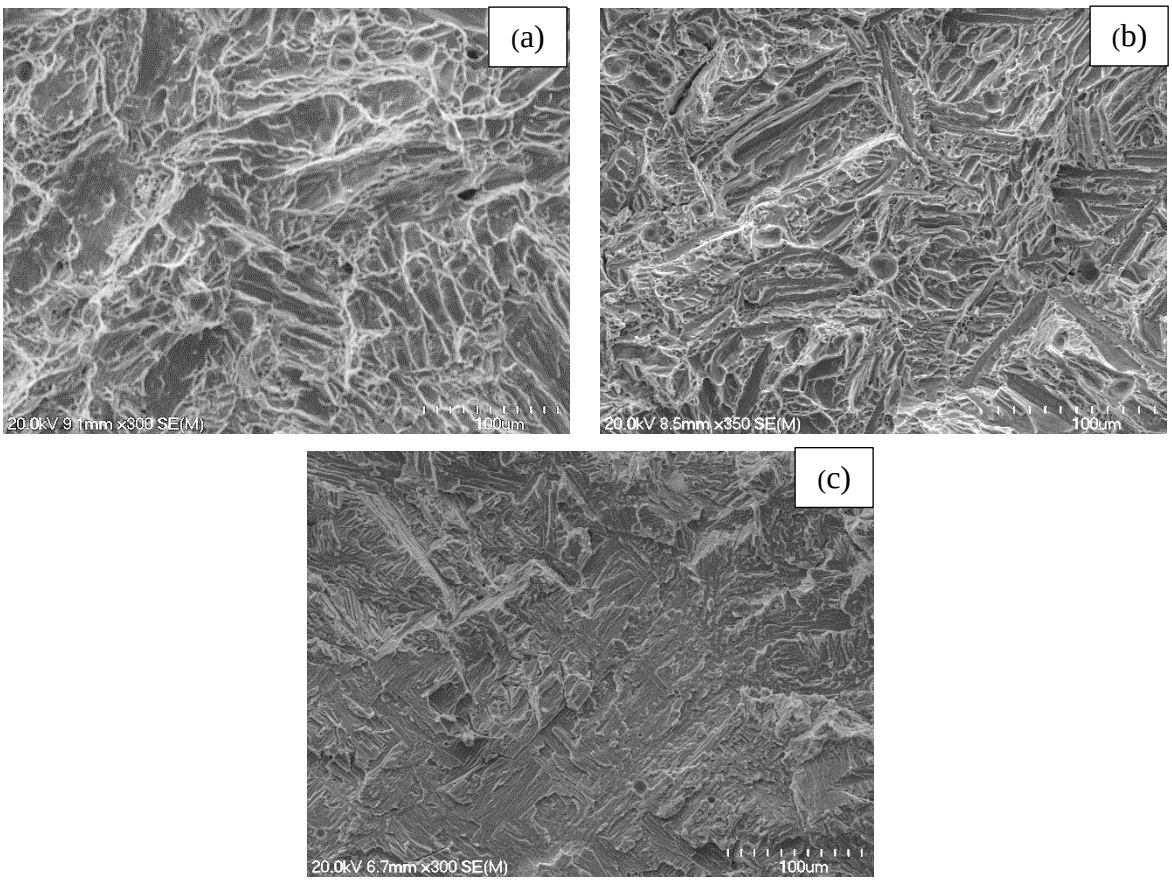

Figure 5.34 Representative fractographs of a) Ti-2Nb-3Fe, b) Ti-2Nb-5Fe, c) Ti-2Nb-6Fe corresponding to the Ti-2Nb system.

With the minimal alloying elements, Ti-2Nb-3Fe is characterised by a coarse Widmanstätten microstructure. With 98% of sintered density, the size and distribution of the pores is minimal. Thus, the nature of fracture is ductile. However, with the increase in alloying elements resulting in increased impediment of the dislocation, a few regions of smooth and flat surfaces are observed in Ti-2Nb-5Fe. A few patches of dimple like structures are also noticeable. Furthermore, Ti-2Nb-6Fe, with very fine lamellae and the highest tensile strength possessed the least elongation of failure which in turns justifies the presence of predominant smooth flat fracture surfaces.

In general, for the Ti-2Nb system, the green and sintered density are similar among the alloys, respectively. All alloys possess a sintered density of 98%. The XRD spectra indicate that Ti-2Nb-3Fe and Ti-2Nb-5Fe exhibit a few β peaks alongside the dominant α peaks. The micrographs (Figure 5.19) indicate that both the alloys are characterised by Widmanstätten microstructures. Ti-2Nb-6Fe shows a higher relative intensity at 39^{o} however, the other α peaks remain dominant and the microstructure as seen in Figure 5.19(e, f) is characterised by fine α+β lamellae. Henceforth, Ti-2Nb-3Fe and Ti-2Nb-5Fe are considered to be β matrix α+β alloys. Concurrent with that, both the alloys exhibit high strength and ductile behaviour (from Figure 5.26 and Figure 5.34(a, b)). Whereas Ti-2Nb-6Fe due to the very fine lamellae, possesses the highest strength but relatively lower elongation to failure. The fractograph (from Figure 5.34c**)** is conclusive evidence of the brittle fracture in Ti-2Nb-6Fe. Henceforth, Ti-2Nb-6Fe is regarded as a near β alloy.

5.2.4.2 Ti-5Nb and Ti-6Nb systems

Figure 5.35 shows the representative fractographs of Ti-5Nb-3Fe, Ti-5Nb-4Fe, Ti-6Nb-5Fe and Ti-6Nb-6Fe alloys corresponding to the Ti-5Nb and Ti-6Nb systems, respectively. It can be seen that the fracture surfaces of Ti-5Nb-3Fe is characterised by dimple like regions and rough edges while Ti-5Nb-4Fe consists of dimples and a few smooth facets. Ti-6Nb-5Fe is characterised by a mixture of clear facets, a few tear-ridges and dimple like structures. There are a few pores visible. For Ti-6Nb-6Fe, the fracture surface is covered with smooth facets and tear-ridges. A few elongated pores can also be spotted.

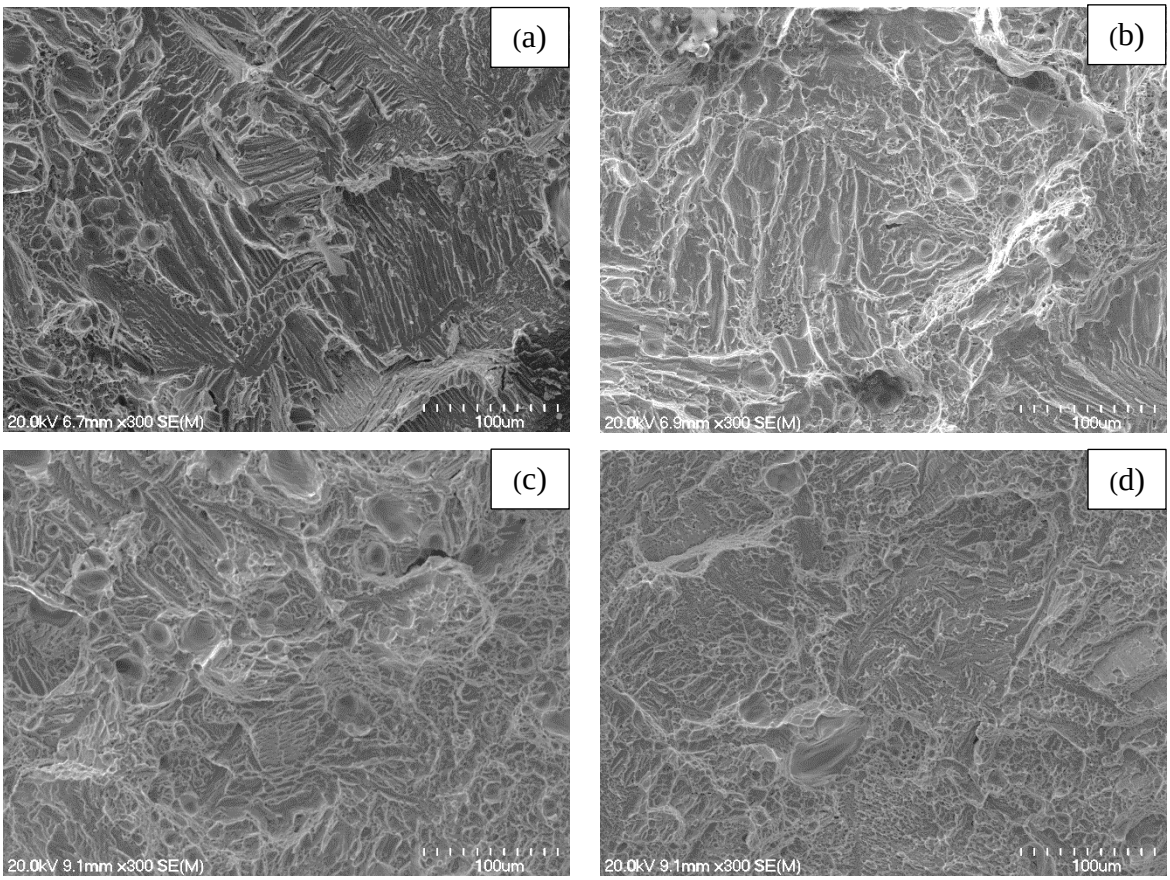

Figure 5.35 Representative fractographs of (a) Ti-5Nb-3Fe, (b) Ti-5Nb-4Fe, (c) Ti-6Nb-5Fe and (d) Ti-6Nb-6Fe alloys corresponding to the Ti-5Nb and Ti-6Nb systems, respectively.

The fracture surfaces of Ti-5Nb-3Fe, Ti-5Nb-4Fe, Ti-6Nb-5Fe and Ti-6Nb-6Fe agree with the corresponding physical and mechanical properties. With the addition of β stabilisers, Ti-5Nb-3Fe and Ti-5Nb-4Fe achieves a biphasic microstructure as a result, the nature of fracture remains ductile despite the increase in tensile strength. However, for Ti-6Nb-5Fe and Ti-6Nb-6Fe, due to the refinement of the grains, solid solution strengthening and porosity many regions with smooth and flat facets are visible.

Overall, for the Ti-5Nb and Ti-6Nb systems, all the alloys from the individual systems have similar green density and sintered density. Based on the XRD spectra as seen in Figure 5.20, Ti-5Nb-3Fe and Ti-5Nb-4Fe shows few β peaks however α phase remains the dominant. Following that, the microstructure primarily consists of Widmanstätten structures (Figure 5.21). Based on these factors, Ti-5Nb-3Fe and Ti-5Nb-4Fe are considered to be β matrix α+β alloys. Consequently, despite the increase in tensile strength, the elongation to failure remains the same. With Ti-6Nb-5Fe, the relative intensities of the peaks corresponding to the α and β phases remain the same. Further the micrograph is characterised by Widmanstätten with very fine overlapping lamellae. Hence, Ti-6Nb-5Fe is regarded as a near β alloy. The XRD spectra

of Ti-6Nb-6Fe shows dominant β peaks while the other α peaks with relatively less peak intensities. The micrograph consists of a mixture of acicular α lamellae and Widmanstätten microstructures. Consequently, Ti-6Nb-6Fe possesses the highest tensile strength and hardness with the least elongation to failure, the presence of acicular α tend to affect plastic deformation thereby escalating the strength and hardness. Hence Ti-6Nb-6Fe is regarded to be a metastable β alloy.

5.2.4.4 Ti-8Nb and Ti-9Nb systems

Figure 5.36 shows the representative fracture surfaces of Ti-8Nb-2Fe, Ti-8Nb-4Fe, Ti-9Nb-5Fe and Ti-9Nb-6Fe alloys corresponding to the Ti-8Nb and Ti-9Nb systems respectively. The fracture surfaces of both Ti-8Nb-2Fe and Ti-8Nb-4Fe are characterised majorly by dimple like structures. Dimples is indicative of ductile fracture and the hemispherical regions in Figure 5.36(a, b) is due to the spherical pores. Although majority of the pores in both these alloys are closed and spherical, there are a few elongated pores noticed. The distribution of elongated pores is especially higher in Ti-8Nb-4Fe. For the Ti-9Nb-5Fe, the fracture surface consists of a mixture of closed dimples and flat facets and tear-ridges. Likewise, for Ti-9Nb-6Fe the fracture surface consists of slightly elongated pores especially near the grain boundaries and the surface is characterised by smooth facets and tear-ridges. Although the size and distribution of pores is less in both the alloys from the Ti-9Nb when compared with the alloys of the Ti-8Nb system. This is due the small difference in the sintered density as seen in Table 5.8. The elongation to failure values from Table 5.12 agree with the nature of failure described on the basis of the fractography of Ti-8Nb-2Fe, Ti-8Nb-4Fe, Ti-9Nb-5Fe, and Ti-9Nb-6Fe.

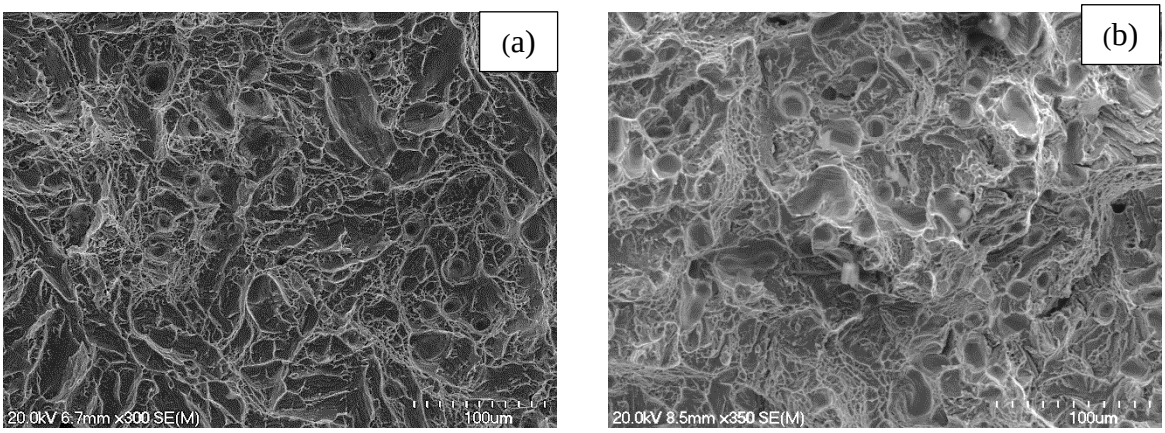

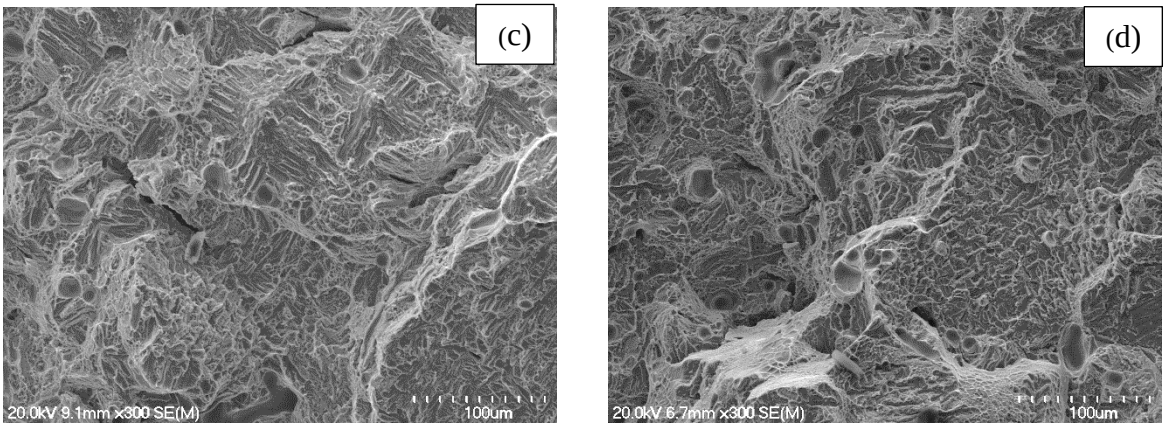

Figure 5.36 Representative fracture surfaces of (a) Ti-8Nb-2Fe, (b) Ti-8Nb-4Fe, (c) Ti-9Nb-5Fe and (d) Ti-9Nb-6Fe alloys corresponding to the Ti-8Nb and Ti-9Nb systems, respectively.

Thus, it is evident that the size and distribution of porosity affects the hardness and ductility of Ti-8Nb-4Fe to a certain extent. However, the presence of acicular α lamellae and the refinement in the α+β lamellae can be primarily attributed to the brittle fracture of Ti-9Nb-5Fe and Ti-9Nb-6Fe.

Overall, for the Ti-8Nb and Ti-9Nb systems, there is a slight variation between the green density of the individual alloys from each system. However, the sintered density is similar for all four alloys. It is noticeable that the densification values increase in both the systems which is indicative that most of the densification occurred during sintering due to the high diffusivity of Fe. From the XRD spectra of the alloys from both the systems (Figure 5.22), it can be inferred that Ti-8Nb-2Fe and Ti-8Nb-4Fe exhibited a few β peaks, the peaks corresponding to the α phase remains dominant. Corresponding to the XRD spectra, Ti-8Nb-2Fe and Ti-8Nb-4Fe shows Widmanstätten microstructures with differing lamellae thickness. The tensile strength and hardness gradually increase. Although the increase in hardness is not comparable with that of the strength. Hence it is clear that porosity has an effect on the decrease in the hardness. Based on the XRD, micrographs and mechanical behaviour Ti-8Nb-2Fe is classified as β matrix α+β alloy and Ti-8Nb-4Fe as near β alloy. Ti-9Nb-5Fe and Ti-9Nb-6Fe both show dominant β peaks while the former also shows few peaks corresponding to the α phase and latter shows a tiny peak corresponding to α'. Ti-9Nb-6Fe is characterised only by β peaks suppressing most of the α phase. The effect of adding of adding β stabilisers is observed from the micrographs seen in Figure 5.23**.** Ti-9Nb-5Fe is characterised by a mixture of Widmanstätten microstructures and acicular α. Ti-9Nb-6Fe consists of equiaxed β grains and meagre portions of acicular α lamellae. Due to the presence of acicular lamellae and high number of alloying elements, the Ti-9Nb-5Fe and Ti-9Nb-6Fe show a higher tensile strength

than the alloys from the Ti-8Nb system. The Rockwell hardness also follows a similar trend as that of tensile strength. Thus Ti-9Nb-5Fe and Ti-9Nb-6Fe are regarded as metastable β.

5.2.4.5 Ti-4Fe system

Figure 5.37 shows the representative fracture surfaces of (a) C.P. Ti, (b) Ti-3Nb-4Fe, (c) Ti-5Nb-4Fe and (d) Ti-8Nb-4Fe alloys corresponding to the Ti-4Fe system. Ti-3Nb-4Fe is characterised primarily by dimple like structures. A few spherical pores can be found. With the addition of Nb, the fracture surface of Ti-5Nb-4Fe is characterised by both dimples and flat facets. Notably, Ti-3Nb-4Fe and Ti-5Nb-4Fe show a similar looking fracture surface. In comparison to Ti-3Nb-4Fe, the nature and distribution of pores is high. The fracture surface of Ti-8Nb-4Fe consists of large number spherical and elongated pores. Ti-8Nb-4Fe consists of large number of spherical pores and a few elongated pores. Besides that, the surface is characterised by dimple like regions.

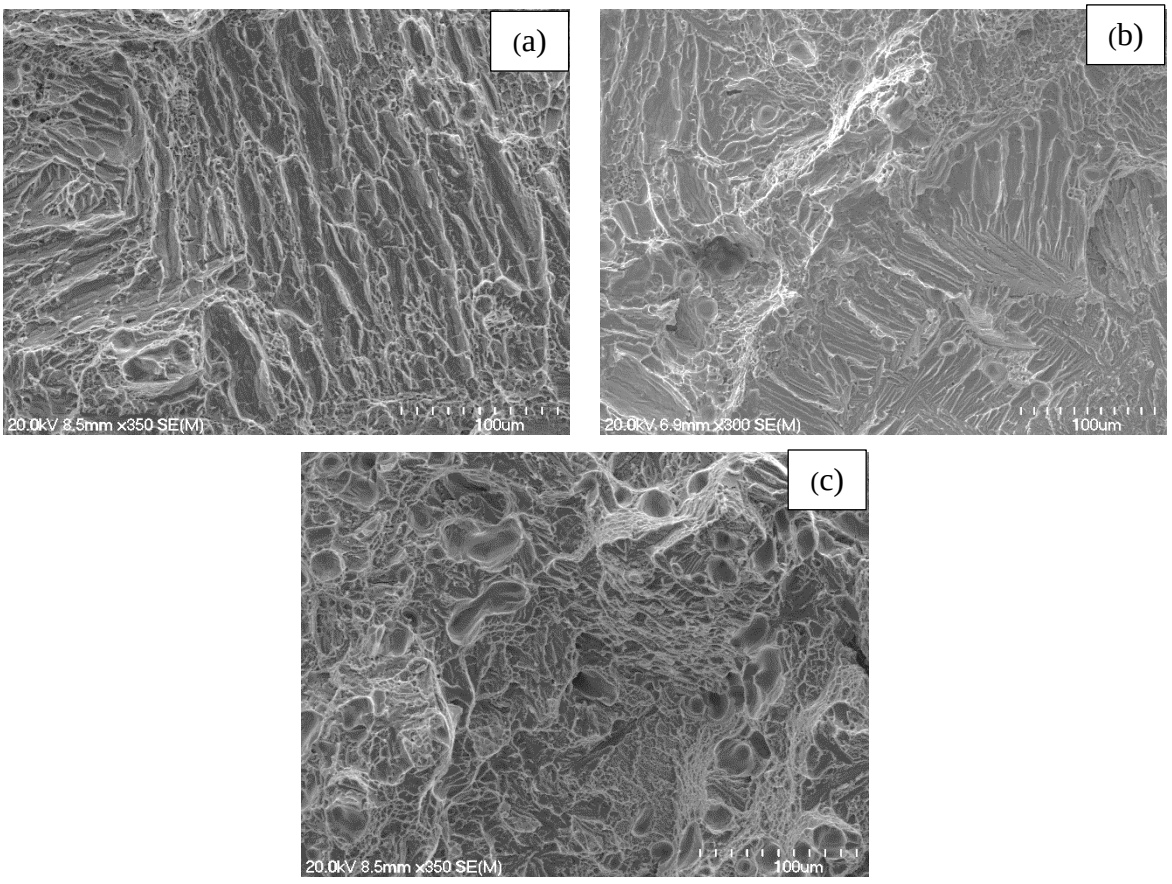

Figure 5.37 Representative fractographs of (a) Ti-3Nb-4Fe, (b) Ti-5Nb-4Fe and (c) Ti-8Nb-4Fe alloys corresponding to the Ti-4Fe system.

For the Ti-4Fe system, the difference in the green density appears to be significant with the addition of Nb. As a result, the sintered density of all the alloys also vary. It is speculated that

the reason for the significant drop in density is due to the high Nb:Fe (wt%) ratio in the compositions. Consequently, Ti-8Nb-4Fe has a sintered density less than 96%. It is observed that porosity heavily influences the ductility and hardness of the alloys, especially with Ti-8Nb-4Fe. Both Ti-3Nb-4Fe and Ti-5Nb-4Fe belong to the β matrix α+β alloy based on the XRD spectra (Figure 5.24) where α peaks remain dominant with a few β peaks gradually rising at 39^{o} and 57^{o}. The micrograph of Ti-3Nb-4Fe and Ti-5Nb-4Fe (Figure 5.25(a-d)) consists of Widmanstätten structures which is characteristic of α+β. Furthermore, like all α+β alloys, Ti-3Nb-4Fe and Ti-5Nb-4Fe possess a good combination of strength and mechanical properties. Ti-8Nb-4Fe despite showing equal relative intensities of α and β peaks, exhibits a Widmanstätten microstructure with ultra-fine lamellae overlapping each other. The refinement causes the strength to increases slightly. It is noticed that the elongation to failure also increases. Based on Figure 5.32 and Figure 5.33, it is concluded that if not for porosity, Ti-8Nb-4Fe will exhibit better mechanical properties. Henceforth, Ti-8Nb-4Fe is also regarded as near β alloy.

Taking everything into consideration, among the Ti-Nb-Fe alloys, all the alloys from their individual systems show a similar green density (±1.5%) except for the Ti-4Fe system. Majority of the alloys show sintered density above 96% except the Ti-8Nb and Ti-9Nb systems (95%). It is worth mentioning these systems have the highest number of alloying elements and the highest Nb content. The combination of the same lead to the drop in the green density which in turn affects the sintered density. However, the presence of Fe powders resulted in appreciable densification. This is evident from Table 5.9. Despite the large number of alloying elements, an increase in densification is observed and is indicated with a negative symbol as there is always a drop in the densification values with the addition of alloying elements in all other systems.

From the XRD spectra and the micrographs of the Ti-Nb-Fe alloys it is inferred that Ti-2Nb-3Fe, Ti-2Nb-5Fe, Ti-3Nb-4Fe, Ti-5Nb-3Fe, Ti-5Nb-4Fe, Ti-8Nb-2Fe belong to the β matrix α+β category as they exhibit a few β peaks amidst dominant α peaks and their microstructure is characterised by coarse Widmanstätten microstructures. Ti-6Nb-6Fe, Ti-9Nb-5Fe and Ti-9Nb-6Fe are categorised as metastable β as they display dominant β peaks while suppressing a majority of the α peaks. Further, their micrographs distinctly contained equiaxed β grains with varying needle like αlamellae. Next up, Ti-2Nb-6Fe, Ti-6Nb-5Fe and Ti-8Nb-4Fe are considered to be near β alloys. These alloys show equal peak intensities of α and β phases and their microstructures are characterised by both Widmanstätten microstructures and varying proportions of individual α lamellae. Kolli et al. [87] stated that near β alloys are in between

the α+β (a.k.a β matrix α+β alloys) and metastable β alloys hence possess a mixture of both the categorises.

Ti alloys are categorised as β matrix α+β alloys (MoE≤ 5), near β, metastable β (10 ≤ MoE ≤30) and fully stable β (MoE ≥ 30) [80; 87]. Keeping these MoE ranges as baseline the alloys were classified on the basis of their XRD and microstructures. It is found that the Equation (4-1) used to deduce the MoE values seems to be inaccurate according to the current research. Therefore, Equation (4-2) is proposed in order to provide relatively accurate MoE values that agree with the above classification. Table 5.14 shows the classification of Ti-Nb-Fe alloys and their MoE values calculated from Equations (4-1) and (4-2).

Table 5.14 Classification of Ti-Nb-Fe alloys

System	Sample	MoE (4-1)	MoE (4-3)	Classification
	C.P. Ti	0.0	0.0	α - Ti
Ti-2Nb	Ti-2Nb-3Fe	9.3	6.4	β matrix α+β
	Ti-2Nb-5Fe	15.1	10.2	
	Ti-2Nb-6Fe	18.0	12.1	near β
Ti-5Nb	Ti-5Nb-3Fe	10.1	7.2	β matrix α+β
	Ti-5Nb-4Fe	13.0	9.1	
Ti-6Nb	Ti-6Nb-5Fe	16.2	11.3	near β
	Ti-6Nb-6Fe	19.1	13.3	Metastable β
Ti-8Nb	Ti-8Nb-2Fe	8.1	6.1	β matrix α+β
	Ti-8Nb-4Fe	13.9	10.0	near β
Ti-9Nb	Ti-9Nb-5Fe	17.1	12.2	Metastable β
	Ti-9Nb-6Fe	20.0	14.1	
Ti-4Fe	Ti-3Nb-4Fe	12.5	8.6	β matrix α+β

In accordance with the above classification, metastable alloys possess the highest tensile strength and Rockwell hardness. However, they show poor ductility as indicated by their corresponding fractographs. It is worth mentioning that Ti-9Nb-5Fe has the highest elongation strain of 5%. It can be attributed to the high Nb content. Likewise, the near β alloys exhibit slightly better mechanical properties. Finally, the α+β alloys, show lowest strength values and comparable elongation to failure values. Overall, it is true in saying that Nb governs the ductility while Fe aids improve the tensile strength and hardness. Also, all alloys containing 6wt% Fe irrespective of the Nb content, tend to undergo brittle fracture. The above-mentioned properties are severely influenced by the microstructural features. Except for the Ti-4Fe system, where the properties are affected by porosity.

Figure 5.38 displays the tensile strength of various α+β and metastable alloys along with the metastable Ti-Nb-Fe alloys. It can be noticed that Ti-9Nb-6Fe has the highest tensile strength than the other alloys. While, Ti-9Nb-5Fe and Ti-6Nb-6Fe are comparable with Ti-12Mo-5Zr and Ti-13Nb-13Zr. To conclude, all the metastable Ti-Nb-Fe alloys have higher tensile strength than the existing biomedical alloys and the near β Ti-Nb-Fe are comparable with the same.

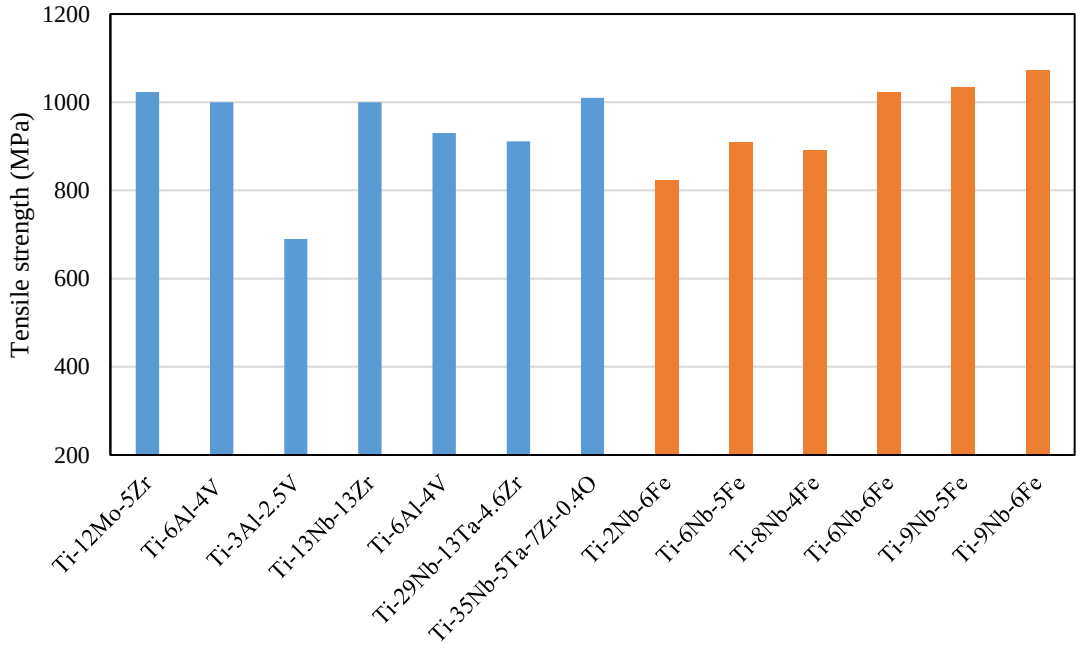

Figure 5.38 Tensile strength of various biomedical α+β/metastable alloys and Ti-Nb-Fe alloys from the current research [4; 41; 89; 95; 96].

Chapter Six

Comparison of Ti-Nb-Mn and Ti-Nb-Fe alloys

Based on the analysis of the Ti-Nb-Mn and Ti-Nb-Fe alloys, it is seen that there are a few similarities between them. Therefore, this section aims to compare the similarities on the basis of MoE and the nature of alloying elements and try to understand its effect on the microstructure and mechanical properties.

6.1 Based on MoE

This section aims to compare the Ti-Nb-Mn and Ti-Nb-Fe alloys on the basis of their MoE values. It is seen that MoE values calculated from equation (4-1) are consistent with the characteristics of Ti-Nb-Mn alloys. However, for the Ti-Nb-Fe alloys, the MoE values calculated from equation (4-2) seems comparable with its XRD and micrographs. Therefore, a combination of equation (4-1) and (4-2) is suggested while comparing both the systems.

$$\text{MoE} = (0.28 \times [\text{Nb}]\text{wt\%}) + (1.54 \times [\text{Mn}]\,\text{wt\%}) + (1.93 \times [\text{Fe}]\,\text{wt\%}) \qquad (6\text{-}1)$$

6.1.1 MoE = 10

Ti-3Nb-6Mn, Ti-2Nb-5Fe and Ti-8Nb-4Fe alloys have MoE values of around 10. Both Ti-3Nb-6Mn and Ti-8Nb-4Fe show similar trend of α and β peaks, while Ti-3Nb-6Mn has a slightly less β peak intensity (Figure 5.3 and Figure 5.22, respectively). Subsequently, Ti-8Nb-4Fe microstructure seems to be much refined (Figure 5.23(c, d)). Yet, both Ti-2Nb-5Fe and Ti-8Nb-4Fe show comparable tensile strength and shows almost twice elongation to failure as Ti-3Nb-6Mn. Similarly, Ti-8Nb-4Fe shows comparable hardness values. It is worth mentioning that both Ti-8Nb-4Fe belong to the near β category and is conclusive that it possesses excellent combination of mechanical properties. Between Ti-3Nb-6Mn and Ti-2Nb-5Fe, despite being α+β alloys, the former possesses relatively less ductility. Figure 5.11c and Figure 5.34b clearly illustrates the nature of failure and the pore characteristics of the α+β alloys with MoE = 10.

6.1.2 MoE = 12

Ti-2Nb-6Fe and Ti-9Nb-5Fe show similar peak intensities in their XRD spectra with dominant β peaks amidst other α peaks (Figure 5.18 and Figure 5.22, respectively). In terms of the microstructural characteristics, Ti-9Nb-5Fe < Ti-4Nb-7Mn < Ti-2Nb-6Fe is the observed trend of interlamellar spacing (Figure 5.6(e, f), Figure 5.22(e, f), Figure 5.18(e, f)). This indicates that Ti-9Nb-5Fe has a major proportion of refined α+ β lamellae followed by Ti-4Nb-7Mn. It is noticeable that the thickness of the lamellae for both are similar. With Ti-2Nb-6Fe, the lamellae appear to be slightly coarser. On that note, Ti-4Nb-7Mn and Ti-9Nb-5Fe shows quite similar tensile strength values. But Ti-9Nb-5Fe exhibits much higher elongation of failure (5%) despite being a metastable alloy. Ti-2Nb-6Fe on the other hand, possess relatively lower strength and ductility, it can be attributed to the high Fe: Nb ratio as it has been identified that Nb aids with improving ductility while Fe improves strength due to solid solution strengthening. All three alloys similar hardness values of 67(±1) HRA.

6.1.3 MoE = 13

Both the metastable alloys Ti-2Nb-8Mn and Ti-6Nb-6Fe have a MoE value of about 13. The XRD spectra shows that both the alloys display a dominant β peak where the other α peaks are have relatively fewer peak intensities (Figure 5.6 and Figure 5.21). Observing the microstructure, it is clear that Ti-2Nb-8Mn has fewer proportion of α lamellae within the equiaxed β grains whereas Ti-6Nb-6Fe has very fine α+β lamellae with a few acicular α along the grain boundary (Figure 5.6(a, b) and Figure 5.21(g, h)). Nevertheless, both the alloys possess comparable tensile strength. Due to the nature of microstructure, both the alloys exhibit a brittle behaviour. Both the alloys are characterised by river like patterns and smooth facets. Correspondingly, display both the metastable alloys exhibit similar hardness values.

6.1.4 MoE = 14

Ti-4Nb-9Mn, Ti-6Nb-8Mn and Ti-9Nb-6Fe shows MoE value about 14. The XRD spectra of Ti-4Nb-9Mn and Ti-9Nb-6Fe show only β peaks with rest of the α peaks mostly suppressed (Figure 5.5 and Figure 5.22, respectively). Further, both the alloys show a tiny peak corresponding to the orthorhombic α'' phase at around 43^{o}. Ti-6Nb-8Mn displays prominent β peaks with few other suppressed α peaks present. The micrographs of all three alloys look similar, with equiaxed β grains enclosing the needle shaped acicular α. The proportion of the α

might however vary. All three alloys exhibit brittle failure as indicated in Figure 5.12 (b, d) and Figure 5.36(g, h) however, the tensile strength is above 1000 MPa and are comparable. Due to the orthorhombic phase, the hardness of Ti-4Nb-9Mn and Ti-9Nb-6Fe is slightly higher than Ti-6Nb-8Mn.

It is therefore conclusive that since most of the properties of the Ti-Nb-Mn and Ti-Nb-Fe are rather dependant on the microstructural features than the porosity, most of the alloys with similar MoE values possess similar mechanical properties. Also, it becomes evident from the comparison that the properties of the alloys are concurrent with the corresponding classification (based on the MoE).

6.2 Based on the system

For the comparison of the Ti-Nb-Mn and Ti-Nb-Fe alloys based on the system, the number of alloying elements and the nature of alloying elements (Fe/Mn) are regarded as prime factors while the mechanical properties are used to quantitatively analyse its behaviour. Figure 6.1 shows the relationship/dependence of sintered density on the ultimate tensile strength for the Ti-Nb-Mn and Ti-Nb-Fe alloys.

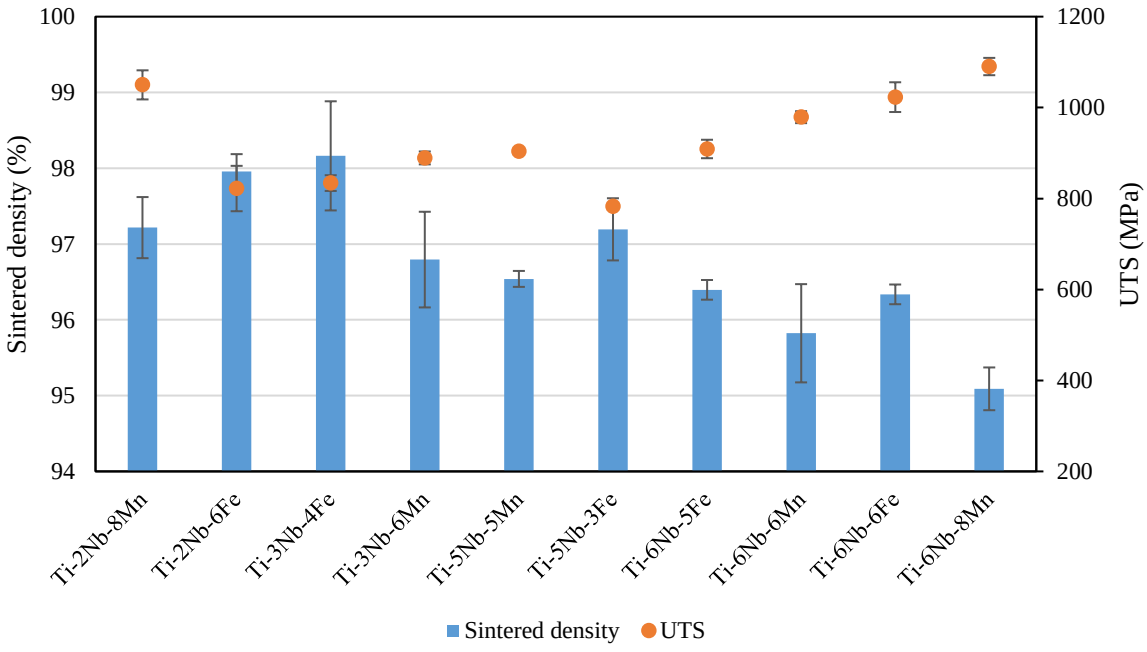

Figure 6.1 Relationship between sintered density and UTS for Ti-Nb-Mn and Ti-Nb-Fe alloys.

6.2.1 Ti-2Nb system

Ti-2Nb-8Mn and Ti-2Nb-6Fe have a total number of alloying elements of 10 wt% and 8 wt% respectively. This difference leads to the difference in the green and sintered density values of the alloys. With the increase in alloying elements, the resistance to compaction increases [2]. The sintered density of Ti-2Nb-8Mn and Ti-2Nb-6Fe is very similar despite the difference in green density. From Figure 5.6(a, b) and Figure 5.19(e, f) it is clear that both the alloys are characterised by spherical pores. However, the number of pores is higher in the latter. The difference in porosity values results in increased distribution of the spherical pores. Although the density of Ti-2Nb-8Mn is lower than Ti-2Nb-6Fe, the yield and ultimate tensile strength of the latter is higher. The presence of acicular α lamellae in Figure 5.6(a, b) can be attributed to the high tensile strength and hardness of Ti-2Nb-8Mn. For the Ti-2Nb-6Fe, although the interlamellar spacing of the lamellae is high, they are slightly coarser when compared to Ti-2Nb-8Mn. Besides, the metastable alloys always possess higher strength α+β alloy or near β alloy.

6.2.2 Ti-3Nb system

Between Ti-3Nb-6Mn and Ti-3Nb-4Fe and, the latter has a higher green density (comparing Table 5.1 and Table 5.9). The difference in the green density is around 1.5%. As a result, a similar trend follows with respect to the sintered density. Ti-3Nb-6Mn has higher tensile strength than Ti-3Nb-4Fe and subsequently, lesser elongation to failure. The hardness values however, is seen to be equal. The difference in density values can be attributed to the number of alloying elements. However, the reason for the increase in tensile strength is due to refinement of the α+β lamellae as seen in Figure 5.4 (e, f) as opposed to Figure 5.25 (a, b). It is worth mentioning that both the alloys belong to the β matrix α+β alloy yet Ti-3Nb-4Fe exhibits a slightly higher % elongation. This can be reasoned on the basis of the individual micrographs i.e. the interlamellar spacing of Ti-3Nb-4Fe is much less than Ti-3Nb-6Mn which indicates that the α+β lamellae is coarser (Figure 5.25(a, b)) when compared with that of Ti-3Nb-6Mn (Figure 5.4(e, f)) and. The XRD spectra also indicate that the primary β peak at 39^{o} of Ti-3Nb-4Fe is less than Ti-3Nb-6Mn.

6.2.3 Ti-5Nb system

Ti-5Nb-5Mn and Ti-5Nb-3Fe belong to the Ti-5Nb system. It is seen that Ti-5Nb-5Mn has a slightly higher green density than Ti-5Nb-3Fe (Table 5.1 and Table 5.7). However, the densification of Ti-5Nb-3Fe is also higher than Ti-5Nb-5Mn. Consequently, despite the difference in the green density, the sintered density of the two alloys are the same. Ti-5Nb-5Mn has a higher tensile strength and hardness than Ti-5Nb-3Fe. However, the elongation to failure of the two alloys are relatively closer (Table 5.3 and Table 5.11).

The slightly higher green density of Ti-5Nb-5Mn can be attributed to the lesser number of alloying elements when compared to Ti-5Nb-3MFe. The higher diffusivity of both Mn and Fe is the reason for the almost equal sintered density[69; 70]. Despite equal sintered density the tensile strength of Ti-5Nb-5Mn is higher than Ti-5Nb-3Fe. This can be attributed to the microstructural features due to the addition of Mn. The same becomes the reason for the increase in hardness values. Since both the alloys belong to the α+β category the elongation to failure values for both alloys are comparable.

6.2.4 Ti-6Nb system

For the Ti-6Nb system, the comparison is done in two parts. Firstly, Ti-6Nb-6Mn is compared against Ti-6Nb-6Fe and Ti-6Nb-5Fe. Following that, Ti-6Nb-8Mn is compared against Ti-6Nb-5Fe and Ti-6Nb-6Fe.

Among Ti-6Nb-5Fe, Ti-6Nb-6Mn and Ti-6Nb-6Fe, all three alloys have a similar green and sintered density. However, Ti-6Nb-5Fe has the lowest tensile strength and hardness whilst Ti-6Nb-6Fe has the highest tensile strength and hardness. The elongation to failure values of Ti-6Nb-5Fe and Ti-6Nb-6Mn are similar and Ti-6Nb-6Fe showed a lesser elongation to failure. Despite equal number of alloying elements, Ti-6Nb-6Fe has better tensile strength and hardness than Ti-6Nb-6Mn (Table 5.1 and Table 5.11).

Based on the XRD spectra of Ti-6Nb-5Fe although there are a few β peaks, the principal α peak corresponding at 40^{o} remains dominant. However, for Ti-6Nb-6Fe, the α peaks are suppressed due to the increase in Fe content (Figure 5.20). Also, the micrograph of Ti-6Nb-6Fe (Figure 5.20(g, h))shows very fine α+β lamellae along with acicular α emerging from the grain boundaries. Whereas, in the case of Ti-6Nb-5Fe and Ti-6Nb-6Mn consists of fine Widmanstätten microstructures. Thus, Ti-6Nb-6Fe being a metastable β possess higher tensile

strength and Rockwell hardness while Ti-6Nb-5Fe and Ti-6Nb-6Mn are near β alloys with a good combination of high strength and ductility.

Between Ti-6Nb-6Fe and Ti-6Nb-8Mn, Ti-6Nb-6Fe has a higher green and sintered density. However, the Ti-6Nb-8Mn has higher tensile strength. The elongation to failure and hardness values for both the alloys are quite similar.

From the XRD spectra (Figure 5.20 and Figure 5.5), albeit both the alloys exhibit a prominent β peaks the microstructure reveals that Ti-6Nb-6Fe has a few regions of Widmanstätten microstructures while Ti-2Nb-8Mn presents equiaxed β grains with slight proportions of acicular α lamellae. This shall also be an evidence for the poor ductility for both the alloys.

To conclude from the comparison of Ti-Nb-Mn and Ti-Nb-Fe alloys based on the number and nature of alloying elements it is evident that although the number of alloying elements in both the systems are not equal, the difference is negligible (~3%). For such a small change in the composition, the change observed in the strength and hardness is relatively higher. In addition, all alloys except Ti-6Nb-8Mn have sintered density higher than 96%. Therefore, the dependence of the hardness and elongation to failure is more on the microstructural features such as proportion of the α+β lamellae and interlamellar spacing than porosity. Notably, all the mechanical properties are in accordance with the XRD spectra and micrographs.

Chapter Seven

Conclusions

7.1 Conclusions

- Ti-1Nb-5Mn and Ti-6Nb-8Mn possess the highest and lowest sintered density of 98% and 95%, respectively. It can be seen from Table 5.1 and the densification values tend to drop within each system.
- Among the Ti-Nb-Mn alloys, Ti-2Nb-8Mn has the highest densification of 67%. It is notable that the decrease % is the highest of 32.3 in the Ti-5Mn system followed by 25.8 in the Ti-8Mn system and is the least with the Ti-4Nb system. Incidentally, between Ti-5Mn and Ti-8Mn systems, the increase in Nb content is 4wt%. It is therefore evident that Nb content significantly affects the densification phenomenon.
- On that note, the minimal decrease in densification for the Ti-4Nb system can be reasoned on the basis of high diffusivity of Mn in Ti. All alloys except Ti-6Nb-8Mn exhibit relative sintered density above 96% which is indicative of reaching the final stage of sintering.
- Ti-3Nb-4Fe and Ti-9Nb-6Fe show the highest and lowest green density (94.5% and 89.8% respectively). Ti-2Nb-3Fe and Ti-9Nb-5Fe shows the highest and lowest sintered density (98.4% and 95.0%). Among all the system, alloys from Ti-8Nb and Ti-9Nb show an increase in densification while the other systems show a decline.
- Among all, C.P. Ti shows the least porosity (~1%) whereas Ti-6Nb-8Mn, due to the high Nb content, has the highest porosity of 4.9%.
- Ti-1Nb-5Mn, Ti-5Nb-5Mn and Ti-3Nb-6Mn, Ti-2Nb-3Fe, Ti-2Nb-5Fe, Ti-3Nb-4Fe, Ti-5Nb-3Fe, Ti-5Nb-4Fe and Ti-8Nb-2Fe are considered to be β matrix α+ β alloys as they showed a few β peaks amidst dominant α peaks and Widmanstatten microstructures. Ti-6Nb-6Mn, Ti-2Nb-6Fe, Ti-6Nb-5Fe, Ti-8Nb-4Fe being borderline α+β and metastable β alloy, it is contemplated to be near β alloy. Meanwhile, all the alloys belonging to the Ti-8Mn, Ti-4Nb, Ti-9Nb systems and Ti-6Nb-6Fe are interpreted as metastable β alloys. Ti-4Nb-9Mn and Ti-9Nb-6Fe show an orthorhombic α'' phase and the mechanical behaviour of theses alloys are concordant with the classification.
- Among the Ti-Nb-Mn alloys, Ti-1Nb-5Mn and Ti-6Nb-6Mn possess the lowest and highest yield strengths of 778 MPa and 1050 MPa, respectively. Correspondingly, Ti-1Nb-5Mn and Ti-6Nb-8Mn possess the highest and lowest ultimate tensile strength of

841 MPa and 1090 MPa respectively. Ti-5Nb-5Mn showed the highest elongation to fracture of 5%.

- Ti-1Nb-5Mn and Ti-4Nb-9Mn exhibit the lowest and highest Rockwell Hardness values of 65.8 and 69.5 HRA.
- Among the Ti-Nb-Fe alloys, Ti-2Nb-3Fe presents the lowest yield and ultimate tensile strength of 608 MPa and 743 MPa, respectively while Ti-9Nb-6Fe exhibits the highest yield and ultimate tensile strength of 1059 MPa and 1071 MPa, respectively. Conversely, Ti-2Nb-3Fe shows the highest elongation to failure (11%) and vice versa (1.6%).
- Ti-2Nb-3Fe and Ti-9Nb-6Fe show the highest and lowest hardness values of 63.2 and 69.4 HRA respectively.
- It is notable that all alloys possess yield and ultimate tensile strengths higher than C.P. Ti (456 and 588 MPa respectively). However, C.P. Ti has elongation to failure value of 10.3%.
- All metastable alloys i.e. Ti-2Nb-8Mn, Ti-6Nb-8Mn and Ti-4Nb-9Mn, Ti-6Nb-6Fe, Ti-9Nb-5Fe and Ti-9Nb-6Fe exhibit higher tensile strength than homogenised Ti-12Mo-5Zr, Ti-15Zr-10Mo, Ti-15Zr-15Mo, TNZT, Ti-15Mo.

7.2 Scope for future research

- In order to enhance the mechanical performance and make the Ti-Nb-Mn and Ti-Nb-Fe alloys more suitable for biomedical application, the near β alloys can be thermo-mechanically processed and the metastable β alloys can be heat treated, especially (Ti-4Nb-9Mn and Ti-9Nb-6Fe) to form fully stable β.
- Investigating various other mechanical properties such as fatigue property, corrosion resistance of Ti-Nb-Mn and Ti-Nb-Fe alloys is required
- Determining the Young's modulus of the alloys using ultrasonic measurements or nano indentation testing.
- Investigating the biocompatibility of the alloys by exposing the metals to cell culture assays and studying its ion release behaviour and cytotoxic behaviour.

References

[1] Kaur, M., & Singh, K. (2019). Review on titanium and titanium based alloys as biomaterials for orthopaedic applications. *Mater Sci Eng C Mater Biol Appl, 102*, 844-862.

[2] German, R. M. (2005). *Powder metallurgy and particulate materials processing: the processes, materials, products, properties and applications*. Metal powder industries federation Princeton.

[3] Li, Y., Yang, C., Zhao, H., Qu, S., Li, X., & Li, Y. (2014). New developments of Ti-based alloys for biomedical applications. *Materials, 7*(3), 1709-1800.

[4] Katti, K. S. (2004). Biomaterials in total joint replacement. *Colloids and surfaces B: Biointerfaces, 39*(3), 133-142.

[5] Weng, W., Biesiekierski, A., Li, Y., & Wen, C. (2019). Effects of selected metallic and interstitial elements on the microstructure and mechanical properties of beta titanium alloys for orthopedic applications. *Materialia, 6*.

[6] Williams, D. F. (2008). On the mechanisms of biocompatibility. *Biomaterials, 29*(20), 2941-2953.

[7] Niinomi, M., Liu, Y., Nakai, M., Liu, H., & Li, H. (2016). Biomedical titanium alloys with Young's moduli close to that of cortical bone. *Regenerative biomaterials, 3*(3), 173-185.

[8] Niinomi, M., Nakai, M., & Hieda, J. (2012). Development of new metallic alloys for biomedical applications. *Acta Biomater, 8*(11), 3888-903.

[9] Chen, Q., & Thouas, G. A. (2015). Metallic implant biomaterials. *Materials Science and Engineering: R: Reports, 87*, 1-57.

[10] Mazzocca, A. D., Caputo, A. E., Browner, B. D., Mast, J. W., & Mendes, M. W. (1998). Principles of internal fixation. In B. D. Browner, J. B. Jupiter, A. M. Levine & P. G. Trafton (Eds.), *Skeletal Trauma* (2nd ed., Vol. 1, pp. 287-348). Philadelphia Saunders.

[11] Rostoker, W., Chao, E., & Galante, J. (1978). Defects in failed stems of hip prostheses. *Journal of biomedical materials research, 12*(5), 635-651.

[12] Davis, J. R. (2003). *Handbook of materials for medical devices*. ASM International.

[13] Goriainov, V., Cook, R., J, M. L., D, G. D., & Oreffo, R. O. (2014). Bone and metal: an orthopaedic perspective on osseointegration of metals. *Acta Biomater, 10*(10), 4043-57.

[14] Lütjering, G., & Williams, J. C. (2007). *Titanium*. Springer Science & Business Media.

[15] Leyens, C., & Peters, M. (Eds.). (2001). *Titanium and Titanium Alloys*. Wiley.

[16] Bania, P. J. (1994). Beta titanium alloys and their role in the titanium industry. *Jom, 46*(7), 16-19.

[17] Wang, Q., Dong, C., & Liaw, P. K. (2015). Structural stabilities of β-Ti alloys studied using a new Mo equivalent derived from [β/(α+ β)] phase-boundary slopes. *Metallurgical and Materials Transactions A, 46*(8), 3440-3447.

[18] Froes, F. H. S. (2015). A historical perspective of titanium powder metallurgy. *Titanium Powder Metallurgy*, 1-19.

[19] Powell, R. L., & Tao, L. C. (Compiler) (1961). *Reclaiming scrap titanium*: Google Patents.

[20] Barbis, D. P., Gasior, R. M., Walker, G. P., Capone, J. A., & Schaeffer, T. S. (2015). Titanium powders from the hydride–dehydride process. In *Titanium Powder Metallurgy* (pp. 101-116).

[21] Coube, O., & Riedel, H. (2000). Numerical simulation of metal powder die compaction with special consideration of cracking. *Powder Metallurgy, 43*(2), 123-131 %@ 0032-5899.

[22] Lapovok, R., Tomus, D., & Muddle, B. C. (2008). Low-temperature compaction of Ti–6Al–4V powder using equal channel angular extrusion with back pressure. *Materials Science and Engineering: A, 490*(1-2), 171-180 %@ 0921-5093.

[23] Sonsino, C. M., & Ratzi, R. (2004). Warm powder compaction substitutes conventionally double pressed and double sintered synchroniser hubs. *Powder metallurgy, 47*(4), 352-357 %@ 0032-5899.

[24] Jia, M., & Zhang, D. (2015). Warm compaction of titanium and titanium alloy powders. In *Titanium Powder Metallurgy* (pp. 183-200).

[25] Hanejko, F. G. (1998). Warm compaction. *ASM Handbook, 7*, 376-381.

[26] Laptev, A., Vyal, O., Bram, M., Buchkremer, H. P., & Stöver, D. (2005). Green strength of powder compacts provided for production of highly porous titanium parts. *Powder Metallurgy, 48*(4), 358-364 %@ 0032-5899.

[27] Luo, S. D., Yang, Y. F., Schaffer, G. B., & Qian, M. (2014). Warm die compaction and sintering of titanium and titanium alloy powders. *Journal of Materials Processing Technology, 214*(3), https://doi.org/10.1016/j.jmatprotec.2013.10.010.

[28] Kondoh, M., Saito, T., & Takamiya, H. (Compiler) (2004). *Green compact and process for compacting the same, metallic sintered body and process for producing the same, worked component part and method of working*: Google Patents.

[29] Qian, M., Yang, Y. F., Luo, S. D., & Tang, H. P. (2015). Pressureless sintering of titanium and titanium alloys: sintering densification and solute homogenization. In *Titanium Powder Metallurgy* (pp. 201-218).

[30] Rostron, D. W. (Compiler) (1951). *Method of sintering titanium and like metals*: Google Patents.

[31] Marty, M., Octor, H., & Walder, A. (Compiler) (1986). *Process for forming a titanium base alloy with small grain size by powder metallurgy*: Google Patents.

[32] Williams, J., Hickman, B., & Marcus, H. (1971). The effect of omega phase on the mechanical properties of titanium alloys. *Metallurgical transactions, 2*(7), 1913-1919.

[33] Mishin, Y., & Herzig, C. (2000). Diffusion in the Ti–Al system. *Acta materialia, 48*(3), 589-623.

[34] Yao, P. (2012). Density functional theory study of the self-diffusion in pure beta titanium and titanium alloys.

[35] Hennig, R. G., Trinkle, D. R., Bouchet, J., Srinivasan, S. G., Albers, R. C., & Wilkins, J. W. (2005). Impurities block the α to ω martensitic transformation in titanium. *Nature materials, 4*(2), 129-133.

[36] Murray, J. L. (1987). Phase diagrams of binary titanium alloys. *ASM international*, 340-345.

[37] Yan, M. (2015). Microstructural characterization of as-sintered titanium and titanium alloys. In *Titanium Powder Metallurgy* (pp. 555-578).

[38] Chapala, P., Sunil Kumar, P., Joardar, J., Bhandari, V., & Acharyya, S. G. (2019). Effect of alloying elements on the microstructure, coefficient of friction, in-vitro corrosion and antibacterial nature of selected Ti-Nb alloys. *Applied Surface Science, 469*, 617-623.

[39] Chinzei, K., Kikinis, R., & Jolesz, F. A. (1999). MR compatibility of mechatronic devices: design criteria. In *International Conference on Medical Image Computing and Computer-Assisted Intervention* (pp. 1020-1030): Springer.

[40] Eisenbarth, E., Velten, D., Müller, M., Thull, R., & Breme, J. (2004). Biocompatibility of β-stabilizing elements of titanium alloys. *Biomaterials, 25*(26), 5705-5713.

[41] Geetha, M., Singh, A. K., Asokamani, R., & Gogia, A. K. (2009). Ti based biomaterials, the ultimate choice for orthopaedic implants – A review. *Progress in Materials Science, 54*(3), 397-425.

[42] Zhao, D., Chang, K., Ebel, T., Qian, M., Willumeit, R., Yan, M., & Pyczak, F. (2013). Microstructure and mechanical behavior of metal injection molded Ti-Nb binary alloys as biomedical material. *J Mech Behav Biomed Mater, 28*, 171-82.

[43] Yılmaz, E., Gökçe, A., Findik, F., & Gulsoy, H. (2018). Metallurgical properties and biomimetic HA deposition performance of Ti-Nb PIM alloys. *Journal of Alloys and Compounds, 746*, 301-313.

[44] Hon, Y.-H., Wang, J.-Y., & Pan, Y.-N. (2003). Composition/phase structure and properties of titanium-niobium alloys. *Materials transactions, 44*(11), 2384-2390 %@ 1345-9678.

[45] Chen, Y., Han, P., Dehghan-Manshadi, A., Kent, D., Ehtemam-Haghighi, S., Jowers, C., Bermingham, M., Li, T., Cooper-White, J., & Dargusch, M. S. (2020). Sintering and biocompatibility of blended elemental Ti-xNb alloys. *Journal of the mechanical behavior of biomedical materials, 104*, 103691.

[46] Thibon, I., Ansel, D., & Gloriant, T. (2009). Interdiffusion in β-Ti–Zr binary alloys. *Journal of alloys and compounds, 470*(1-2), 127-133.

[47] Guthoff, F., Hennion, B., Herzig, C., Petry, W., Schober, H., & Trampenau, J. (1994). Lattice dynamics and self-diffusion in niobium at elevated temperatures. *Journal of Physics: Condensed Matter, 6*(31), 6211.

[48] Henriques, V. A. R., Galvani, E. T., Petroni, S. L. G., Paula, M. S. M., & Lemos, T. G. (2010). Production of Ti–13Nb–13Zr alloy for surgical implants by powder metallurgy. *Journal of Materials Science, 45*(21), 5844-5850.

[49] Santos, D. R., Pereira, M. S., Cairo, C. A. A., Graça, M. L. A., & Henriques, V. A. R. (2008). Isochronal sintering of the blended elemental Ti–35Nb alloy. *Materials Science and Engineering: A, 472*(1-2), 193-197.

[50] Chen, Z., Liu, Y., Jiang, H., Liu, M., Wang, C., & Cao, G. (2017). Microstructures and mechanical properties of Mn modified, Ti-Nb-based alloys. *Journal of Alloys and Compounds, 723*, 1091-1097.

[51] Santos, P. F., Niinomi, M., Liu, H., Cho, K., Nakai, M., Itoh, Y., Narushima, T., & Ikeda, M. (2016). Fabrication of low-cost beta-type Ti-Mn alloys for biomedical applications by metal injection molding process and their mechanical properties. *J Mech Behav Biomed Mater, 59*, 497-507.

[52] Sigel, H. (2000). *Metal ions in biological systems: volume 37: manganese and its role in biological processes*. CRC press.

[53] Santamaria, A. (2008). Manganese exposure, essentiality & toxicity. *Indian Journal of Medical Research, 128*(4), 484.

[54] Takeda, S., Kakiuchi, H., & Nakamura, M. (1989). Cytotoxicity of pure metals. *Shika zairyo, kikai= Journal of the Japanese Society for Dental Materials and Devices, 8*(5), 648-652.

[55] Kim, J.-W., Hwang, M.-J., Han, M.-K., Kim, Y.-G., Song, H.-J., & Park, Y.-J. (2016). Effect of manganese on the microstructure, mechanical properties and corrosion behavior of titanium alloys. *Materials Chemistry and Physics, 180*, 341-348.

[56] Alshammari, Y., Yang, F., & Bolzoni, L. (2019). Mechanical properties and microstructure of Ti-Mn alloys produced via powder metallurgy for biomedical applications. *J Mech Behav Biomed Mater, 91*, 391-397.

[57] Santos, P. F., Niinomi, M., Cho, K., Nakai, M., Liu, H., Ohtsu, N., Hirano, M., Ikeda, M., & Narushima, T. (2015). Microstructures, mechanical properties and cytotoxicity of low cost beta Ti-Mn alloys for biomedical applications. *Acta Biomater, 26*, 366-76.

[58] Franti, G., Williams, J., & Aaronson, H. (1978). A survey of eutectoid decomposition in ten Ti-X systems. *Metallurgical Transactions A, 9*(11), 1641-1649.

[59] Santos, P. F., Niinomi, M., Cho, K., Nakai, M., Liu, H., Ohtsu, N., Hirano, M., Ikeda, M., & Narushima, T. (2015). Microstructures, mechanical properties and cytotoxicity of low cost beta Ti–Mn alloys for biomedical applications. *Acta biomaterialia, 26*, 366-376.

[60] Froes, F., & Qian, M. (2018). *Titanium in Medical and Dental Applications*. Woodhead Publishing.

[61] Niinomi, M. (Compiler) (2009). *Basic Materials Science, Manufacturing and Newly Advanced Technologies of Titanium and Its Alloys*: CMC Publishing Co., Ltd.

[62] Fujii, H., & Maeda, T. (2014). Titanium alloys developed by Nippon steel & Sumitomo metal corporation. *Nippon Steel & Sumitomo Metal Technical Report, 106*, 16-21.

[63] Nakajima, H., Ohshida, S., Nonaka, K., Yoshida, Y., & Fujita, F. (1996). Diffusion of iron in {beta} Ti-Fe alloys. *Scripta materialia, 34*(6).

[64] Liu, Y., Chen, L., Tang, H., Liu, C. T., Liu, B., & Huang, B. (2006). Design of powder metallurgy titanium alloys and composites. *Materials Science and Engineering: A, 418*(1-2), 25-35.

[65] Lu, J., Zhao, Y., Niu, H., Zhang, Y., Du, Y., Zhang, W., & Huo, W. (2016). Electrochemical corrosion behavior and elasticity properties of Ti–6Al–xFe alloys for biomedical applications. *Materials Science and Engineering: C, 62*, 36-44.

[66] Chen, B.-Y., Hwang, K.-S., & Ng, K.-L. (2011). Effect of cooling process on the α phase formation and mechanical properties of sintered Ti–Fe alloys. *Materials Science and Engineering: A, 528*(13-14), 4556-4563.

[67] Umeda, J., Tanaka, T., Teramae, T., Kariya, S., Fujita, J., Nishikawa, H., Shibutani, Y., Shen, J., & Kondoh, K. (2021). Microstructures analysis and quantitative strengthening evaluation of powder metallurgy Ti–Fe binary extruded alloys with (α+β)-dual-phase. *Materials Science and Engineering: A, 803*.

[68] Alshammari, Y., Raynova, S., Yang, F., & Bolzoni, L. (2020). Effect of particle size and manufacturing technique on the properties of the PM Ti-5Fe alloy. *International Journal of Refractory Metals and Hard Materials, 90*.

[69] Esteban, P. G., Ruiz-Navas, E. M., & Gordo, E. (2010). Influence of Fe content and particle size the on the processing and mechanical properties of low-cost Ti–xFe alloys. *Materials Science and Engineering: A, 527*(21-22), 5664-5669.

[70] Ehtemam-Haghighi, S., Attar, H., Dargusch, M. S., & Kent, D. (2019). Microstructure, phase composition and mechanical properties of new, low cost Ti-Mn-Nb alloys for biomedical applications. *Journal of Alloys and Compounds, 787*, 570-577.

[71] Liu, J., Chang, L., Liu, H., Li, Y., Yang, H., & Ruan, J. (2017). Microstructure, mechanical behavior and biocompatibility of powder metallurgy Nb-Ti-Ta alloys as biomedical material. *Materials Science and Engineering: C, 71*, 512-519.

[72] Lu, X., Sun, B., Zhao, T.-f., Wang, L.-n., Liu, C.-c., & Qu, X.-h. (2014). Microstructure and mechanical properties of spark plasma sintered Ti-Mo alloys for dental applications. *International Journal of Minerals, Metallurgy, and Materials, 21*(5), 479-486.

[73] Nazari, K. A., Nouri, A., & Hilditch, T. (2015). Mechanical properties and microstructure of powder metallurgy Ti–xNb–yMo alloys for implant materials. *Materials & Design, 88*, 1164-1174.

[74] Rao, X., Chu, C., & Zheng, Y. (2014). Phase composition, microstructure, and mechanical properties of porous Ti–Nb–Zr alloys prepared by a two-step foaming powder

metallurgy method. *Journal of the mechanical behavior of biomedical materials, 34*, 27-36.

[75] Ehtemam-Haghighi, S., Liu, Y., Cao, G., & Zhang, L. C. (2016). Influence of Nb on the beta-->alpha" martensitic phase transformation and properties of the newly designed Ti-Fe-Nb alloys. *Mater Sci Eng C Mater Biol Appl, 60*, 503-510.

[76] Hsu, H.-C., Hsu, S.-K., Wu, S.-C., Lee, C.-J., & Ho, W.-F. (2010). Structure and mechanical properties of as-cast Ti–5Nb–xFe alloys. *Materials Characterization, 61*(9), 851-858.

[77] Ehtemam-Haghighi, S., Prashanth, K. G., Attar, H., Chaubey, A. K., Cao, G. H., & Zhang, L. C. (2016). Evaluation of mechanical and wear properties of Ti xNb 7Fe alloys designed for biomedical applications. *Materials & Design, 111*, 592-599.

[78] Ehtemam-Haghighi, S., Liu, Y., Cao, G., & Zhang, L.-C. (2016). Phase transition, microstructural evolution and mechanical properties of Ti-Nb-Fe alloys induced by Fe addition. *Materials & Design, 97*, 279-286.

[79] Chen, Y.-y., XU, L.-j., LIU, Z.-g., KONG, F.-t., & CHEN, Z.-y. (2006). Microstructures and properties of titanium alloys Ti-Mo for dental use. *Transactions of Nonferrous Metals Society of China, 16*, s824-s828.

[80] Cotton, J. D., Briggs, R. D., Boyer, R. R., Tamirisakandala, S., Russo, P., Shchetnikov, N., & Fanning, J. C. (2015). State of the art in beta titanium alloys for airframe applications. *Jom, 67*(6), 1281-1303.

[81] Astm, B. (Compiler) (2008). *Standard test methods for density of compacted or sintered powder metallurgy (PM) products using Archimedes' principle*: ASTM International West Conshohocken, PA.

[82] Tanaka, M., Girard, G., Davis, R., Peuto, A., & Bignell, N. (2001). Recommended table for the density of water between 0 C and 40 C based on recent experimental reports. *Metrologia, 38*(4), 301 %@ 0026-1394.

[83] Astm, B. E18-15,

[84] Karre, R., Kodli, B. K., Rajendran, A., J, N., Pattanayak, D. K., Ameyama, K., & Dey, S. R. (2019). Comparative study on Ti-Nb binary alloys fabricated through spark plasma sintering and conventional P/M routes for biomedical application. *Mater Sci Eng C Mater Biol Appl, 94*, 619-627.

[85] Ye, X., Imai, H., Shen, J., Chen, B., Han, G., Umeda, J., Takahashi, M., & Kondoh, K. (2017). Strengthening-toughening mechanism study of powder metallurgy Ti-Si alloy by interrupted in-situ tensile tests. *Journal of Alloys and Compounds, 694*, 82-92.

[86] Ye, X., Chen, B., Shen, J., Umeda, J., & Kondoh, K. (2017). Microstructure and strengthening mechanism of ultrastrong and ductile Ti-xSn alloy processed by powder metallurgy. *Journal of Alloys and Compounds, 709*, 381-393.

[87] Kolli, R., & Devaraj, A. (2018). A Review of Metastable Beta Titanium Alloys. *Metals, 8*(7).

[88] He, J., Wang, H., Huang, H., Xu, X., Chen, M., Wu, Y., Liu, X., Nieh, T., An, K., & Lu, Z. (2016). A precipitation-hardened high-entropy alloy with outstanding tensile properties. *Acta Materialia, 102*, 187-196.

[89] Plaine, A. H., da Silva, M. R., & Bolfarini, C. (2019). Tailoring the microstructure and mechanical properties of metastable Ti–29Nb–13Ta-4.6Zr alloy for self-expansible stent applications. *Journal of Alloys and Compounds, 800*, 35-40.

[90] Abdel-Hady Gepreel, M., & Niinomi, M. (2013). Biocompatibility of Ti-alloys for long-term implantation. *J Mech Behav Biomed Mater, 20*, 407-15.

[91] Long, M., & Rack, H. (1998). Titanium alloys in total joint replacement—a materials science perspective. *Biomaterials, 19*(18), 1621-1639.

[92] Davidson, J., & Georgette, F. (1987). *State of the art materials for orthopedic prosthetic devices*. Society of Manufacturing Engineers.

[93] Chaves, J. M., Florencio, O., Silva, P. S., Jr., Marques, P. W., & Afonso, C. R. (2015). Influence of phase transformations on dynamical elastic modulus and anelasticity of beta Ti-Nb-Fe alloys for biomedical applications. *J Mech Behav Biomed Mater, 46*, 184-96.

[94] Santos, P. F., Niinomi, M., Liu, H., Cho, K., Nakai, M., Trenggono, A., Champagne, S., Hermawan, H., & Narushima, T. (2016). Improvement of microstructure, mechanical and corrosion properties of biomedical Ti-Mn alloys by Mo addition. *Materials & Design, 110*, 414-424.

[95] Li, Y., Yang, C., Zhao, H., Qu, S., Li, X., & Li, Y. (2014). New Developments of Ti-Based Alloys for Biomedical Applications. *Materials (Basel), 7*(3), 1709-1800.

[96] Zhao, C., Zhang, X., & Cao, P. (2011). Mechanical and electrochemical characterization of Ti–12Mo–5Zr alloy for biomedical application. *Journal of Alloys and Compounds, 509*(32), 8235-8238.